FASJS

Faculty of Arts and Science Journal of Science

SÜLEYMAN DEMİREL
UNİVERSİTY

Süleyman Demirel University
Faculty of Arts and Sciences
Journal of Science

Volume

18

Issue

3

Year

2023

e-ISSN

1306-7575

Journal Boards

Süleyman Demirel University Faculty of Arts and Science Journal of Science is a peer-reviewed scientific journal published semi-annually, in May and November.

Original scientific research articles submitted in English in the fields of Biology, Physics, Chemistry and Mathematics are continued in the scientific review process after the preliminary evaluation stage, where similarity and layout checks are made.

No fee is charged from the author or institution under any name.

Special numbers/issues can be published without changing the periodic publication frequency during the year.

Since 2017; technical notes, letters to the editor, discussions, case reports and reviews will not be accepted.

As of 01.01.2023, Süleyman Demirel University Faculty of Arts and Sciences Journal of Science only accepts studies submitted in English.

Süleyman Demirel University Faculty of Arts and Science Journal of Science (SDUFASJS) takes into account the principles published by the Higher Education Institutions Scientific Research and Publication Ethics Directive and "Committee on Publication Ethics" (COPE). In this context, the issues that are important for the authors, referees and editors are specified in the "Ethical Principles and Publication Policy" page of the journal website.

Süleyman Demirel University Faculty of Arts and Science Journal of Science is indexed in the following databases.

- ULAKBIM TR – Dizin
- Bielefeld Academic Search Engine (BASE)
- Centre for Agriculture and Bioscience International (CABI) - CAB Direct
- China National Knowledge Infrastructure (CNKI)
- Crossref
- Directory of Open Access Journals (DOAJ)
- Directory of Open Access Scholarly Resources (ROAD)
- EBSCO host
- Elektronische Zeitschriftenbibliothek (EZB)
- German Union Catalogue of Serials (ZDB)
- Google Academic
- Index Copernicus
- Information Matrix for the Analysis of Journals (MIAR)
- MathSciNet
- ResearchBib
- WorldCat

Süleyman Demirel Üniversitesi Fen Edebiyat Fakültesi Fen Dergisi

https://dergipark.org.tr/sdufeffd

Süleyman Demirel University Faculty of Arts and Sciences Journal of Science e-ISSN: 1306-7575

Volume: 18, Issue: 3, Year: 2023

CONTENTS

Süleyman Demirel Üniversitesi Fen Edebiyat Fakültesi Fen Dergisi https://dergipark.org.tr/sdufeffd
Süleyman Demirel University Faculty of Arts and Sciences Journal of Science e-ISSN: 1306-7575
Research Article, 2023, 18(3): 195-202, DOI: 10.29233/sdufeffd.1250542

Effects of Usnic Acid on Cytotoxicity, Colony Formation and Migration in SK-UT-1 Human Uterine Leiomyosarcoma Cells

Doğukan Mutlu[1,*], Mücahit Seçme[2], Şevki Arslan[1]

[1]Department of Biology, Faculty of Science, Pamukkale University, 20160, Denizli, TURKEY
https://orcid.org/0000-0003-3259-5822
*corresponding author: dogukanmutlu@gmail.com
[2]Department of Medical Biology, Faculty of Medicine, Ordu University, 52200, Ordu, TURKEY
https://orcid.org/0000-0002-2084-760X
[1]Department of Biology, Faculty of Science, Pamukkale University, 20160, Denizli, TURKEY
https://orcid.org/0000-0002-4215-5006

(Received: 13.02.2023, Accepted: 24.07.2023, Published: 23.11.2023)

Abstract: Usnic acid (UA) is a common lichenic secondary metabolite with therapeutic potential. Anticancer, antimicrobial, and antioxidant effects have been demonstrated and UA-enriched extracts are often used to treat various diseases in traditional medicine. First, we performed a viability assay of UA in human uterine leiomyosarcoma (SK-UT-1) since no *in vitro* cytotoxicity data have been reported so far. For this purpose, the cytotoxicity of UA on SK-UT-1 and embryonic kidney (HEK293) cells was studied at 24 and 48 hours. The toxicity of UA was investigated by the MTT test. In addition, we assessed UA colony formation and migration properties against SK-UT-1 cells in 6-well plates. Our results showed a significant cytotoxic effect of UA at the 5.34 μM; UA was also effective against colony formation ability and wound healing assay. In conclusion, our study suggests that UA exerts anti-proliferative effects on SK-UT-1 cells by inducing cell death. Moreover, our results suggest that the potential anticancer activities of UA should be further studied by additional molecular biological approaches.

Keywords: Usnic acid, Uterine leiomyosarcoma, SK-UT-1, Cytotoxicity, Colony formation, Migration

1. Introduction

Uterine sarcomas are tumors with a very low incidence among all uterine cancers. They constitute ~3% of all uterine cancers [1]. Uterine leiomyosarcoma (LMS) is rare cancer that originates from the smooth muscle cells in the uterus. LMS is an aggressive tumor with a high risk of recurrence and death [1, 2]. Pharmacological agents are very important for the treatment of uterine LMSs, and a limited number of drugs such as doxorubicin, gemcitabine, eribulin and docetaxel are used in the treatment of this disease [3, 4]. Current researches focus on the development of new effective agents and novel therapeutic strategies for the treatment of this severe neoplasia [5].

Secondary metabolites are present in plants, fungi, lichens, and bacteria. They contain powerful pharmacological properties that have been used in treating various diseases including cancer, from the past to the present [6-8]. UA is a secondary metabolite, a dibenzofuran derivative, which is found very common in lichens, especially in the Usnea genus [9, 10]. UA is one of the first discovered lichen secondary metabolites and has strong pharmacological and biological activities such as antioxidant, anticancer, antimicrobial, antiviral, and anti-inflammatory [10-12]. In previous studies, the anticancer activities of UA and its derivatives have been investigated on different cancer cells such as endometrium [12], lung [13], breast [14], colorectal [15], leukemia [16], gastric [17], prostate and melanoma [18]. In all these studies, it has been reported that UA exhibits anti-carcinogenic activity through molecular biological mechanisms including stimulation of apoptosis, modulation of oxidative DNA damage, induction cell cycle arrest, suppression of cell proliferation and regulation of expression of various genes and non-coding RNAs [12-18].

In addition to all these studies, there is no study in the literature about the effectiveness of UA in LMS. The aim of this study is to evaluate the dose and time-dependent cytotoxic effect of UA in the human uterine LMS cells SK-UT-1 (HTB114), and also to reveal its effect on colony formation and migration under *in vitro* cell culture conditions.

2. Material and Method

2.1. Cell culture

The SK-UT-1 and HEK293 (embryonic kidney) cells were obtained from American Type Culture Collection (ATCC). Cells cultured with Dulbecco's Modified Eagle's Medium (DMEM) or Eagle's Minimum Essential Medium (EMEM) (Sigma-Aldrich, Germany) supplemented with 1% penicillin/streptomycin mix (Capricorn) and 10% fetal bovine serum (FBS) (Capricorn, Germany) as described previously [19].

2.2. MTT assay

Cytotoxic effects of UA on SK-UT-1 and HEK293 cells were determined by MTT (dimethyl thiazolyl tetrazolium bromide) (Merck, USA) assay as described previously [20]. SK-UT-1 and HEK293 cells were grown in 96-well plates (100 μL/well, $2x10^3$ cells) and maintained at 37°C in a humidified condition in a 5% CO_2 incubator under suitable conditions. Following 24-hour incubation, cells were treated with various concentrations (0.75, 1.5, 5, 10, and 25 μM) of UA (Sigma-Aldrich, Germany) dissolved in chloroform (CarloErba, France) (not exceeding 0.5%) 24 and 48 h. After incubation periods, 10 μL MTT solution (5 mg/mL in 100 μL culture media, Merck) was added and maintained at 37^oC. After 3 h incubation, formazan dye was dissolved in 50 μL of dimethyl sulfoxide (DMSO,Carlo Erba, Italy) for at least 30 minutes. At the end, the optical density (OD) was measured in a spectrophotometer (Epoch, BioTek, USA) at 590 nm.

2.3. Colony formation assay

Effects of UA on colony formation status in LMS cells were performed by colony formation assay described previously [21]. Briefly, cells ($1x10^3$ cells per 6-well plate) were seeded and treated with the IC50 dose of UA for 48 h. After 48 h exposure, mediums were refreshed and maintained for at least one week. The fixation of the cells was executed by 100% methanol for 10 min at -20^oC and stained with crystal violet (0.1%) at RT for 15 min. Colonies photographed under an inverted microscope (Oxion Inverso, Euromex, Holland) and counted with ImageJ software 1.53e (USA).

2.4. *In-vitro* scratch assay

The migration efficacy of the UA was investigated in SK-UT-1 cells. Briefly, $3x10^4$ cells were seeded on 6-well culture plates (Jet Biofil, China) and incubated to grow until confluent. After incubation, cells were scraped by a 200 μL tip. The wells were cleaned with phosphate-buffered saline (PBS, Bioshop, Poland) to remove detached cells. The culture medium was refreshed by media containing 5.34 μM UA for 48 h and the wound area in the treated cells was compared with the control (cells treated with chloroform at an equal volume). The wound size was imaged (0, 24, 48, and 72 h) with an inverted microscope at 10x magnification, and wound closure rate (%) was calculated with ImageJ software.

2.5. Statistical analysis

GraphPad Prism v.9 (San Diego, CA, USA) was used to evaluate the differences between two groups. The differences in the groups were evaluated using the Student’s t-test or One-way ANOVA. P <0.05 was considered as statistically significant.

3. Results and Discussion

The cytotoxicity of UA was evaluated against human uterine cancer line SK-UT-1 and the non-carcinogenic HEK293 cell line by the MTT assay. In the current study, five different concentrations of UA (0.75 to 25 µM) were attended for cytotoxicity investigations for 24 and 48 h (Figure 1). The results show a significant reduction in proliferation rate in the SK-UT-1 cells with increasing the dose concentration for 48 h. After 48 h of exposure, approximately 87% of SK-UT-1 cells were eradicated by 25µM UA treatment, decrement in the survival of 56% for HEK293 cells. The cytotoxicity of UA (expressed as IC50 values) was found to be 5.34 µM for SK-UT-1 and 21.09 µM for HEK293 cells at 48 h.

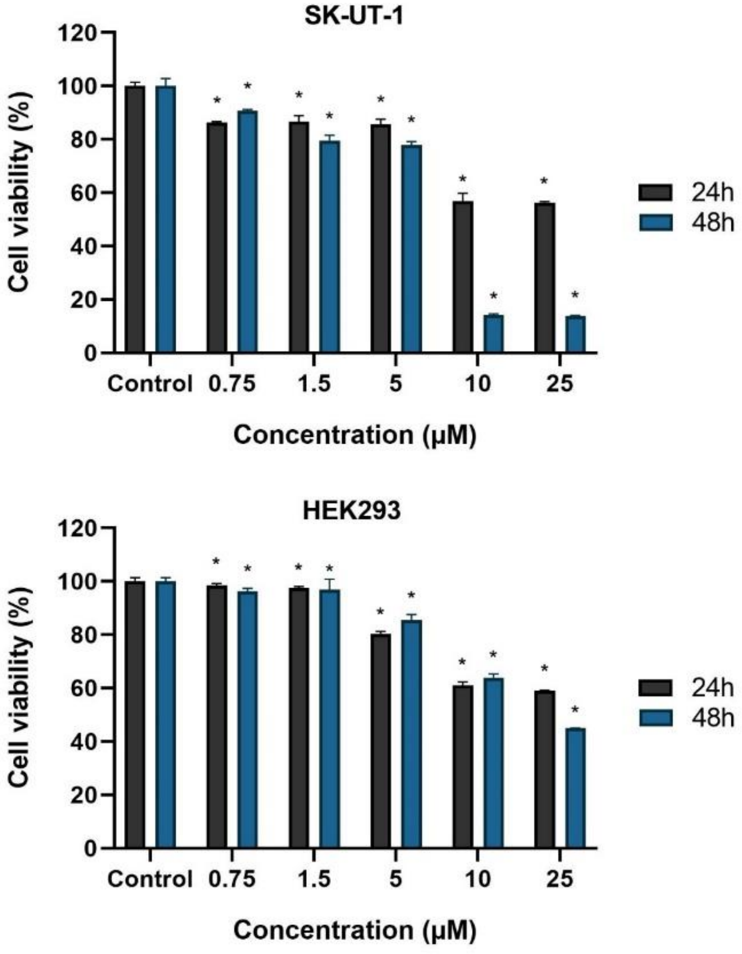

Figure 1. The cytotoxicity of UA was performed using the MTT assay of cancerous SK-UT-1 and embryonic kidney HEK293. Values are mean ± SD of triplicate value. *p <0.05 vs. control group.

The effects of UA on the proliferation of the SK-UT-1 cells were observed through colony formation assay. Figure 2 shows that the dose group treated with IC50 of UA was significantly reduced, suggesting that UA can effectively inhibit the proliferation of the uterine LMS cells.

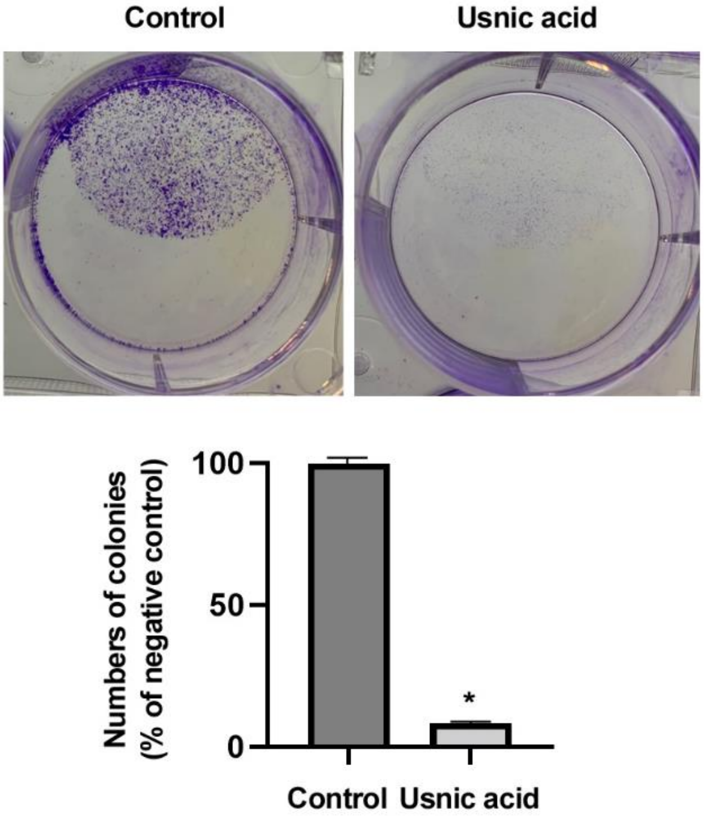

Figure 2. Colony formation assay. The number of colonies of the SK-UT-1 cells treated with UA vs. control group (containing chloroform v/v) for 48 h. *p < 0.05.

A scratch assay was carried out to assess the effect of UA on the migration of the SK-UT-1 cells. The migration of SK-UT-1 cells was significantly inhibited by UA and cell migration was restricted by 63% at the end of 72 h compared to control (Figure 3, p <0.05).

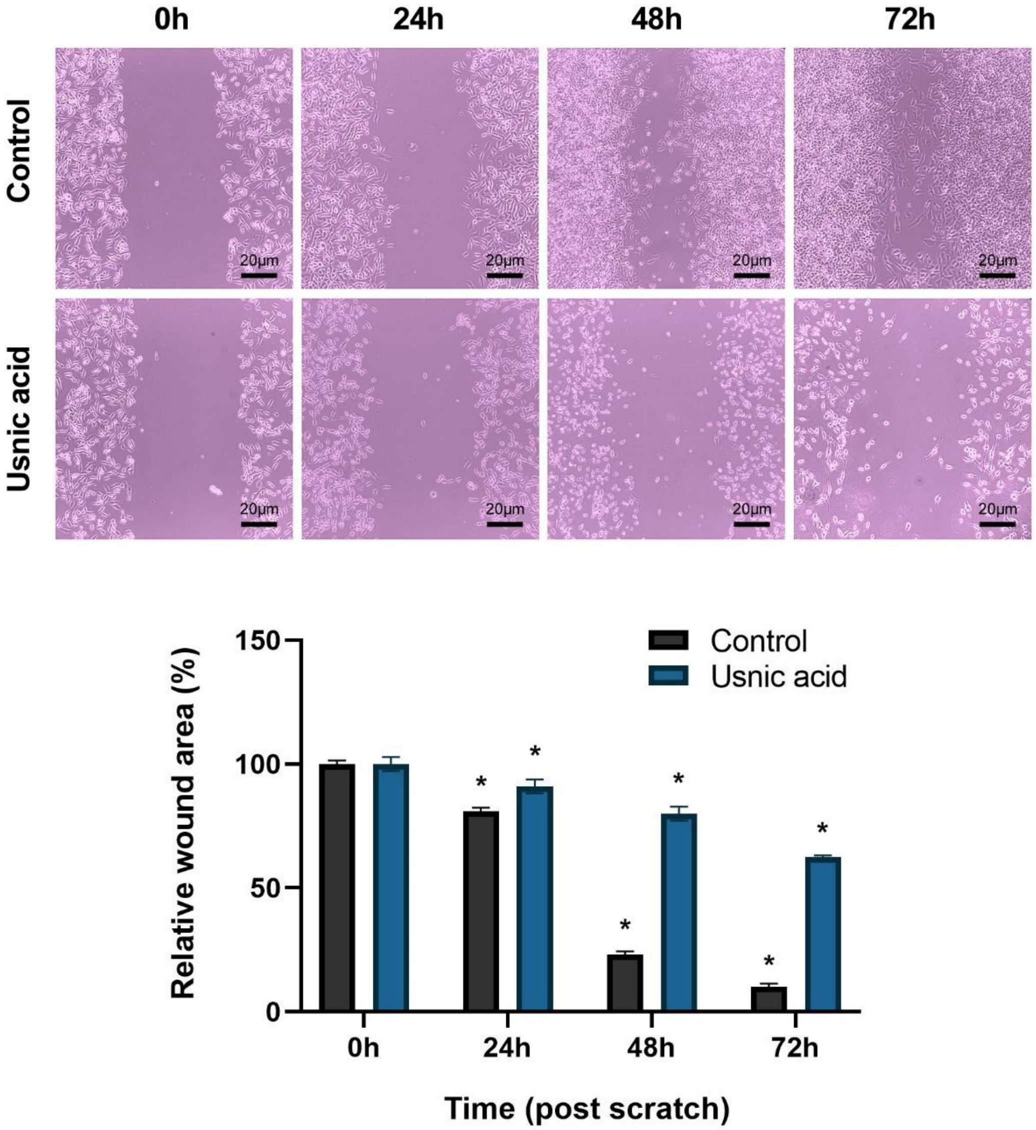

Figure 3. *In vitro* scratch assay. The photos were taken 0, 24, 48, and 72 h. Relative wound area in SK-UT-1 cells treated with UA vs. control group. *p <0.05.

In a study, it was reported that UA may have triggered the reactive oxygen species-dependent mitochondrial pathway-mediated apoptotic mechanism [22]. In a recent study, UA significantly reduced cell proliferation in AGS gastric cancer cells in the dose range of 10-50 µM and induced apoptosis in gastric cancer cells [17]. Galanty et al. (2017) demonstrated that UA exhibits anti-proliferative effects on DU145 and PC3 prostate cancer under *in vitro* conditions [18]. Wu et al. [23] have showed that UA inhibits cell proliferation in colorectal cancer cells through ATM-mediated DNA damage signaling pathway. Furthermore, they have demonstrated that UA inhibited colorectal cancer cell migration in the cell culture wound healing assay model.

In another study, it was shown that UA causes inhibition of cell motility in non-small cell lung cancer cells [24]. In a study, when the cytotoxic effects of UA on the HepG2 cell line, NS20Y, and HUVEC cells were analyzed, it was reported that the IC50 value of UA was higher in HUVEC cells used as control cells compared to cancer cells [25]. Emsen et al. [26] have showed that the UA decreased cell viability in U87MG glioblastoma cells and primary rat cerebral cortex (PRCC) cells. While the IC50 value in glioblastoma cells was determined as 41.55 mg/L, the IC50 value in PRCC cells was determined as 132.69 mg/L, which is a higher dose than glioblastoma. Similar to our study, it was reported that

UA showed more cytotoxic activity in cancer cells in comparison with non-cancerous cell lines [18, 27-29].

It was demonstrated by *in vitro* clonogenic test that UA inhibits colony formation in A549 cells. It was showed that UA treatment not only reduces the colony amount of A549 lung cancer but also reduces the colony sizes, especially depending on the increasing dose [30]. In a study on the anticancer activity of UA in COLO-205 colon cancer cells, it was shown that UA inhibited colony formation even at low doses, as well as inhibited cell proliferation [31]. Our results showed that the UA has a cytotoxic effect on the SK-UT-1 cells. The UA was cytotoxic after 48 h at concentrations above 5 μM, decreasing the viability of SK-UT-1 cells to about 13% at the highest concentration (25 μM). Besides, UA significantly revealed less toxicity on non-cancerous (HEK293) cells in comparison with the SK-UT-1 cells, HEK293 viability at 25 μM did not decrease below 40%. In the colony formation assay, we found that UA significantly inhibited the colony formation capability for SK-UT-1 cells. Similar effects were also observed in a wound-healing assay.

4. Conclusion

Our results suggest that UA can be an alternative bioactive agent for human uterine LMS SK-UT-1 (also known as HTB-114) cells. Our study is the first examination of the antiproliferative effects of the UA on SK-UT-1 cells. The molecular mechanism underlying the potential anti-cancer activities of UA should be investigated in further studies.

Authorship contribution statement

D. Mutlu: Methodology, Visualization, Original Draft Writing; **M. Seçme**: Methodology, Advice; **Ş. Arslan**: Supervision.

Declaration of competing interest

The authors declare that they have no known competing financial interests or personal relationships that could have appeared to influence the work reported in this paper.

Ethics Committee Approval and/or Informed Consent Information

As the authors of this study, we declare that we do not have any ethics committee approval and/or informed consent statement.

References

[1] E. D'Angelo, J. Prat, “Uterine sarcomas: a review”, *Gynecologic oncology*, 116(1), 131-139, 2010.

[2] R. L. Giuntoli, D. S. Metzinger, C. S. DiMarco, S. S. Cha, J. A. Sloan, G. L. Keeney and B. S. Gostout, “Retrospective review of 208 patients with leiomyosarcoma of the uterus: prognostic indicators, surgical management, and adjuvant therapy”, *Gynecologic oncology*, 89(3), 460-469, 2003.

[3] E. Fujimoto, K. Takehara, T. Tanaka, T. Yokoyama, K. Tomono, M.Okazawa-Sakai, S. Okame, Y. Sugawara and N. Teramoto, “Uterine leiomyosarcoma well-controlled with eribulin mesylate”, *International cancer conference journal*, (8)1, 33-38, 2018.

[4] M. Azumi, M. Yoshie, N. Nakachi, A. Tsuru, K. Kusama and K. Tamura, “Stathmin expression alters the antiproliferative effect of eribulin in leiomyosarcoma cells”, *Journal of pharmacological sciences*, 150(4), 259-266, 2022.

[5] A. Pistilli, M. Rende, L. Crispoltoni, C. Montagnoli and A. M. Stabile, “LY294002 induces in vitro apoptosis and overexpression of p75NTR in human uterine leiomyosarcoma HTB 114 cells”, *Growth factors (Chur, Switzerland)*, 33(5-6), 376-383, 2015.

[6] O. Mosunova, J. C. Navarro-Muñoz and J. Collemare, “The biosynthesis of fungal secondary metabolites: From fundamentals to biotechnological applications”, *In Encyclopedia of Mycology*, 2, 458-476, 2021.

[7] A. M. L. Seca and D. C. G. A. Pinto, “Plant secondary metabolites as anticancer agents: Successes in clinical trials and therapeutic application”, *International Journal of Molecular Sciences*, 19(1), 263, 2018.

[8] S. Bhattacharyya, P. R. Deep, S. Singh and B. Nayak, “Lichen Secondary Metabolites and Its Biological Activity”, *American Journal of Pharmtech Research*, 6(6), 29-44, 2016.

[9] F. Salgado, L. Albornoz, C. Cortéz, E. Stashenko, K. Urrea-Vallejo, E. Nagles, C. Galicia-Virviescas, A. Cornejo, A. Ardiles, M. Simirgiotis, O. García-Beltrán, and C. Areche, “Secondary Metabolite Profiling of Species of the Genus Usnea by UHPLC-ESI-OT-MS-MS”, *Molecules (Basel, Switzerland)*, 23(1), 54, 2017.

[10] H. Wang, M. Xuan, C. Huang and C. Wang, “Advances in Research on Bioactivity, Toxicity, Metabolism, and Pharmacokinetics of UA In Vitro and In Vivo”, *Molecules (Basel, Switzerland)*, 27(21), 7469, 2022.

[11] A. A. Araújo, M. G. de Melo, T. K. Rabelo, P. S. Nunes, S. L. Santos, M. R. Serafini, M. R. J Santos, L. J. Quintans-Júnior and D. P. Gelain, “Review of the biological properties and toxicity of UA”, *Natural product research*, 29(23), 2167-2180, 2015.

[12] M. Secme and Y. Dodurga, “UA Inhibits Cell Proliferation and Downregulates lncRNA UCA1 Expression in Ishikawa Endometrial Cancer Cells”, *Natural Products and Biotechnology*, 1(1), 28-37, 2021.

[13] W. Qi, C. Lu, H. Huang, W. Zhang, S. Song and B. Liu, “(+)-UA Induces ROS-dependent Apoptosis via Inhibition of Mitochondria Respiratory Chain Complexes and Nrf2 Expression in Lung Squamous Cell Carcinoma”, *International journal of molecular sciences*, 21(3), 876, 2020.

[14] N. Kilic, Y. O. Islakoglu, I. Buyuk, B. Gur-Dedeoglu and D. Cansaran-Duman, “Determination of UA Responsive miRNAs in Breast Cancer Cell Lines”, *Anti-cancer agents in medicinal chemistry*, 19(12), 1463-1472, 2019.

[15] L. Samuelsen, P. E. Hansen and O. Vang, “Derivatives of UA cause cytostatic effect in Caco-2 cells”, *Natural product research*, 35(23), 4953-4959, 2021.

[16] S. Wang, J. Zang, M. Huang, L. Guan, K. Xing, J. Zhang, D. Liu and L. Zhao, “Discovery of novel (+)-UA derivatives as potential anti-leukemia agents with pan-Pim kinases inhibitory activity”, *Bioorganic chemistry*, 89, 102971, 2019.

[17] K. Kumar, J. P. N. Mishra and R. P. Singh, “UA induces apoptosis in human gastric cancer cells through ROS generation and DNA damage and causes up-regulation of DNA-PKcs and γ-H2A.X phosphorylation”, *Chemico-biological interactions*, 315, 108898, 2020.

[18] A. Galanty, P. Koczurkiewicz, D. Wnuk, M. Paw, E. Karnas, I. Podolak, M. Węgrzyn, M. Borusiewicz, Z. Madeja, J. Czyż and M. Michalik, “UA and atranorin exert selective cytostatic and anti-invasive effects on human prostate and melanoma cancer cells”, *Toxicology in vitro*, 40, 161-169, 2017.

[19] C. Yilmaz, S. Arslan, D. Mutlu, M. Konus, A. Kayhan, A. Kurt-Kizildogan, C. Otur, O. Ozok, and A. Kivrak, “Identification of 3-Bromo-1-Ethyl-1H-Indole as a Potent Anticancer Agent with Promising Inhibitory Effects on GST Isozymes”, *Anti-Cancer Agents in Medicinal Chemistry*, 21(10), 1292-1300, 2021.

[20] E. Kavak, D. Mutlu, O. Ozok, S. Arslan and A. Kivrak, “Design, synthesis and pharmacological evaluation of novel Artemisinin-Thymol”, *Natural Product Research*, 36(14), 3511-3519, 2022.

[21] D. Mutlu, C. Cakir, M. Ozturk and S. Arslan, “Anticancer and apoptotic effects of a polysaccharide extract isolated from Lactarius chrysorrheus Fr. in HepG2 and PANC-1 cell lines”, *Archives of Biological Sciences*, 74(4), 315-324, 2022.

[22] S. T. Zuo, L. P. Wang, Y. Zhang, D. N. Zhao, Q. S. Li, D. Shao and X. D. Fang, “Usnic acid induces apoptosis via an ROS-dependent mitochondrial pathway in human breast cancer cells in vitro and in vivo”, *RSC Advances*, 5(1), 153-162, 2015.

[23] W. Wu, H. Gou, J. Dong, X. Yang, Y. Zhao, H. Peng, D. Chen, R. Geng, L. Chen and J. Liu, “Usnic Acid Inhibits Proliferation and Migration through ATM Mediated DNA Damage Response in RKO Colorectal Cancer Cell”, *Current pharmaceutical biotechnology*, 22(8), 1129-1138, 2021.

[24] Y. Yang, T. T. Nguyen, M. Jeong, F. Crisan, Y. H. Yu, H. Ha, K. H. Choi, H. G. Jeong, T. C. Jeong, K. Y. Lee, K. K. Kim, J. S. Hur and H. Kim, “Inhibitory Activity of (+)-Usnic Acid against Non-Small Cell Lung Cancer Cell Motility”, *PloS one*, 11(1), 2016.

[25] A. T. Koparal, “Anti-angiogenic and antiproliferative properties of the lichen substances (-)-usnic acid and vulpinic acid. Zeitschrift fur Naturforschung” *Journal of biosciences*, 70(5-6), 159–164, 2015.

[26] B. Emsen, A. Aslan, H. Turkez, A. Joughi and A. Kaya, “The anti-cancer efficacies of diffractaic, lobaric, and usnic acid: In vitro inhibition of glioma”, *Journal of cancer research and therapeutics*, 14(5), 941–951, 2018.

[27] N. S. Dyrkheeva, A. S. Filimonov, O. A. Luzina, A. L. Zakharenko, E. S. Ilina, A. A. Malakhova, S. P. Medvedev, J. Reynisson, K. P. Volcho, S. M. Zakian, N. F. Salakhutdinov and O. I. Lavrik, “New Hybrid Compounds Combining Fragments of Usnic Acid and Monoterpenoids for Effective Tyrosyl-DNA Phosphodiesterase 1 Inhibition”, *Biomolecules*,11(7), 973, 2021.

[28] B. Yurdacan, U. Egeli, G. G. Eskiler, I. E. Eryilmaz, G. Cecener and B. Tunca, "The role of usnic acid-induced apoptosis and autophagy in hepatocellular carcinoma", *Human & Experimental Toxicology*, 38(2), 201-215, 2019.

[29] B. Colak, D. Cansaran-Duman, G. G. Eskiler, K. Földes and S. Yangin, "Usnic acid-induced programmed cell death in ovarian cancer cells", *Rendiconti Lincei. Scienze Fisiche e Naturali*, 33, 143-152, 2022.

[30] N. Singh, D. Nambiar, R. K. Kale and R. P. Singh, “Usnic acid inhibits growth and induces cell cycle arrest and apoptosis in human lung carcinoma A549 cells”, *Nutrition and cancer*, 65, 36–43, 2013.

[31] T. Anuk, B. Yildiz, R. Demirel, M. Icen, S. Yildirim, H. Beseren, B. Mor and O. Ozden, “Usnic acid reduces colon cancer cell viability and colony formation by affecting cancer cell metabolism”, *Kafkas Universitesi Veteriner Fakultesi Dergisi*, 28(4), 491-497, 2022.

Süleyman Demirel Üniversitesi Fen Edebiyat Fakültesi Fen Dergisi https://dergipark.org.tr/sdufeffd
Süleyman Demirel University Faculty of Arts and Sciences Journal of Science e-ISSN: 1306-7575
Research Article, 2023, 18(3): 203-212, DOI: 10.29233/sdufeffd.1262031

On Neutrosophic Square Matrices and Solutions of Systems of Linear Equations

Yılmaz Çeven[1,*], Ali İhsan Sekmen[2]

[1]Department of Mathematics, Faculty of Arts and Sciences, Süleyman Demirel University, 32260, Isparta, TURKEY
https://orcid.org/0000-0002-2968-1546
*corresponding author: *yilmazceven@sdu.edu.tr*
[2] Graduate School of Natural and Applied Sciences, Süleyman Demirel University, 32260, Isparta, TURKEY
https://orcid.org/0000-0002-5342-0418

(Received: 08.03.2023, Accepted: 31.08.2023, Published: 23.11.2023)

Abstract: We started this work with a theorem that shows in which case the abbreviation rule for neutrosophic real numbers is true. We then detail in which cases the division of two neutrosophic real numbers yields a new neutrosophic number. Then, the solution cases of a neutrosophic linear equation with one unknown were examined. After calculating the determinant of a square matrix and giving the necessary and sufficient conditions for a square matrix to be invertible, the solution conditions of the systems of equations with the number of unknowns equal to the number of equations were examined.

Key words: Neutrosophic matrices, Neutrosophic systems of linear equations, Determinant of a neutrosophic square matrix, Inverse of neutrosophic square matrix

1. Introduction

Smarandache firstly studied the concept of neutrosophy to address the uncertainty in nature and science. [1]. Neutrosophy has important applications in a lot of fields and researchers done many studies on the subject. Neutrophic number theory and neutrophic linear algebra are just two of these fields. Some of the studies carried out in these areas are given in the references [2-10].

We firstly started this work with a theorem that shows in which case the abbreviation rule for neutrosophic real numbers is true. We then detail in which cases the division of two neutrosophic real numbers yields a new neutrosophic number. Then, the solution cases of a neutrosophic linear equation with one unknown were examined. After calculating the determinant of a square matrix and giving the necessary and sufficient conditions for a square matrix to be invertible, the solution conditions of the systems of equations with the number of unknowns equal to the number of equations were examined. Also, we gave some important examples to clarify the theory.

2. Material and Method

In this section, some definitions and theorems of neutrosophic numbers and matrices will be given, which we will use in later chapters. As known, the set of neutrosophic real numbers $is\ R[I] = \{\alpha + \beta I | \alpha, \beta \in R, I^2 = I\}$ and the I used here is called the unknown.

The following definition is given for neutrosophic rational numbers in [3]. But it would not be wrong to define it for real numbers as well.

Definition 2.1 [3] Let $\alpha+\beta I \in R[I]$. The norm and the conjugate of $\alpha+\beta I$ are defined by $N(\alpha+\beta I)=\alpha(\alpha+\beta)$ and $\overline{\alpha+\beta I}=\alpha+\beta-\beta I$.

It is seen that $(\alpha+\beta I)\left(\overline{\alpha+\beta I}\right)=N(\alpha+\beta I)$. Also, it is seen that $N(\alpha+\beta I)=0$ if and only if $\alpha=0$ or $\alpha+\beta=0$.

Also, it is true that $N(x.y)=N(x).N(y)$ for $x,y \in R[I]$ by Proposition 3.5 (vi) in [3].

Definition 2.2 [8] Let $A=N+MI$ be a $n\times n$ neutrosophic matrix where N and M are $n\times n$ real matrices. The determinant of A is defined as

$$detA=detN+(\det(N+M)-detN)I.$$

Theorem 2.3 [8] Let $A=N+MI$ be a $n\times n$ neutrosophic matrix where N and M are $n\times n$ real matrices. Then a necessary and sufficient condition for the inverse of A to exist N and $N+M$ invertible matrices and

$$A^{-1}=N^{-1}+((N+M)^{-1}-N^{-1})I.$$

3. Results

Theorem 3.1 Let $\alpha,\beta,\gamma \in R[I]$. If $\alpha\beta=\alpha\gamma$ and $N(\alpha)\neq 0$, then $\beta=\gamma$.

Proof. Let $\alpha\beta=\alpha\gamma$ and $N(\alpha)\neq 0$ where $\alpha=\alpha_1+\alpha_2 I, \beta=\beta_1+\beta_2 I$ and $\gamma=\gamma_1+\gamma_2 I$. Since $N(\alpha)=\alpha(\alpha+\beta)\neq 0$, we have $\alpha\neq 0$ and $\alpha+\beta\neq 0$. Since $\alpha\beta=\alpha\gamma$, we have $(\alpha_1+\alpha_2 I)(\beta_1+\beta_2 I)=(\alpha_1+\alpha_2 I)(\gamma_1+\gamma_2 I)\Rightarrow \alpha_1\beta_1+\big((\alpha_1+\alpha_2)(\beta_1+\beta_2)-\alpha_1\beta_1\big)I=\alpha_1\gamma_1+((\alpha_1+\alpha_2)(\gamma_1+\gamma_2)-\alpha_1\gamma_1)I$. Hence, we get $\alpha_1\beta_1=\alpha_1\gamma_1$ and since $\alpha_1\neq 0$, we have $\beta_1=\gamma_1$. Also, since $(\alpha_1+\alpha_2)(\beta_1+\beta_2)=(\alpha_1+\alpha_2)(\gamma_1+\gamma_2)$, $\alpha+\beta\neq 0$ and $\beta_1=\gamma_1$, we have $\beta_2=\gamma_2$. Consequently, it is seen that $\beta=\gamma$.

Definition 3.2 Let $0\neq a+bI,\, c+dI \in R[I]$. If there exists a neutrosophic real number $k+tI\in R[I]$ such that $c+dI=(k+tI)(a+bI)$, then we say $a+bI$ divides $c+dI$ and denote $a+bI|c+dI$. In this case $\frac{c+dI}{a+bI}=k+tI\in R[I]$.

Note that the set $R[I]$ is not closed according to the division. The quotient of two neutrosophic numbers may not be a neutrosophic number.

Example 3.3 Since $10+5I=(2+3I)(5-2I)$, we have $2+3I|10+5I$. But there do not exist any neutrosophic real number $k+tI$ such that $2+4I=(k+tI)(1-I)$, we have $1-I\nmid 2+4I$.

Teorem 3.4 Let $0\neq \alpha+\beta I,\ \gamma+\delta I\in R[I]$ and $x=\frac{\gamma+\delta I}{\alpha+\beta I}$. Then

i) if $N(\alpha+\beta I)\neq 0$, then $x=\frac{\gamma}{\alpha}+\frac{\alpha\delta-\beta\gamma}{\alpha(\alpha+\beta)}I\in R[I]$,

ii) in case $N(\alpha+\beta I)=0$,

a) if $\alpha = 0,\ \gamma \neq 0$, then $x = \dfrac{\gamma+\delta I}{\alpha+\beta I} = \dfrac{\gamma+\delta I}{\beta I} \notin R[I]$,

b) if $\alpha = 0,\ \gamma = 0$, then $x = \dfrac{\gamma+\delta I}{\alpha+\beta I} = \dfrac{\delta I}{\beta I} = m + nI \in R[I]$ where $m + n = \dfrac{\delta}{\beta}$,

c) if $\beta = -\alpha \neq 0, \gamma + \delta \neq 0$, then $x = \dfrac{\gamma+\delta I}{\alpha+\beta I} = \dfrac{\gamma+\delta I}{\alpha-\alpha I} \notin R[I]$,

d) if $\beta = -\alpha \neq 0, \gamma = -\delta \neq 0$, then $x = \dfrac{\gamma+\delta I}{\alpha+\beta I} = \dfrac{\gamma-\gamma I}{\alpha-\alpha I} = \dfrac{\gamma}{\alpha} + nI \in R[I]$ where $n \in R$.

Proof. $i)$ Let $N(\alpha+\beta I) = \alpha(\alpha+\beta) \neq 0$. Then $\alpha \neq 0$ and $\alpha+\beta \neq 0$. Hence, we get

$$\begin{aligned} x &= \frac{\gamma+\delta I}{\alpha+\beta I} \\ &= \frac{(\gamma+\delta I)(\alpha+\beta-\beta I)}{(\alpha+\beta I)(\alpha+\beta-\beta I)} \\ &= \frac{\gamma(\alpha+\beta)+(\alpha\delta-\beta\gamma)}{N(\alpha+\beta I)} \\ &= \frac{\gamma}{\alpha} + \frac{\alpha\delta-\beta\gamma}{\alpha(\alpha+\beta)} I \in R[I]. \end{aligned}$$

$ii)$ Let $N(\alpha+\beta I) = \alpha(\alpha+\beta) = 0$. Then $\alpha = 0$ or $\alpha+\beta = 0$. (since $\alpha+\beta I \neq 0, \alpha$ and β can not both be zero) Firstly, let $\alpha = 0$ and $\alpha+\beta \neq 0$. Then if $x = \dfrac{\gamma+\delta I}{\alpha+\beta I} = m + nI$ for any $m,\ n \in R$, we have $m\alpha = \gamma$ and $(m+n)(\alpha+\beta) = \gamma+\delta$. **(a)** Since $\alpha = 0$, if $\gamma \neq 0$, there do not exist any $m \in R$ such that $m\alpha = \gamma$. That is, $x = \dfrac{\gamma+\delta I}{\beta I} \notin R[I]$ for $\gamma \neq 0$. **(b)** If $\alpha = 0, \gamma = 0$, the equality $m\alpha = \gamma$ is true for all $m \in R$. From the equality $(m+n)(\alpha+\beta) = \gamma+\delta$, we have $m+n = \dfrac{\delta}{\beta}$. So $x = \dfrac{\gamma+\delta I}{\alpha+\beta I} = \dfrac{\delta I}{\beta I} = m + nI \in R[I]$ where $m + n = \dfrac{\delta}{\beta}$. **(c)** Let $\alpha \neq 0$ and $\alpha+\beta = 0$. Then we have $\beta = -\alpha$. From the equality $m\alpha = \gamma$, we have $m = \dfrac{\gamma}{\alpha}$ and from the equality $(m+n)(\alpha+\beta) = \gamma+\delta$, we have $\left(\dfrac{\gamma}{\alpha} + n\right).0 = \gamma+\delta$. Then if $\gamma+\delta \neq 0$, there are not any $n \in R$ such that $\left(\dfrac{\gamma}{\alpha} + n\right).0 = \gamma+\delta$. Hence $x = \dfrac{\gamma+\delta I}{\alpha+\beta I} = \dfrac{\gamma+\delta I}{\alpha-\alpha I} \notin R[I]$ where $\gamma+\delta \neq 0$. **(d)** If $\gamma+\delta = 0$, it is true the equality $\left(\dfrac{\gamma}{\alpha} + n\right).0 = \gamma+\delta$ for all $n \in R$. In this case $x = \dfrac{\gamma+\delta I}{\alpha+\beta I} = \dfrac{\gamma-\gamma I}{\alpha-\alpha I} = \dfrac{\gamma}{\alpha} + nI \in R[I]$ for all $n \in R$.

Example 3.5 $\frac{2+\mathrm{I}}{1+\mathrm{I}}=2-\frac{1}{2}I\in R$, $\frac{2+\mathrm{I}}{\mathrm{I}}\notin R[I]$, $\frac{4\mathrm{I}}{2\mathrm{I}}=m+nI\in R[I]$ where $m+n=2$, $\frac{2+\mathrm{I}}{1-\mathrm{I}}\notin R[I]$, $\frac{2-2\mathrm{I}}{1-\mathrm{I}}=2+nI\in R[I]$ where $n\in R$.

Theorem 3.6 Let $\alpha x=\beta$ be a neutrosophic liner equation where $0\neq\alpha,\beta\in R[I]$.
i) If $N(\alpha)\neq 0$, then $\alpha x=\beta$ has unique solution in $R[I]$ and the solution is $x=\frac{\bar{\alpha}.\beta}{N(\alpha)}$
ii) If $N(\alpha)=0$ and $\alpha|\beta$, then $\alpha x=\beta$ has an infinite number of solutions.
iii) If $N(\alpha)=0$ and $\alpha\nmid\beta$, then $\alpha x=\beta$ has no solutions in $R[I]$.

Proof. It is clear by Theorem 3.4.

Example 3.7 i) Consider the neutrosophic linear equation $(2+3I)x=4-I$. Since $N(2+3I)=10\neq 0$ and $\overline{2+3I}=5-3I$, we have $\mathrm{x}=\frac{\overline{(2+3\mathrm{I})}(4-\mathrm{I})}{\mathrm{N}(2+3\mathrm{I})}=2-\frac{7}{5}\mathrm{I}$.
ii) For $(1-I)x=3-3I$, since $1-I\neq 0, N(1-I)=0$ and $1-I|3-3I$, the equation has an infinite number of solutions: Let $x=a+bI$. Then since $(1-I)(a+bI)=3-3I$, we have $a-aI=3-3I$. Hence, we see that $a=3, b\in R$. Then the solution set is $\{3+bI: b\in R\}$.
iii) Consider the neutrosophic linear equation $(1-I)x=2+I$. We have $1-I\neq 0, N(1-I)=0$ and $1-I\nmid 2+I$. Since there are no neutrosophic number $a+bI$ such that $(1-I)(a+bI)=2+I$, the equation has no solutions.
iv) The solution set of the equation $2Ix=4I$ is $\{m+nI: m+n=2, m,n\in R\}$.

Consider the equation $ax+by=c$ ($a\neq 0$ or $b\neq 0$) in R. It is known that

i) if $b\neq 0$, then the solution set is $\left\{\left(x,\frac{c-ax}{b}\right): x\in R\right\}$,

ii) if $a\neq 0$, then the solution set is $\left\{\left(\frac{c-by}{a},y\right): y\in R\right\}$.

Now we investigate the solutions of a neutrosophic liner equation with two variables.

Theorem 3.8 Let $\alpha x+\beta y=\gamma$ be a neutrosophic liner equation with two variables where $\alpha,\beta,\gamma\in R[I]$ and $\alpha\neq 0, \beta\neq 0$.
i) If $N(\alpha)\neq 0$, then the solution set is $\left\{\left(\frac{(\gamma-\beta y)\bar{\alpha}}{N(\alpha)},y\right)\middle| y\in R[I]\right\}$,
ii) If $N(\beta)\neq 0$, then the solution set is $\left\{\left(x,\frac{(\gamma-\alpha x)\bar{\beta}}{N(\beta)}\right)\middle| x\in R[I]\right\}$,
iii) If $N(\alpha)=0\ and\ N(\beta)=0$, then
a) there exist infinitely many $y\in R[I]$ for all x that satisfies the property $\beta|\gamma-\alpha x$,
b) there do not exist any $y\in R[I]$ for an x that satisfies the property $\beta\nmid\gamma-\alpha x$,
or
c) there exist infinitely many $x\in R[I]$ for all y that satisfies the property $\alpha|\gamma-\beta y$,
d) there do not exist any $x\in R[I]$ for an y that satisfies the property $\alpha\nmid\gamma-\beta y$

Proof. i) If $N(\alpha)\neq 0$, then we have $x=\frac{\gamma-\beta y}{\alpha}=\frac{(\gamma-\beta y)\bar{\alpha}}{\alpha\bar{\alpha}}=\frac{(\gamma-\beta y)\bar{\alpha}}{N(\alpha)}\in R[I]$.
Then the solution set is $\left\{\left(\frac{(\gamma-\beta y)\bar{\alpha}}{N(\alpha)},y\right)\middle| y\in R[I]\right\} y\in R[I]$.
ii) $N(\beta)\neq 0$, the proof is similar (i).

iii) Let $N(\alpha) = 0$ and $N(\beta) = 0$. From the equation $\alpha x + \beta y = \gamma$, we have $y = \frac{\gamma - \alpha x}{\beta}$. In this case, by Theorem 3.6, if $\beta | \gamma - \alpha x$ for any $x \in R[I]$, then there exist infinitely many $y = \frac{\gamma - \alpha x}{\beta} \in R[I]$. But if $\beta \nmid \gamma - \alpha x$ for any $x \in R[I]$, then there do not exist an $y = \frac{\gamma - \alpha x}{\beta}$ in R[I]. Hence (a) and (b) are true. Similarly (c) and (d) are true.

In [9], according to Alhasan's analysis in part 3.1, every neutrosophic linear equation with two variables is solvable. But as seen from the Theorem 3.8, some equations may be unsolvable.

Example 3.9 i) Consider the equation $(1+I)x + (2-I)y = 1 + 2I$. Since $N(2-I) = 2 \neq 0$ and $\overline{2-I} = 1 + I$, we see that, the solution is

$$y = \frac{1+2I}{2-I} - \frac{1+I}{2-I}x$$

$$= \frac{1}{2} - \frac{5}{2}\mathrm{I} - \left(\frac{1}{2} + \frac{3}{2}\mathrm{I}\right)x$$

for all $x \in R[I]$.

ii) Consider the equation $2Ix + 3Iy = 4I$. We see that $N(2I) = 0$ and $N(3I) = 0$. In this case, since $y = \frac{4I - 2Ix}{3I}$ and $3I | 4I - 2Ix$ for all $x \in R[I]$, there exist infinitely many solutions. For example, for $x = 0$, $y = a + bI$ $(a + b = \frac{4}{3})$ are the solutions since $\frac{4\mathrm{I}}{3\mathrm{I}} = \left\{ a + bI \in R[I] \middle| a + b = \frac{4}{3} \right\}$.

iii) Consider the equation $2Ix + 3Iy = 1 + 4I$. We see that $N(2I) = 0$ and $N(3I) = 0$. In this case, since $y = \frac{1 + 4I - 2Ix}{3I}$ and $3I \nmid 1 + 4I - 2Ix$ for all $x \in R[I]$, So this equation has no solution.

In [8, Definition 3.2], the determinant of the matrix $M = A + BI$ is given as a definition in terms of A and B. In the following theorem, we give this property as a theorem.

Theorem 3.10 Let $\mathcal{A}$ and $\mathcal{B}$ be $n \times n$ real matrix and $\mathcal{M} = \mathcal{A} + \mathcal{B}I$. Then the determinant of $\mathcal{M}$ is

$$det\mathcal{M} = det\mathcal{A} + (\det(\mathcal{A} + \mathcal{B}) - det\mathcal{A})I.$$

Proof. Let $\mathcal{M} = \mathcal{A} + \mathcal{B}I = [m_{ij}]_{2\times 2}$, $\mathcal{A} = [a_{ij}]_{2\times 2}$ and $\mathcal{B} = [b_{ij}]_{2\times 2}$. Then $\det(\mathcal{M}) = m_{11}m_{22} - m_{12}m_{21}$

$$= (a_{11} + b_{11}I)(a_{22} + b_{22}I) - (a_{12} + b_{12}I)(a_{21} + b_{21}I)$$

$$= a_{11}a_{22} - a_{12}a_{21} + (a_{11}b_{22} + b_{11}a_{22} + b_{11}b_{22} - a_{12}b_{21} - b_{12}a_{21} - b_{12}b_{21})I$$

$$= a_{11}a_{22} - a_{12}a_{21} + (a_{11}b_{22} + b_{11}a_{22} + b_{11}b_{22} + a_{11}a_{22} - a_{12}a_{21} - a_{11}a_{22} - a_{12}a_{21} - a_{12}b_{21} - b_{12}a_{21} - b_{12}b_{21})I$$

$$\begin{aligned} &= a_{11}a_{22} - a_{12}a_{21} \\ &\qquad - \big((a_{11}+b_{11})(a_{22}+b_{22}) - (a_{21}+b_{21})(a_{12}+b_{12}) - (a_{11}a_{22} \\ &\qquad - a_{12}a_{21})\big)I \end{aligned}$$

$$= det\mathcal{A} + (\det(\mathcal{A}+\mathcal{B}) - det\mathcal{A})I.$$

Hence the claim is true for case n=2. Now suppose that the assertion is true for case n-1. Then, by the cofactor expansion about the first row, we have

$$\det(\mathcal{M}) = m_{11}M_{11} + m_{12}M_{12} + \cdots + m_{1n}M_{1n}$$

where M_{1j} is the cofactor of $m_{1j} = a_{1j} + b_{1j}I$ for $1 \le j \le n$. Let M'_{1j}, A'_{1j} and B'_{1j} be the $(n-1)\times(n-1)$ submatrices of $\mathcal{M}, \mathcal{A}$ and $\mathcal{B}$ obtained by deleting the first row and jth column respectively. Then since $M'_{1j} = A'_{1j} + B'_{1j}I$, we have by induction hypothesis, and $M_{1j} = (-1)^{1+j}detM'_{1j} = (-1)^{1+j}\big(detA'_{1j} + \big(\det(A'_{1j}+B'_{1j}) - \det A'_{1j}\big)I\big)$. Hence, we get that

$$\begin{aligned} \det(\mathcal{M}) &= m_{11}(detA'_{11} + (\det(A'_{11}+B'_{11}) - \det A'_{11})I) \\ &\qquad - m_{12}(detA'_{12} + (\det(A'_{12}+B'_{12}) - \det A'_{12})I) \\ &\quad + \cdots + m_{1n}(-1)^{1+n}(detA'_{1n} + (\det(A'_{1n}+B'_{1n}) - \det A'_{1n})I) \\ &= m_{11}detA'_{11} - m_{12}detA'_{12} + \cdots + m_{1n}(-1)^{1+n}detA'_{1n} \\ &\quad + (m_{11}\det(A'_{11}+B'_{11}) - m_{12}\det(A'_{12}+B'_{12}) + \cdots + m_{1n}(-1)^{1+n}\det(A'_{1n}+B'_{1n}) \\ &\qquad - (m_{11}detA'_{11} - m_{12}detA'_{12} + \cdots + m_{1n}(-1)^{1+n}detA'_{1n}))I \\ &= det\mathcal{A} + (\det(\mathcal{A}+\mathcal{B}) - det\mathcal{A})I. \end{aligned}$$

So, theorem is true for all $n \in Z^+$.

We can write the following theorem examining the existence of the matrix M^{-1}. Note that if $N(a+bI) = 0$ for any $a+bI \in R[I]$, we have $a(a+b) = 0$. So, we see that $a = 0$ or $a+b = 0$. Then $a+bI$ is a neutrosophic number such that bI or $a - aI$. Also, we see that $N(detM) = detA.det(A+B)$ where $M = A + BI$ by Theorem 3.10, Definition 2.1 and Definition 2.2.

Theorem 3.11 Let $\mathcal{A}$ and $\mathcal{B}$ be $n \times n$ real matrix and $\mathcal{M} = \mathcal{A} + \mathcal{B}I$. Then

$N(det\mathcal{M}) \neq 0$ if and only if $\mathcal{M}$ is invertible.

Proof. Let $N(det\mathcal{M}) \neq 0$. Then we have $det\mathcal{A} \neq 0$ and $det(\mathcal{A}+\mathcal{B}) \neq 0$. Hence $det\mathcal{M} \neq 0$. We know that $\mathcal{M}.Adj(\mathcal{M}) = det\mathcal{M}.I_n$. Hence it is seen that $\mathcal{M}\frac{1}{det\mathcal{M}}Adj(\mathcal{M}) = I_n$. Say $K = \frac{1}{det\mathcal{M}}Adj(\mathcal{M})$. Since $\dfrac{1}{det\mathcal{M}} = \dfrac{\overline{det\mathcal{M}}}{det\mathcal{M}.\overline{det\mathcal{M}}} = \dfrac{\overline{det\mathcal{M}}}{N(det\mathcal{M})} \in R[I]$, all entries of the matrix K are neutrosophic real numbers and $K = \mathcal{M}^{-1}$. So $\mathcal{M}$ is invertible matrix. Conversely, let $\mathcal{M}$ is invertible matrix. Then there exists a neutrosophic matrix $N = C + DI$ such that $\mathcal{M}N = N\mathcal{M} = I_n$. Hence since $(\mathcal{A}+\mathcal{B}I)(C+DI) = I_n$ and $(C+DI)(\mathcal{A}+\mathcal{B}I) = I_n$, we have $\mathcal{A}C = C\mathcal{A} = I_n$ and $(\mathcal{A}+\mathcal{B})(C+D) = (C+D)(\mathcal{A}+\mathcal{B}) = I_n$. So $\mathcal{A}$ and $\mathcal{A}+\mathcal{B}$ are invertible real matrices. In this case, since $det\mathcal{A} \neq 0$ and $\det(\mathcal{A}+\mathcal{B}) \neq 0$, we obtain $N(\mathcal{M}) = det\mathcal{A}.\det(\mathcal{A}+\mathcal{B}) \neq 0$. Note that, in case $N(\det\mathcal{M}) = 0$ (this includes $det\mathcal{M} = 0$), suppose that $\mathcal{M}$ is invertible. Then since $\mathcal{M}.\mathcal{M}^{-1} = I_n$, we have $det(\mathcal{M}.\mathcal{M}^{-1}) = 1$. Hence $\det(\mathcal{M})\cdot\det(\mathcal{M}^{-1}) = 1$. Then the equality $\mathrm{N}(\det(\mathcal{M})\cdot$

$\det(\mathcal{M}^{-1})) = \underbrace{N(det\mathcal{M})}_{0}.N(det\mathcal{M}^{-1}) = N(1) = 1$ is not true. So $\mathcal{M}$ is not an invertible matrix.

Example 3.12 i) Let $M = \begin{bmatrix} 1+I & 3-I \\ 0 & 0 \end{bmatrix}$. Then since $N(detM) = N(0) = 0$, M is not invertible.

ii) Let $M = \begin{bmatrix} 2-I & 1+I \\ 3 & 4I \end{bmatrix}$**.** Then $detM = -3 + I \neq 0$ and $N(detM) = 6 \neq 0$. Hence M is an invertible matrix and

$$M^{-1} = \frac{1}{-3+I} \cdot \begin{bmatrix} 4I & -1-I \\ -3 & 2-I \end{bmatrix}$$

$$= \frac{-2-I}{(-3+I)(-2-I)} . \begin{bmatrix} 4I & -1-I \\ -3 & 2-I \end{bmatrix}$$

$$= \frac{1}{6} \cdot (-2-I). \begin{bmatrix} 4I & -1-I \\ -3 & 2-I \end{bmatrix}$$

$$= \frac{1}{6} \cdot \begin{bmatrix} -12I & 2+4I \\ 6+3I & -4+I \end{bmatrix}$$

iii) Let $M = \begin{bmatrix} 3I & 0 \\ 0 & 2I \end{bmatrix}$. Then $detM = 6I \neq 0, N(detM) = 0$. There do not exist any inverse of M by Theorem 3.11. As a second way, if there exists an inverse of the matrix M such that $M^{-1} = \begin{bmatrix} a+bI & c+dI \\ e+fI & g+hI \end{bmatrix}$, since $M.M^{-1} = I$, we get $3I(a+bI) = 1$ and $2I(g+hI) = 1$. But there do not exist $a, b \in R$ and $g, h \in R$ satisfying the above equations by Theorem 3.4. So, the matrix M do not have any inverse.

Remark 1. By Theorem 3.11 and Example 3.12 (iii), we see that the condition $detM \neq 0$ is not sufficient for M to be an invertible matrix. Therefore, Theorem 3.4 in [8] is not entirely correct.

Now, let $\mathcal{A}$ and $\mathcal{B}$ be $n \times n$ real matrix and $\mathrm{C} = D + EI$ be $n \times 1$ be column vector and $\mathcal{M} = \mathcal{A} + \mathcal{B}I$. Consider the systems of neutrosophic linear equations $\mathcal{M}Z = C$.

Theorem 3.13 If $N(detM) \neq 0$, then the systems of neutrosophic linear equation $MZ = C$ has unique solution and this solution is $Z = M^{-1}C$.

Proof. By Theorem 3.11, M is an invertible matrix. Multiplying $MZ = C$ by M^{-1} from the left, we get $Z = M^{-1}C$. If $Z_1\ and\ Z_2$ are two solutions of $MZ = C$, then we have $MZ_1 = MZ_2$. Multiplying by M^{-1} from the left, we get $Z_1 = Z_2$.

The following Corollary states the solution vector $Z = X + YI$ of the systems of neutrosophic linear equation $MZ = C$ in terms of A, B, C and D where $M = A + BI$ and $C = D + EI$.

Corollary 3.14 Let $\mathcal{A}$ and $\mathcal{B}$ are $n \times n$ real matrices and $C\ and\ D$ are $n \times 1$ real column vector. Let $\mathcal{M} = \mathcal{A} + \mathcal{B}I$ be an $n \times n$ matrix and $\mathrm{C} = D + EI$ be $n \times 1$ be column vector. If $N(detM) \neq 0$, then the solution of the systems of neutrosophic linear equations $MZ = C$ is the vector $Z = X + YI$ where $X = \mathcal{A}^{-1}D$ and $Y = (\mathcal{A} + \mathcal{B})^{-1}(D + E) - \mathcal{A}^{-1}D$.

Proof. By Theorem 3.13, we have $Z = M^{-1}C$. Hence using Theorem 2.3, we obtain that

$$\begin{aligned} Z &= X + YI \\ &= M^{-1}C \\ &= (\mathcal{A}^{-1} + ((\mathcal{A}+\mathcal{B})^{-1} - \mathcal{A}^{-1})I)(D + EI) \\ &= \mathcal{A}^{-1}D + (\mathcal{A}^{-1}E + (\mathcal{A}+\mathcal{B})^{-1}D - \mathcal{A}^{-1}D + (\mathcal{A}+\mathcal{B})^{-1}E - \mathcal{A}^{-1}E)I \\ &= \mathcal{A}^{-1}D + ((\mathcal{A}+\mathcal{B})^{-1}(D+E) - \mathcal{A}^{-1}D)I. \end{aligned}$$

Example 3.15 Consider the systems of neutrosophic equations

$$(2-I)Z_1 + (1+I)Z_2 = 1 + 2I$$

$$3Z_1 + 4IZ_2 = 3 + 4I.$$

Then $M = \begin{bmatrix} 2-I & 1+I \\ 3 & 4I \end{bmatrix} = \underbrace{\begin{bmatrix} 2 & 1 \\ 3 & 0 \end{bmatrix}}_{A} + \underbrace{\begin{bmatrix} -1 & 1 \\ 0 & 4 \end{bmatrix}}_{B} I, C = \begin{bmatrix} 1+2I \\ 3+4I \end{bmatrix} = \underbrace{\begin{bmatrix} 1 \\ 3 \end{bmatrix}}_{D} + \underbrace{\begin{bmatrix} 2 \\ 4 \end{bmatrix}}_{E} I,$
$Z = \begin{bmatrix} Z_1 \\ Z_2 \end{bmatrix}$. If we use Theorem 3.13, since $M^{-1} = \frac{1}{6}\begin{bmatrix} -12I & 2+4I \\ 6+3I & -4+I \end{bmatrix}$, we have $Z = M^{-1}C = \begin{bmatrix} 1 \\ -1+2I \end{bmatrix}$. If we use the Corollary 3.14, since $A^{-1} = \frac{1}{3}\begin{bmatrix} 0 & -1 \\ -3 & 2 \end{bmatrix}$, $(A+B)^{-1} = -\frac{1}{2}\begin{bmatrix} 4 & -2 \\ -3 & 1 \end{bmatrix}$, we have

$$X = A^{-1}D = \begin{bmatrix} 1 \\ -1 \end{bmatrix}, Y = (A+B)^{-1}(D+E) - A^{-1}D = \begin{bmatrix} 0 \\ 2 \end{bmatrix}.$$

Hence $Z = X + YI = \begin{bmatrix} 1 \\ -1+2I \end{bmatrix}$.

In Theorem 3.13 and Corollary 3.14, we investigate the solutions of the systems of neutrosophic linear equations $MZ = C$ where $N(detM) \neq 0$. If $N(detM) = 0$, since M has not an inverse, we can not find a solution using the matrix M^{-1}. In case $N(detM) = 0$, we can write the following Theorem:

Theorem 3.16 If $detM \neq 0$ but $N(detM) = 0$, then the systems of neutrosophic linear equations $MZ = C$ has either more than one solution or no solution.

Proof. Since $detM \neq 0$ and $N(detM) = 0$, we can use Cramer's rule. We know that ith component of the solution Z is $Z_i = \frac{\det M_i}{\det M}$ for $i = 1,2,\dots,n$ where M_i is the matrix obtained from M by replacing the ith column of M by the vector C. If $detM | detM_i$, then $Z_i \in R[I]$ for all i by Theorem 3.4. Hence $MZ = C$ has more than one solution. If $detM \nmid detM_i$ for some i, then $Z_i \notin R[I]$. Hence $MZ = C$ has no solution.

Example 3.17 For the system

$$\begin{aligned} 3IX + (1+I)Y &= 6I \\ 2IY &= 4I, \end{aligned}$$

$M = \begin{bmatrix} 3I & 1+I \\ 0 & 2I \end{bmatrix}$, $C = \begin{bmatrix} 6I \\ 4I \end{bmatrix}$, $detM = 6I \neq 0, N(detM) = 0$. Then, by the second equation, we have $Y = \frac{4I}{2I} = p + qI$ $(p + q = 2, p, q \in R)$. Substituting it in the first equation, we see that $X = \frac{-p+(4-q)I}{3I}$. In this case, if $p=0$, we obtain $3I | (4-q)I$ and $X = \frac{(4-q)I}{3I} \in R[I]$. (For $p \neq 0$, since $3I \nmid -p + (4-q)I$, there are no solution) Hence since $p + q = 2$, we have $q = 2$ and $Y = 2I$. So, the solutions of the given systems of the neutrosophic linear equations are

$$X = \frac{2I}{3I} = \left\{u + vI : u, v \in R, u + v = \frac{2}{3}\right\}$$
$$Y = 2I.$$

Note that, if $detA \neq 0$, then the system $AX = B$ has only one solution in real linear algebra.

Example 3.18 The system

$$3IX + (1 + I)Y = 6I$$
$$2IY = 1 + 4I$$

has no solutions since $2I \nmid 1 + 4I$.

Corollary 3.19 Consider the system $MZ = C$ where M is a neutrosophic $n \times n$ square matrix and C is an $n \times 1$ be neutrosophic column vector.
i) If $N(detM) \neq 0$, then the systems of neutrosophic linear equation $MZ = C$ has unique solution. (Theorem 3.13)
ii) If $detM \neq 0$ but $N(detM) = 0$, then the systems of neutrosophic linear equations $MZ = C$ has either more than one solution or no solution. (Theorem 3.16)
iii) If $detM = 0$, the systems of equations $MZ = C$ has either more than one solution or no solution.

Remark 2. Considering Corollary 3.18 and the examples above, in Alhasan's article ([9]), it can be seen that there are some errors in the results and some examples in Section 4.2. The system in Example 4.2.2 in Alhasan's article has unlimited number solutions:

$$x = \frac{13\mathrm{I}}{19\mathrm{I}} = \left\{u + vI \,\middle|\, u, v \in R, u + v = \frac{13}{19}\right\}$$
$$y = -\frac{1}{19}\mathrm{I}$$

are the solutions of the equation of the systems:

$$2Ix + 7y = I$$

$$3Ix + y = 2I.$$

4. Conclusion

In this paper, we firstly researched the subject in which cases the division of two neutrosophic real numbers yields a new neutrosophic number. Then, from a different perspective, the solution cases of a neutrosophic linear equation with one unknown were examined. After calculating the determinant of a square matrix and giving the necessary and sufficient conditions for a square matrix to be invertible, the solution conditions of the systems of equations with the number of unknowns equal to the number of equations were examined. In doing so, we used the real and neutrophic parts of a neutrophisophic matrix. Also, we gave some important examples to clarify the theory.

Authorship contribution statement

Y. Çeven: Supervision/Observation/Advice, Conceptualization;

A. I. Sekmen: Methodology, Original Draft Writing.

Declaration of competing interest

The authors declare that they have no known competing financial interests or personal relationships that could have appeared to influence the work reported in this paper.

Ethics Committee Approval and/or Informed Consent Information

As the authors of this study, we declare that we do not have any ethics committee approval and/or informed consent statement.

References

[1] F. Smarandache, Neutrosophy: Neutrosophic Probability, Set and Logic, Rehoboth: USA, American Research Press, 72 pages, 1998.

[2] M. Abobala, "Partial foundation of neutrosophic number theory", *Neutrosophic Sets and Systems*, 39, 120-132, 2021.

[3] Y. Çeven, Ş. S. Tekin, "Some properties of neutrosophic ıntegers", *Kırklareli University Journal of Engineering and Science,* 6(1), 50-59, 2020.

[4] M. Abobala, "On some neutrosophic algebraic equations", *Journal of New Theory,* 33, 26-32,2020.

[5] S. A. Edalatpanah, "Systems of neutrosophic linear equations", *Neutrosophic Sets and Systems,* 33, 92-104, 2020.

[6] H. Sankari, M. Abobala, "Neutrosophic linear diophantine equations with two variables", *Neutrosophic Sets and Systems,* 38, 399-408, 2020.

[7] A. N. Yurttakal, Y. Çeven, "Some elementary properties of neutrosophic ıntegers", *Neutrosophic Sets and Systems,* 41, 106-112, 2021.

[8] M. Abobala, A. Hatip, N. Olgun, S. Broumi, A. A. Salama, H. E. Khaled, "The algebraic creativity in the neutrosophic square matrices", *Neutrosophic Sets and Systems, 40, 1-11,2021.*

[9] Y. A. Alhasan, "Types of system of the neutrosophic linear equations and Cramer's rule", *Neutrosophic Sets and Systems,* 45, 402-413, 2021.

[10] M. Abobala, M. Bal, A. Hatip, "A review on recent advantages in algebraic theory of neutrosophic matrices", *International Journal of Neutrosophic Science,* 17(1), 68-86, 2021.

Süleyman Demirel Üniversitesi Fen Edebiyat Fakültesi Fen Dergisi https://dergipark.org.tr/sdufeffd
Süleyman Demirel University Faculty of Arts and Sciences Journal of Science e-ISSN: 1306-7575
Research Article, 2023, 18(3): 213-222, DOI: 10.29233/sdufeffd.1312399

Evaluation of the Gaunt Coefficients by Using Recurrence Relations for Spherical Harmonics

Selda Özay

Department of Physics, Faculty of Science, Ondokuz Mayıs University, 55139, Samsun, TURKEY
https://orcid.org/0000-0001-5205-4519
corresponding author: seldaozay@hotmail.com

(Received: 09.06.2023, Accepted: 12.09.2023, Published: 23.11.2023)

Abstract: The Gaunt coefficient is one of the important coefficients to be known for calculating molecular integrals in quantum theory of coupling of three angular momenta. Generally, these coefficients are calculated analytically by using the properties of the associated Legendre polynomials. In this study, Gaunt coefficients were calculated algebraically by using the recurrence relations and orthogonality conditions of spherical harmonics and different mathematical expressions were obtained from known analytical expressions for Gaunt coefficients in terms of factorial functions or binomial coefficients. By using the program written in the Mathematica programming language, both the analytical expressions and the algebraic expressions were calculated, and the numerical results obtained were compared. Numerical results are in quite agreement with the literature and each other.

Key words: Clebsch – Gordan coefficients, Vector coupling coefficients, Gaunt coefficients.

1. Introduction

Since atoms and molecules are quantum mechanical systems, in order to study their electronic structure, physical and chemical properties, the Hamiltonian operator of the system must be written, and the Schrödinger equation of the system must be solved. The repulsive Coulomb potential energy term between electrons in atoms and molecules depends on the distances between two electrons and is inversely proportional to the distance term dependent on the coordinates of both electrons. Therefore, this interaction term between electrons cannot be written separately depending on the coordinates of individually electrons. This makes it impossible to solve the Schrödinger equation analytically for multi-electron systems without using approximate methods. It should be known that there is no mathematical difficulty in single-electron systems. The most suitable coordinate system to solve the Schrödinger equation in such systems is spherical coordinates. If spherical coordinates are used, the kinetic energy operators of individual particles are written as

$$T = -\frac{\hbar^2}{2\,m}\left\{\frac{1}{r^2}\frac{\partial}{\partial r}\left(r^2\frac{\partial}{\partial r}\right) - \frac{L^2}{\hbar^2\,r^2}\right\} \tag{1}$$

the form of the square of the angular momentum operator.

In central field problems, since the Hamiltonian operator of the system commute with the square of the angular momentum and the component z of the angular momentum. The spherical harmonics are the eigenfunctions of L^2 and also the eigenfunctions of the Hamiltonian operator. Therefore, the angular part of the spatial wave functions of all atoms and molecules is composed of spherical harmonics.

Spherical harmonics are given by associated Legendre polynomials, P_l^m, as follows [1]

$$Y_l^m(\theta,\phi) = (-1)^m \sqrt{\frac{2\,l+1}{4\pi}\,\frac{(l-m)\,!}{(l+m)\,!}}\; P_l^m(cos\theta)\, e^{i\,m\,\phi}\,, \qquad m\, \geq 0 \tag{2.a}$$

Spherical harmonics for negative superscript is given by

$$Y_l^{-|m|}(\theta,\phi) = (-1)^m \left[Y_l^{|m|}(\theta,\phi)\right]^* \tag{2.b}$$

Spherical harmonics have a very wide range of applications not only in atomic and molecular physics, but also in solid-state physics, nuclear physics, astrophysics, and many areas of chemistry.

In the second part of this study, functions consisting of the product of spherical harmonics and trigonometric functions are written again in terms of spherical harmonics. In the third part, the Gaunt coefficients are calculated algebraically using the integral expression for the Gaunt coefficients and the recurrence relations of the spherical harmonics in the second part. The numerical results of the obtained mathematical expression are calculated with the Mathematica program, the results are presented as Table 1 in the fourth part. The accuracy of the results found was checked using the orthogonality relation and compared with the literature.

2. Material and Method

2.1. Recurrence relations for spherical harmonics

In multipole moment transitions that occur as a result of the interaction of atoms with the external electric and magnetic fields, the products of one spherical harmonic and trigonometric function (or product of trigonometric and exponential function) emerge. To calculate multipole moment integrals, it is possible to write recurrence relations for spherical harmonics using the recurrence relations provided by the associated Legendre polynomials. Some of these relations are given below [1, 2].

$$cos\theta\; Y_L^M(\theta,\phi) = \sqrt{\tfrac{(L-M+1)(L+M+1)}{(2L+1)(2L+3)}}\; Y_{L+1}^M + \sqrt{\tfrac{(L-M)(L+M)}{(2L-1)(2L+1)}}\; Y_{L-1}^M \tag{3}$$

$$sin\theta\; Y_L^M(\theta,\phi)\; e^{i\,\phi} = -\sqrt{\tfrac{(L+M+1)(L+M+2)}{(2L+1)(2L+3)}}\; Y_{L+1}^{M+1} + \sqrt{\tfrac{(L-M-1)(L-M)}{(2L-1)(2L+1)}}\; Y_{L-1}^{M+1} \tag{4}$$

$$sin\theta\; Y_L^M(\theta,\phi)\; e^{-i\,\phi} = \sqrt{\tfrac{(L-M+1)(L-M+2)}{(2L+1)(2L+3)}}\; Y_{L+1}^{M-1} - \sqrt{\tfrac{(L+M-1)(L+M)}{(2L-1)(2L+1)}}\; Y_{L-1}^{M-1} \tag{5}$$

$$\begin{aligned}(2L-1)(2L+3)\cos^2\theta\; Y_L^M(\theta,\phi) = {} & (2l-1)\sqrt{\tfrac{((L+1)^2-M^2)((L+2)^2-M^2)}{(2L+1)(2L+5)}}\; Y_{L+2}^M \\ & +[2L(L+1)-2M^2-1]\; Y_L^M \\ & +(2l+3)\sqrt{\tfrac{(L^2-M^2)((L-1)^2-M^2)}{(2L+1)(2L-3)}}\; Y_{L-2}^M\end{aligned} \tag{6}$$

$$(2L-1)(2L+3)\; sin\theta\;\; \cos\theta\; e^{i\phi}\; Y_L^M(\theta,\phi)\; =$$

$$-(2l-1)\sqrt{\frac{((L+1)^2-M^2)(L+M+2)(L+M+3)}{(2L+1)(2L+5)}}\;Y_{L+2}^{M+1}$$

$$-(2M+1)\sqrt{L(L+1)-M(M+1)}\;Y_{L}^{M+1} \tag{7}$$

$$+(2l+3)\sqrt{\frac{(L^2-M^2)(L-M-1)(L-M-2)}{(2L+1)(2L-3)}}\;Y_{L-2}^{M+1}$$

$$(2L-1)(2L+3)\,sin\theta\;\cos\theta\, e^{-i\phi}\,Y_L^M(\theta,\phi)\;=$$

$$(2L-1)\sqrt{\frac{((L+1)^2-M^2)(L-M+2)(L-M+3)}{(2L+1)(2L+5)}}\;Y_{L+2}^{M-1}$$

$$-(2M-1)\sqrt{L(L+1)-M(M-1)}\;Y_{L}^{M-1} \tag{8}$$

$$-(2l+3)\sqrt{\frac{(L^2-M^2)(L+M-1)(L+M-2)}{(2L+1)(2L-3)}}\;Y_{L-2}^{M-1}$$

$$(2L-1)(2L+3)\;\sin^2\theta\;\,e^{2i\phi}\,Y_L^M(\theta,\phi)\;=$$

$$\frac{2L-1}{\sqrt{(2L+1)(2L+5)}}\sqrt{\frac{(L+M+4)!}{(L+M)!}}\;Y_{L+2}^{M+2}$$

$$+\frac{2L+3}{\sqrt{(2L+1)(2L-3)}}\sqrt{\frac{(L-M)!}{(L-M-4)!}}\;Y_{L-2}^{M+2} \tag{9}$$

$$-2\sqrt{\frac{(L+M+2)!(L-M)!}{(L-M-2)!(L+M)!}}\;Y_{L}^{M+2}$$

$$(2L-1)(2L+3)\;\sin^2\theta\;\,e^{-2i\phi}\,Y_L^M(\theta,\phi)\;=$$

$$\frac{2L-1}{\sqrt{(2L+1)(2L+5)}}\sqrt{\frac{(L-M+4)!}{(L-M)!}}\;Y_{L+2}^{M-2}$$

$$+\frac{2L+3}{\sqrt{(2L+1)(2L-3)}}\sqrt{\frac{(L+M)!}{(L+M-4)!}}\;Y_{L-2}^{M-2} \tag{10}$$

$$-2\sqrt{\frac{(L-M+2)!(L+M)!}{(L+M-2)!(L-M)!}}\;Y_{L}^{M-2}$$

In many-particle systems, the total angular momentum of the system is composed of the vector sum of the orbital angular momenta of the particles. The situation is a bit more complicated in atoms and molecules. Because, in addition to the orbital angular momenta of the electrons, there are also spin angular momenta that are independent of the orbital motion. In atoms and molecules, the total angular momentum which is expressed of the sum of these two angular momenta, needs to be investigated. ***H*** Hamiltonian operator of the system commutes with L^2, S^2, L_z and S_z so that these are constants of motion and corresponding quantum numbers l, s, m_l and m_s are all *good quantum numbers*. It is possible to write the wave function of the system that is composed of the individual wave functions of the electrons (superposition principle). In this case, the linear combination coefficients are called Clebsch – Gordan coefficients [2] and are defined in terms of $F(a,b)$ binomial coefficients [3] as follows.

$$C^{L\,M}_{l_1m_1,l_2m_2} = \langle l_1m_1\; l_2m_2|l_1l_2LM\rangle = \langle l_1l_2LM|l_1m_1\; l_2m_2\rangle$$

$$= \delta_{M,m_1+m_2}\left[\frac{F(2l_1,l_1+l_2-L)\,F(2l_2,l_1+l_2-L)}{F(l_1+l_2+L+1,l_1+l_2-L)F(2l_1,l_1-m_1)F(2l_2,l_2-m_2)F(2L,L-M)}\right]^{1/2} \tag{11}$$

$$\sum\nolimits_z\{(-1)^zF(l_1+l_2-L,z)$$

$$F(l_1-l_2+L,l_1-m_1-z)F(-l_1+l_2+L,l_2+m_2-z)\}$$

where the summation index *z* is described in Refs. [2, 3].

To calculate the Clebsch – Gordan coefficients, the raising/lowering operators of the angular momentum operators are used. This is quite laborious task for high quantum numbers. In the use of computers, there is a problem of memory stacking. Clebsch – Gordan coefficients have been calculated analytically by many researchers using analytical methods, and the results are generally given in terms of factorial functions or binomial coefficients [4-12].

Clebsch – Gordan coefficients are the most general coefficients related to rotational motion. Therefore, all other coefficients related to rotation are written in terms of Clebsch – Gordan coefficients. One of these rotation coefficients is the Gaunt coefficient. Gaunt coefficients are defined as the product of three spherical harmonics by following form in terms of Clebsch – Gordan coefficients [13-19].

For $\Delta M = m_1 - m_2$

$$Y^{L\,M}_{l_1m_1,l_2m_2} = \int_0^{2\,\pi}\int_0^{\pi}\left(Y_{l_1}^{m_1}\right)^*\, Y_{l_2}^{m_2}\, Y_L^M\, sin\theta\; d\theta\; d\phi \tag{12}$$

$$= (-1)^{m_2}\sqrt{\frac{(2\,l_1+1)\,(2\,l_2+1)}{4\,\pi\,(2L+1)}}\; C^{L0}_{l_10,l_20}C^{LM}_{l_1m_1,l_2-m_2}$$

and for $\Delta M = m_1 + m_2$

$$Y^{L\,M}_{l_1m_1,l_2m_2} = \int_0^{2\,\pi}\int_0^{\pi} Y_{l_1}^{m_1}\, Y_{l_2}^{m_2}\,(Y_L^M)^*\, sin\theta\; d\theta\; d\phi \tag{13}$$

$$= \sqrt{\frac{(2\,l_1+1)\,(2\,l_2+1)}{4\,\pi\,(2L+1)}}\; C^{L0}_{l_10,l_20}C^{LM}_{l_1m_1,l_2m_2}$$

Using the Clebsch – Gordan coefficients given in Refs. [5, 7, 20] in terms of factorial and binomial coefficients and Eqs. (12, 13), the Gaunt coefficients are written in terms of generalized hypergeometric functions whose argument is equal to 1 [21].

$$Y^{L\,M}_{l_1m_1,l_2m_2} = (-1)^{\frac{3l_1+l_2-L-2m_1}{2}}\left(\frac{1+(-1)^{l_1+l_2+L}}{2}\right)\sqrt{\frac{(2l_1+1)(2l_2+1)(2L+1)}{4\pi}}$$

(14)

$$\frac{F\left(l_2,\frac{l_2+L-l_1}{2}\right) F\left(\frac{l_1+l_2+L}{2}, l_2\right) F(l_2+L-m_1,l_2-L+m_1)}{(l_1+l_2+L+1)\ F(2L,2m_1)}$$

$$\sqrt{\frac{F(-l_1+l_2+L,L)\ F(2L,l_1-l_2+L)\ F(L+M,L-M)\ F(2m_1+2m_2,2m_1)}{F(l_1+l_2+L,2L)\ F(2L,L)\ F(L,l_2-l_1)\ F(l_1+l_2+L,2L)\ F(l_2+m_2,l_2-m_2)}}$$

$${}_3F_2\left[\begin{matrix} l_1+m_1+1,-l_1+\ m_1,-L+M \\ -l_1-L+m_1,\ l_2-\ L+\ m_1+1 \end{matrix}\middle|\, 1\right]$$

In this study, Gaunt coefficients were calculated algebraically using the recurrence relations of spherical harmonics and numerical values were obtained by using the Mathematica programming language [22].

2.2. Gaunt coefficients

According to Eq. (12 or 13), the expansion of spherical harmonics given by Eq. (2) should be used to calculate the Gaunt coefficients analytically. Since the double integral over a sphere (both θ and ϕ limits are constant) is product, the Gaunt coefficients are written as the product of two independent integrals. While it is difficult to calculate integrals via the associated Legendre polynomials, it is quite easy to calculate the integral via the azimuthal angle which gives the necessary selection rules for the Gaunt coefficients to be nonzero. The selection rules are $\Delta M = m_1 \pm m_2$ according to the spherical harmonic chosen as the complex. If the Gaunt coefficients are calculated using the Eqs. (12-14), these selection rules must be taken into account. Because, when the condition $\Delta M = m_1 - m_2$ is satisfied, the Gaunt coefficient is different from zero but the Clebsch – Gordan coefficient becomes zero unless $m_2 = -m_2$ in the expressions for the Clebsch – Gordan coefficient.

When algebraic methods will be used instead of analytical methods to calculate the Gaunt coefficients, recurrence and orthogonality relations of spherical harmonics given by Eqs. (3-10) will be used. For $l_2 = 1$ and $m_2 = 0$, if special values of spherical harmonics for this quantum sets is used, Eq. (12) rewritten as follows

$$Y^{L\,M}_{l_1 m_1,10} = \sqrt{\frac{3}{4\pi}} \int_0^{2\,\pi} \int_0^{\pi} \left(Y_{l_1}^{m_1}\right)^* \left(cos\theta\ Y_L^M\right) sin\theta\ d\theta\ d\phi$$

In this equation, if the recurrence relation given by Eq. (3) is replaced with the product of trigonometric function and spherical harmonics, the orthogonality relation of spherical harmonics is used in the integral expression and then obtained.

$$Y^{LM}_{l_1 m_1,10} = \sqrt{3}\left\{\sqrt{\frac{(L-M+1)(L+M+1)}{(2L+1)(2L+3)}}\ Y^{L+1M}_{l_1 m_1,00} + \sqrt{\frac{(L-M)(L+M)}{(2L-1)(2L+1)}}\ Y^{L-1M}_{l_1 m_1,00}\right\} \tag{15}$$

In order to calculate the $Y^{LM}_{l_1 m_1,10}$ Gaunt coefficients, it is sufficient to give only L and M quantum numbers to this obtained equation.

By changing the values of the l_2 and m_2 quantum numbers and repeating the above operations, the Gaunt coefficients for different quantum sets can be obtained as follows:

$$Y^{LM}_{l_1 m_1,11} = \sqrt{3/2}\left\{\sqrt{\frac{(L+M+1)(L+M+2)}{(2L+1)(2L+3)}}\ Y^{L+1M+1}_{l_1 m_1,00} - \sqrt{\frac{(L-M)(L-M-1)}{(2L-1)(2L+1)}}\ Y^{L-1M+1}_{l_1 m_1,00}\right\} \tag{16}$$

(17)

$$Y^{LM}_{l_1m_1,1-1} = \sqrt{3/2}\left\{\sqrt{\frac{(L-M+1)(L-M+2)}{(2L+1)(2L+3)}}\;Y^{L+1M-1}_{l_1m_1,00} - \sqrt{\frac{(L+M)(L+M-1)}{(2L-1)(2L+1)}}\;Y^{L-1M-1}_{l_1m_1,00}\right\}$$

$$\begin{aligned} Y^{LM}_{l_1m_1,20} = \sqrt{5}\Bigg\{\frac{3}{2(2L-1)(2L+3)}\Bigg[&(2L-1)\sqrt{\frac{((L+1)^2-M^2)((L+2)^2-M^2)}{(2L+1)(2L+5)}}\;Y^{L+2M}_{l_1m_1,00}\\ &+(2L(L+1)-2M^2-1)\;Y^{LM}_{l_1m_1,00}\\ &+(2L+3)\sqrt{\frac{(L^2-M^2)((L-1)^2-M^2)}{(2L+1)(2L-3)}}\;Y^{L-2M}_{l_1m_1,00}\Bigg]-\frac{1}{2}\;Y^{LM}_{l_1m_1,00}\Bigg\} \end{aligned} \tag{18}$$

$$\begin{aligned} Y^{LM}_{l_1m_1,21} = 3\sqrt{\frac{5}{6}}\Bigg\{\frac{1}{(2L-1)(2L+3)}\Bigg[&(2L-1)\sqrt{\frac{((L+1)^2-M^2)(L+M+2)(L+M+3)}{(2L+1)(2L+5)}}\;Y^{L+2M+1}_{l_1m_1,00}\\ &+(2M+1)\sqrt{L(L+1)-M(M+1)}\;Y^{LM+1}_{l_1m_1,00}\\ &-(2L+3)\sqrt{\frac{(L^2-M^2)(L-M-1)(L-M-2)}{(2L+1)(2L-3)}}\;Y^{L-2M+1}_{l_1m_1,00}\Bigg]\Bigg\} \end{aligned} \tag{19}$$

$$\begin{aligned} Y^{LM}_{l_1m_1,2-1} = 3\sqrt{\frac{5}{6}}\Bigg\{\frac{1}{(2L-1)(2L+3)}\Bigg[&(2L-1)\sqrt{\frac{((L+1)^2-M^2)(L-M+2)(L-M+3)}{(2L+1)(2L+5)}}\;Y^{L+2M-1}_{l_1m_1,00}\\ &-(2M-1)\sqrt{L(L+1)-M(M-1)}\;Y^{LM-1}_{l_1m_1,00}\\ &-(2L+3)\sqrt{\frac{(L^2-M^2)(L+M-1)(L+M-2)}{(2L+1)(2L-3)}}\;Y^{L-2M-1}_{l_1m_1,00}\Bigg]\Bigg\} \end{aligned} \tag{20}$$

$$\begin{aligned} Y^{LM}_{l_1m_1,22} = 3\sqrt{\frac{5}{24}}\Bigg\{\frac{1}{(2L-1)(2L+3)}\Bigg[&\frac{2L-1}{\sqrt{(2L+1)(2L+5)}}\sqrt{\frac{(L+M+4)!}{(L+M)!}}\;Y^{L+2M+2}_{l_1m_1,00}\\ &+\frac{2L+3}{\sqrt{(2L+1)(2L-3)}}\sqrt{\frac{(L-M)!}{(L-M-4)!}}\;Y^{L-2M+2}_{l_1m_1,00}\\ &-2\sqrt{\frac{(L+M+2)!(L-M)!}{(L-M-2)!(L+M)!}}\;Y^{LM+2}_{l_1m_1,00}\Bigg]\Bigg\} \end{aligned} \tag{21}$$

$$\begin{aligned} Y^{LM}_{l_1m_1,2-2} = 3\sqrt{\frac{5}{24}}\Bigg\{\frac{1}{(2L-1)(2L+3)}\Bigg[&\frac{2L-1}{\sqrt{(2L+1)(2L+5)}}\sqrt{\frac{(L-M+4)!}{(L-M)!}}\;Y^{L+2M-2}_{l_1m_1,00}\\ &+\frac{2L+3}{\sqrt{(2L+1)(2L-3)}}\sqrt{\frac{(L+M)!}{(L+M-4)!}}\;Y^{L-2M-2}_{l_1m_1,00}\\ &-2\sqrt{\frac{(L-M+2)!(L+M)!}{(L+M-2)!(L-M)!}}\;Y^{LM-2}_{l_1m_1,00}\Bigg]\Bigg\} \end{aligned} \tag{22}$$

All Gaunt coefficients given by the Eqs. (15-22) are expressed in terms of the basic Gaunt coefficient defined as

$$Y^{LM}_{l_1 m_1,00} = \frac{1}{\sqrt{4\pi}} \delta_{l_1,L} \delta_{m_1,M} \tag{23}$$

3. Results

As can be seen from the Eqs. (15-22), it is possible to find the Gaunt coefficients numerically according to the given quantum sets by calculating the multipliers of the basic Gaunt coefficients. Given Eqs. (14 and 15-22) Gaunt coefficients were calculated by algorithm written in Mathematica programming language based on these formulas and the results are given in Table 1. The numerical values given in Table 1 are in agreement with Refs. [15, 16, 19 and 23].

Written program by using Eqs. (14 and 15-22) are run on Intel (R) Core (TM) i5-6200U CPU @ 2.30 Ghz computer for some sets of quantum numbers and the CPU times are found, and the results are given in seconds in Table 2. Since the computers used have different hardware, the CPU times are not compared with the literature.

Table 1. Gaunt coefficients for different sets of quantum numbers by using Eqs. (15-22 and 14).

l_1	m_1	l_2	m_2	l	m	$\frac{1}{\sqrt{\pi}}$ Eqs. (15-22)	Eq. (14)
10	5	0	0	10	5	1/2	0.2820947917738781
15	8	1	0	14	8	$\frac{1}{2}\sqrt{483/899}$	0.2067705997734994
25	-8	1	0	26	-8	$3/\sqrt{53}$	0.2324921981102874
20	13	1	1	19	12	$2\sqrt{33/533}$	0.2807685277668304
30	-15	1	1	31	-16	$-\frac{1}{2}\sqrt{1081/1281}$	-0.2591393410513699
40	18	1	-1	39	19	$\frac{1}{6}\sqrt{77/79}$	0.09283369360381252
15	5	1	-1	16	6	$-\frac{1}{2}\sqrt{21/31}$	-0.2321794983075630
12	6	2	0	10	6	$\frac{9}{46}\sqrt{17/7}$	0.1720224711335037
14	7	2	0	14	7	$\frac{7\sqrt{5}}{186}$	0.04747830014554065
6	5	2	0	8	5	$\frac{3}{\sqrt{170}}$	0.1298140972960522
64	50	2	1	62	49	$\frac{14}{635}\sqrt{12882/43}$	0.2152964127263299
8	4	2	1	8	3	$\frac{7}{19\sqrt{2}}$	0.1469787348847384
12	7	2	1	14	6	$-\frac{2}{9}\sqrt{14/19}$	-0.08711191655125597
38	15	2	-1	36	16	$\frac{1}{10}\sqrt{1219/365}$	0.1031051798730726
53	9	2	-1	53	10	$-\frac{19}{109}\sqrt{33/70}$	-0.06752430402507384

45	18	2	-1	47	19	$-\frac{8}{31}\sqrt{55/19}$	-0.2477181917039297
79	24	2	2	77	22	$\frac{5}{314}\sqrt{530553/1643}$	0.1614399541279544
83	65	2	2	85	63	$\frac{5}{338}\sqrt{77/167}$	0.005667160268083574
34	27	2	2	34	25	$-\frac{90\sqrt{61}}{4757}$	-0.08336799160917377
49	5	2	-2	47	7	$\frac{1}{194}\sqrt{12341/19}$	0.07411766167839542
24	9	2	-2	26	11	$\frac{5}{2}\sqrt{111/6307}$	0.1871178187511329
96	47	2	-2	96	49	$-\frac{84\sqrt{58}}{2483}$	-0.1453588997129646

Table 2. Computational times for some sets of quantum numbers in Table 1.

l_1	m_1	l_2	m_2	l	m	CPU (in seconds)	
						Eqs. (15-22)	Eq.(14)
10	5	0	0	10	5	0.234	0.266
30	-15	1	1	31	-16	0.296	0.218
64	50	2	1	62	49	0.328	0.282
53	9	2	-1	53	10	0.329	0.328
83	65	2	2	85	63	0.297	0.344
96	47	2	-2	96	49	0.266	0.329

4. Conclusion

To check the accuracy of the obtained numerical results, we used orthogonality relation for the Gaunt coefficients provided by following form [23]

$$\sum_{m_1=-l_1}^{l_1}\sum_{m_2=-l_2}^{l_2} Y^{L\,M}_{l_1 m_1, l_2 m_2} Y^{L'\,M'}_{l_1 m_1, l_2 m_2} = Y^{L\,0}_{l_1 0, l_2 0}\sqrt{\frac{(2\,l_1+1)\,(2\,l_2+1)}{4\,\pi\,(2L+1)}}\,\delta_{L,L'}\delta_{M,M'} \qquad (24)$$

Since the m_2 value is constant in the Eqs. (15-22), it is sufficient to add only summation via m_1 instead of the two sums in the orthogonality relation.

In this study, the advantage of the formulas obtained for the Gaunt coefficients is that they are valid when both selection rules of the form $\Delta M = m_1 \pm m_2$ are satisfied.

Authorship contribution statement

S. Özay: Conceptualization, Methodology, Software, Validation, Investigation, Original Draft Writing, Review and Editing.

Declaration of competing interest

The author declares that I have no known competing financial interests or personal relationships that could have appeared to influence the work reported in this paper.

Acknowledgment

As the author of this study, I declare that I do not have any support and thank you statement.

Ethics Committee Approval and/or Informed Consent Information

As the author of this study, I declare that I do not have any ethics committee approval and/or informed consent statement.

References

[1] G. B. Arfken and H. J. Weber, Mathematical Methods for Physicists, 4th ed., London, Academic Press, 1029 pages, 2001.
[2] D. A. Varshalovich, A. N. Moskalev and V. K. Khersonskii, Quantum Theory of Angular Momentum, Irreducible Tensors, Spherical Harmonics, Vector Coupling Coefficients, *3nj* Symbols, Singapore, World Scientific Publishing Co. Pte. Ltd, 514 pages, 1988.
[3] T. Shimpuku, "General Theory and Numerical Tables of Clebsch-Gordan Coefficients", *Progress of Theoretical Physics Supplement*, 13, 1-136, 1960.
[4] A. Bandzaitis and A. Yutsis, "Once more on the formulas for the Clebsch-Gordan coefficients", Lietuvos Fiz. Rinkinys, 4, 45-49, 1964.
[5] V. A. Fock, "New deduction of the vector model", JETP 10, 383-393, 1940.
[6] S. D. Majumdar, "The Clebsch-Gordan coefficients", *Progress of Theoretical Physics*, 20(6), 798-803, 1958.
[7] G. Racah, "Theory of complex spectra. II", *Physical Review*, 62(9), 438-462, 1942.
[8] A. R. Edmonds, Angular Momentum in Quantum Mechanics, 2nd ed., New Jersey, Princeton University Press, 146 pages, 1960.
[9] M. E. Rose, Elementary Theory of Angular Momentum, New York, John Wiley&Sons, 248 pages, 1957.
[10] R. N. Zare, Angular Momentum, Understanding Spatial Aspects in Chemistry and Physics, New York, John Wiley&Sons, 349 pages, 1988.
[11] E. U. Condon and G. H. Shortley, The Theory of Atomic Spectra, Cambridge, Cambridge University Press, 441 pages, 1959.
[12] A. R. Edmonds, Angular Momenta in Quantum Mechanics, CERN 55-26, Geneva, 82 pages, 1955.
[13] J. A. Gaunt, "The triplets of Helium", *Philosophical Transactions of the Royal Society of London Series A*, 228, 151-196, 1929.
[14] O. R. Cruzan, "Translational addition theorems for spherical vector wave functions", Quarterly Applied Mathematics, 20, 33-40, 1962.
[15] Y. L. Xu, "Fast evaluation of Gaunt coefficients", *Mathematics of Computation*, 65(216), 1601-1612, 1996.
[16] E. J. Weniger and E. O. Steinborn, "Programs for the coupling of spherical harmonics, *Computer Physics Communications*, 25, 149-157, 1982.
[17] J. Rasch and A. C. H. Yu, "Efficient storage scheme for precalculated Wigner 3j, 6j and Gaunt coefficients", *Journal on Scientific Computing*, 25(4), 1416-1428, 2004.
[18] H. H. Homeier and E. O. Steinborn, "Some properties of the coupling coefficients of real spherical harmonics and their relation to Gaunt coefficients", *Journal of Molecular Structure (Theochem)*, 368, 31-37, 1996.
[19] S. A. Yükçü, N. Yükçü and E. Öztekin, "New representations for Gaunt coefficients", *Chemical Physics Letters*, 735 (UNSP 136769), 1-3, 2019.
[20] E. P. Wigner, Group Theory, New York, Academic Press, 372 pages, 1959.
[21] E. L. Akim and A. A. Levin, "Generating Function for Clebsch-Gordan Coefficients", *Doklady Akademii Nauk USSR*, 138, 503-505, 1961.

[22] S. Wolfram, A system for doing mathematics by computer, 2nd ed., United Kingdom, Addison Wesley, 261 pages, 1998.

[23] D. Sebilleau, “On the computation of the integrated products of three spherical harmonics”, *Journal of Physics A: Mathematical and General Physics*, 31(34), 7157-7168, 1998.

Süleyman Demirel Üniversitesi Fen Edebiyat Fakültesi Fen Dergisi https://dergipark.org.tr/sdufeffd
Süleyman Demirel University Faculty of Arts and Sciences Journal of Science e-ISSN: 1306-7575
Research Article, 2023, 18(3): 223-237, DOI: 10.29233/sdufeffd.1237412

Influence of Ho Substitution on Structural, Morphological, and Optical Properties of Anatase $Ti_{1-x}Ho_xO_2$ (x= 0.0, 0.01, 0.02, 0.03) Thin Films

Şeydanur Kaya[1,2,*]

[1] Central Research Laboratory, Kastamonu University, 37100, Kastamonu, TURKEY
[2] Department of Physics, Faculty of Sciences, Kastamonu University, 37100, Kastamonu, TURKEY
https://orcid.org/0000-0002-6894-9082
*corresponding author: *seydanurkaya@kastamonu.edu.tr*

(Received: 17.01.2023, Accepted: 26.09.2023, Published: 23.11.2023)

Abstract: $Ti_{1-x}Ho_xO_2$ (x= 0.0, 0.01, 0.02, 0.03) thin films are synthesized by a sol-gel method and deposited by a dip-coating technique on the glass substrates. The films' crystal structures are examined by an X-ray diffraction technique, while the morphological properties are investigated by scanning electron microscopy and atomic force microscopy. UV-Vis and photoluminescence spectrophotometry are used to analyze the optical properties. Based on the X-ray diffraction patterns, all the films belong to the anatase phase. It is observed that the surface characteristics, such as the morphology, film thickness, and roughness change significantly with the holmium substitution. The optical investigations reveal that the transmittance, band gap energies, and luminescence properties can be adjusted by the holmium substitution. According to the current study, holmium substituted TiO_2 thin films with improved optical properties may be a suitable candidate for applications that require a wide band gap and high optical transparency as well as luminescence properties.

Key words: TiO_2 thin films, Ho substitution, Optical transmittance, Photoluminescence properties

1. Introduction

Titanium dioxide (TiO_2) is one of the most attractive metal oxides with wide band gap (~3.00–4.16 eV) and high optical transmittance [1,2]. TiO_2 is also a promising semiconductor due to its high transparency, refractive index, ultraviolet absorption, and photocatalytic activity, making it suitable for the development of next-generation optoelectronic devices, including photocatalytic systems, optical sensors, photodiodes, phototransistors, solar cells, LEDs, and OLEDs [3]. Furthermore, due to its nontoxicity and biocompatibility, TiO_2 is commonly used in various biotechnological applications such as antibacterial utilities, medicines, air/water purification systems, and cosmetics. Its long-term physical and chemical stability in addition to low-cost and practical synthesis methods are significant advantages for device applications.

Different crystallographic phases, including anatase, rutile, and brookite of TiO_2 can be synthesized by changing the production conditions, such as temperature and pressure. However, rutile and anatase phases are the most commonly used phases in optical applications. Fabrication of TiO_2, in particular, as a thin film rather than as a bulk offers the opportunity for it to be deposited onto different substrates, which enables the production of flexible devices [4]. There are many methods, including chemical spray pyrolysis, electron-beam evaporation, RF sputtering, chemical vapor deposition, and pulsed laser deposition to produce anatase TiO_2 thin films [5–9]. Due to these methods' complex, expensive, and time-consuming manufacturing processes, researchers have focused on wet chemical methods, such as hydrothermal, chemical bath, and sol-gel, which give desired results in thin film deposition. Among them, the sol-gel method is one of the most attractive methods due to its simple, inexpensive, fast, and practical production processes. This method makes it possible to produce pure and homogeneous thin films with a controllable stoichiometry at relatively lower temperatures. In addition, it enables the fabrication of thin films with different morphologies and optical properties by changing the solution chemistry and the deposition parameters. The sol-gel method with deposition techniques, such as dip-coating and spin-coating provides high-quality thin films with stable optical properties [10]. Thin film surface properties, including grain distribution, size and orientation, film thickness, and roughness play crucial roles in the optical properties of TiO_2. Many previous studies have revealed the strong relationships between the morphological properties and optical properties of TiO_2 thin films [11,12].

Various strategies have been developed to modify the current properties of TiO_2 thin films, such as doping with metal or nonmetal ions, forming oxygen vacancies in the crystal lattice, deposition of various noble metals, combinations with other semiconductors, and interfacial modifications [13]. Undoubtedly, the most practical and effective method among these is doping to the semiconductor's crystal structure. A typical doping process is based on the controlled incorporation of foreign atoms into the crystal lattice. Doping even a small amount of foreign atoms can change the band gap of the semiconductor, increase the amount of charge carriers, and significantly improve the emission properties. In regard to doping studies carried out so far, different factors exist that can affect the final sample, such as production methods and parameters, types of precursor materials and ratios, and solvents. Therefore, each doping processing method should be evaluated within itself in terms of its conditions [14,15]. Namely, even if the same element is doped, different results can be obtained. The doping of rare earth elements (REs) is one of the most effective techniques for the structural and morphological manipulation of TiO_2 as a semiconductor [16]. RE^{3+} ions provide superior electronic, optical, and chemical properties in a wide range of applications due to their 4f electron configuration. Among RE^{3+} ions, holmium (Ho) is one of the most attractive metals due to its large atomic radius and luminescence properties originating from the f-f electronic transition within the partially filled 4f orbitals. By optimizing the doping process of Ho^{3+} ions, it is possible to tune the band gap and optical characteristics of TiO_2 by introducing impurity energy levels into the electronic structure [17]. In addition, the combination of titanium and holmium atoms creates several oxide forms, providing a high magnetic moment, susceptibility, and dielectric permittivity [18]. Compared to other REs, however, fewer studies were conducted on Ho doping on TiO_2. The existing reports mainly focus on its photocatalytic, photovoltaic, magnetic, optoelectronic, and piezoelectric properties [19–23]. However, in these reports, powder or bulk forms of titania, rutile or oxide-mixed crystal phases have been investigated. To our knowledge, no detailed report has been published on the structural and optical properties of Ho doped anatase TiO_2 thin films produced by the sol-gel based dip coating technique. Thus, in this study, the effect of holmium (Ho) on the morphological and optical properties of anatase TiO_2 was investigated. $Ti_{1-x}Ho_xO_2$ (x= 0.0, 0.01, 0.02, 0.03) thin films were produced via a sol-gel method. The influence of Ho substitution on the structural, morphological, and optical properties was examined by various techniques and significant changes were reported.

2. Materials and Methods

A sol-gel method was used to prepare the aqueous solution and a dip-coating technique was used for the deposition of the thin films. A schematic diagram of the preparation of the samples is given in Figure 1. All the films were deposited on a glass substrate using a 0.5 M aqueous solution containing titanium (IV) butoxide ($Ti(OCH_2CH_2CH_2CH_3)_4$) and holmium(III) nitrate pentahydrate ($Ho(NO_3)_3 \cdot 5H_2O$) as precursor materials. A substitutional doping process was carried out. Ethanol was used as a solvent and acetylacetone was used as a chelating agent. A mixture of hydrochloric acid and distilled water was added to the solution dropwise for hydrolysis. The final solution was stirred for two hours at room temperature. After aging overnight, ultrasonically cleaned glass substrates were dip-coated five times. Finally, an annealing process at 600 °C for one hour was applied to all the samples to obtain an anatase crystal phase. An X-ray diffractometer (PANalytical, Empyrean) was used to analyze the crystal structure, while a scanning electron microscope (FEI, Quanta FEG 250) and an atomic force microscope (Bruker, EDGE 3-SYS) were used to examine the surface morphology of the films. A UV-Vis spectrophotometer (Shimadzu, UV Pharmaspec 1700) was used to investigate the optical transmittance, whereas a photoluminescence spectrophotometer (Horiba, FluoroMax-4) equipped with a Xenon lamp was used to analyze the luminescence properties of the samples. The excitation wavelength used was 365 nm.

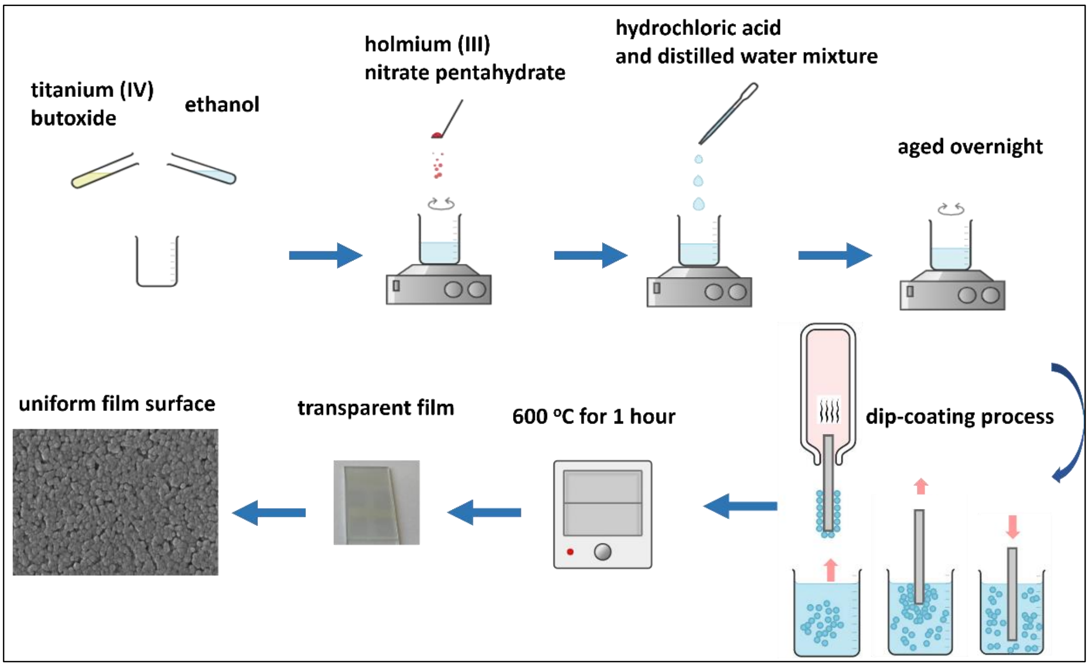

Figure 1. Schematic diagram of the preparation of $Ti_{1-x}Ho_xO_2$ (x= 0.0, 0.01, 0.02, 0.03) thin films

3. Results

The X-ray diffraction patterns of the samples are given in Figure 2. All samples belong to the tetragonal anatase phase of TiO_2 with the diffraction peaks of (101) and (200). There is preferential growth along the (101) surface due to its lowest surface energy [24]. While no impurity peaks are observed in the undoped TiO_2, the impurity peaks of the diholmium titanate (Ho_2TiO_5) phase are detected with increasing Ho concentration. Thus, it can be said that some of the dopant ions do not enter the crystal lattice but instead form the Ho_2TiO_5 based secondary crystal phases, which reach a considerably high intensity level in $Ti_{0.97}Ho_{0.03}O_2$. Furthermore, a slight increase is observed in the intensity of both the (101) and (200) peaks with increasing Ho concentration.

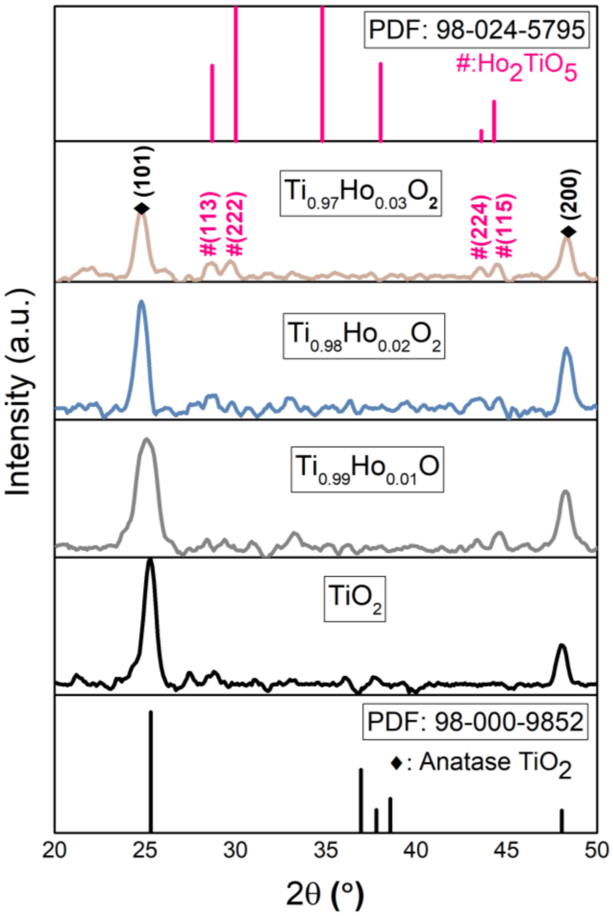

Figure 2. X-ray diffraction patterns of $Ti_{1-x}Ho_xO_2$ (x= 0.0, 0.01, 0.02, 0.03)

The lattice parameters, crystallite size, lattice strain, and dislocation density values of the samples are summarized in Table 1. The lattice parameters for a tetragonal crystal system are calculated by the Bragg's law, which is given below [25]:

$$\frac{1}{d^2} = \frac{h^2 + k^2}{a^2} + \frac{l^2}{c^2} \tag{1}$$

where, d is the interplanar spacing between the crystal planes, h, k, l are the Miller indices, a and c $(a = b \neq c)$ are the lattice parameters of the tetragonal crystal system. The crystallite size values of the samples are determined using the Scherrer equation, which is given as [25]:

$$D = 0.941\lambda/\beta cos\theta \tag{2}$$

where D is the crystallite size, λ is the wavelength of the X-ray, β is the full width at half maximum (FWHM), and θ is the diffraction angle. The microstrain values are calculated using the formula given below [26]:

$$\varepsilon = \frac{\beta cos\theta}{4sin\theta} \tag{3}$$

Finally, for the density dislocation calculations, the Williamson–Hall relation is used as given below [27]:

$$\delta = \frac{1}{D^2} \tag{4}$$

where β is the (FWHM), θ is the diffraction angle, and D is the crystallite size.

Table 1. Lattice parameters, crystallite size, lattice strain, dislocation density, and film thickness values of $Ti_{1-x}Ho_xO_2$ (x= 0.0, 0.01, 0.02, 0.03)

Sample	Lattice parameters a (Å)= b (Å)	c (Å)	Crystallite size (nm)	Microstrain (10^{-3})	Discolation Density (10^{-3}) (nm^{-2})	Film thickness (nm)
TiO_2	3.78	9.49	13	12.63	5.91	60.93
$Ti_{0.99}Ho_{0.01}O_2$	3.93	9.21	9	19.01	12.3	68.14
$Ti_{0.98}Ho_{0.02}O_2$	3.80	9.65	11	14.25	8.26	75.02
$Ti_{0.97}Ho_{0.03}O_2$	3.66	9.29	12	13.69	6.94	82.34

According to Table 1, the a lattice parameter of undoped TiO_2 is 3.78 Å, while it increases to 3.93 Å for $Ti_{0.99}Ho_{0.01}O_2$. Then, a gradual decrease is observed in the a lattice parameter values with increasing Ho substitution ratio and reaches its minimum in $Ti_{0.97}Ho_{0.03}O_2$. The Ho^{3+} ions have a larger ionic radius (0.901 Å) than that of the Ti^{4+} ions (0.605 Å). Thus, the incorporation of Ho^{3+} ions into the Ti^{4+} sites is expected to create lattice expansion and tensile microstrain in the TiO_2 [28]. At 1% Ho, the increment of the a lattice parameter indicates that the Ho^{3+} ions cause an expansion along the a-direction of the TiO_2 tetragonal lattice. This result is in agreement with the highest tensile microstrain value of $Ti_{0.99}Ho_{0.01}O_2$ given in Table 1. It is also interesting to note that the Ho_2TiO_5 phase begins to form in this sample, which is shown by weak XRD peaks yet do not affect the substitution process, according to the crystal parameters (Table 1). As the Ho concentration increases, the substitution ratio decreases, and unsubstituted Ho^{3+} ions promote further formation of the Ho_2TiO_5 phase. Accordingly, the expansion along the a-direction tends to decrease at relatively higher Ho concentrations. Previously, the increment up to a certain doping level and then decrement of the a lattice parameter has been observed in ZnO thin films and has been associated with the difference in dopant ionic radii, which is also supported by our current results [29]. The c lattice parameter is 9.49 Å for the undoped sample and decreases to 9.21 Å for $Ti_{0.99}Ho_{0.01}O_2$. While a slight increase is observed in $Ti_{0.98}Ho_{0.02}O_2$, it decreases in $Ti_{0.97}Ho_{0.03}O_2$. These variations in lattice parameters can be attributed to the different incorporation rates of Ho^{3+} ions into the TiO_2 host crystal lattice as well as the formation of the Ho_2TiO_5 phase. The crystallite size values are 13 nm, 9 nm, 11 nm, and 12 nm for TiO_2, $Ti_{0.99}Ho_{0.01}O_2$, $Ti_{0.98}Ho_{0.02}O_2$, and $Ti_{0.97}Ho_{0.03}O_2$, respectively. Positive microstrain values are observed for all the samples, confirming the tensile strain of the lattice (Table 1). The undoped sample has the lowest microstrain value. At 1% Ho, a significant increase occurs in the microstrain of $Ti_{0.99}Ho_{0.01}O_2$, and then, with increasing Ho concentration, shows a gradual decrease to a value still higher than the undoped one. This observation aligns with a similar result reported previously, which confirms that Ho ions result in a distortion in the TiO_2 crystal lattice [19]. This enhancement in the microstrain might be caused by several factors, such as crystal defects, lattice mismatch, and the difference between the ionic radius of the dopants and the host ions [30,31]. Dislocations can be defined as imperfections in a crystal, while dislocation density describes the dislocation lines per unit volume of the crystals [32]. According to the dislocation density values given in Table 1, the incorporation of Ho^{3+} ions into the TiO_2 lattice creates lattice distortions, which is attributed to the defect concentration.

Figure 3 shows the top and cross-sectional SEM images of the $Ti_{1-x}Ho_xO_2$ (x= 0.0, 0.01, 0.02, 0.03) thin films. As shown in Figure 3(a), undoped TiO_2 has a homogenous surface distribution of uniformly sized spherical particles. With the incorporation of Ho^{3+} ions into the crystal structure, at a concentration of 1%, the surface morphology significantly changes. Many more grain formations with different shapes including both smaller and larger particles are observed, compared with that of the undoped sample (Figure 3(b)). When the Ho concentration is 2%, the number of large particles decreases (Figure 3(c)). At 3% Ho, quite large polyhedral clusters with sharp edges are observed on the surface

(Figure 3(d)). Thus, it can be said that the surface is quite far from a uniform distribution at 3% Ho.

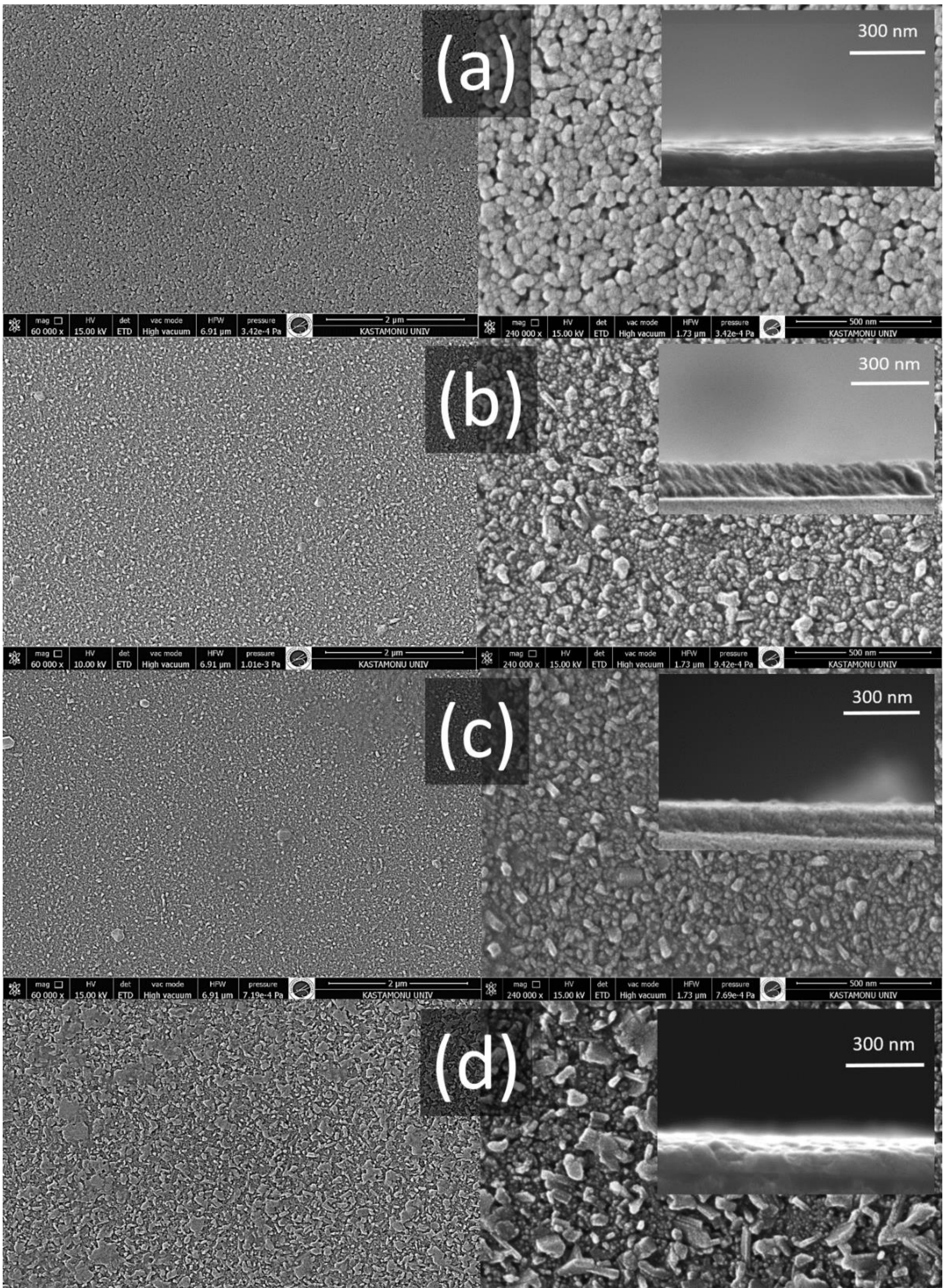

Figure 3. Top and cross-sectional (shown in inset) SEM views of (a) TiO_2, (b) $Ti_{0.99}Ho_{0.01}O_2$, (c) $Ti_{0.98}Ho_{0.02}O_2$, and (d) $Ti_{0.97}Ho_{0.03}O_2$

The film thicknesses were measured from the cross-sectional SEM views of the films and are given in Table 1. The film thicknesses are 60.93 nm, 68.14 nm, 75.02 nm, and 82.34 nm for TiO_2, $Ti_{0.99}Ho_{0.01}O_2$, $Ti_{0.98}Ho_{0.02}O_2$, and $Ti_{0.97}Ho_{0.03}O_2$, respectively. It can be concluded that the thickness of the films increases gradually with Ho substitution. EDX area analysis spectra of the samples are given in Figure 4, while the mapping results of $Ti_{0.97}Ho_{0.03}O_2$ is given in Figure 5. The elemental concentrations of all the samples are given in Table 2. In addition to Ti, O, and Ho peaks, the spectra include some impurity peaks such as Si and Na, which come from the substrate used, as well as, Au peaks, which come from the conductive coating of SEM measurements. For the undoped sample, the elemental concentrations of Ti and O are 33.32 and 66.68 (atomic %), respectively. For $Ti_{0.97}Ho_{0.03}O_2$, the elemental concentrations of Ti, O, and Ho are 29.28, 65.87, and 4.85 (atomic %), respectively. The mapping images confirm the homogeneous distribution of the Ho^{3+} ions in the TiO_2 microstructure.

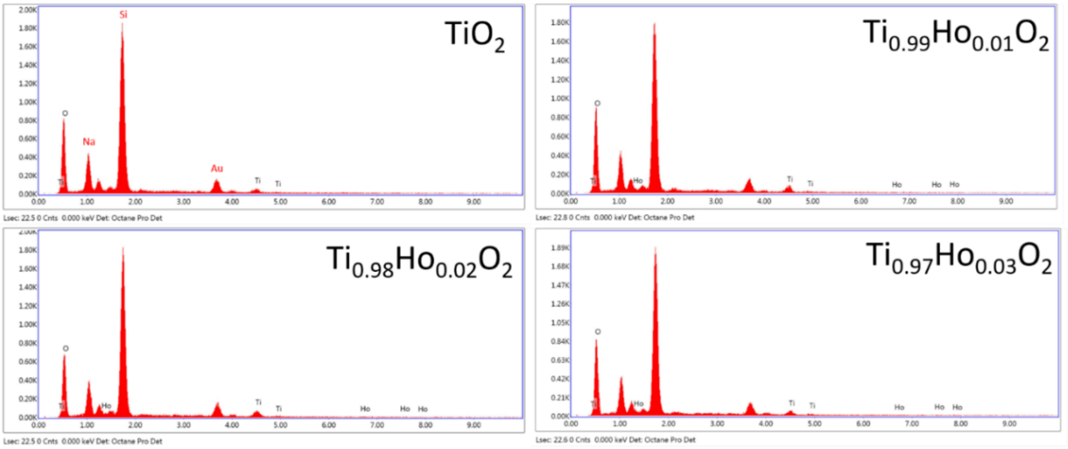

Figure 4. EDX analysis spectra of $Ti_{1-x}Ho_xO_2$ (x= 0.0, 0.01, 0.02, 0.03)

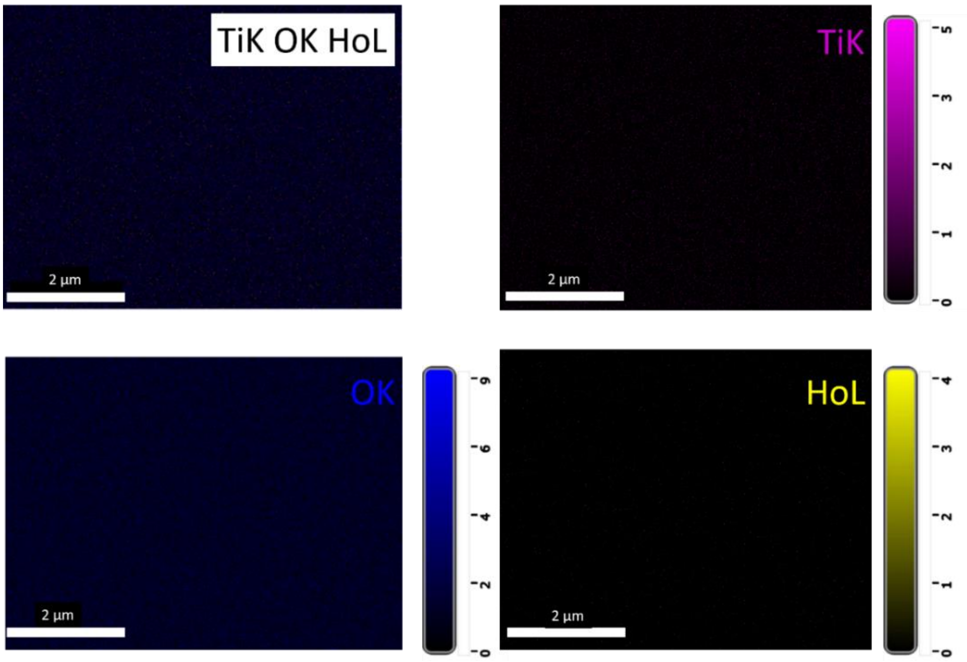

Figure 5. EDX mapping images of $Ti_{0.97}Ho_{0.03}O_2$

Table 2. Elemental concentrations of $Ti_{1-x}Ho_xO_2$ (x= 0.0, 0.01, 0.02, 0.03)

Sample	Element	Atomic (%)
TiO_2	Ti	33.32
	O	66.68
$Ti_{0.99}Ho_{0.01}O_2$	Ti	31.94
	O	65.33
	Ho	2.73
$Ti_{0.98}Ho_{0.02}O_2$	Ti	30.60
	O	66.13
	Ho	3.27
$Ti_{0.97}Ho_{0.03}O_2$	Ti	29.28
	O	65.87
	Ho	4.85

Figure 6 shows the top and perspective AFM views of the $Ti_{1-x}Ho_xO_2$ (x= 0.0, 0.01, 0.02, 0.03) thin films. In all the images, an area of 5x5 µm was scanned. The top views of the film surfaces are shown on the left, while perspective views are shown on the right. According to the images, whereas there is a homogeneous particle distribution in the undoped TiO_2, the clusters forming on the surfaces can clearly be seen in the doped samples, in accordance with the SEM results.

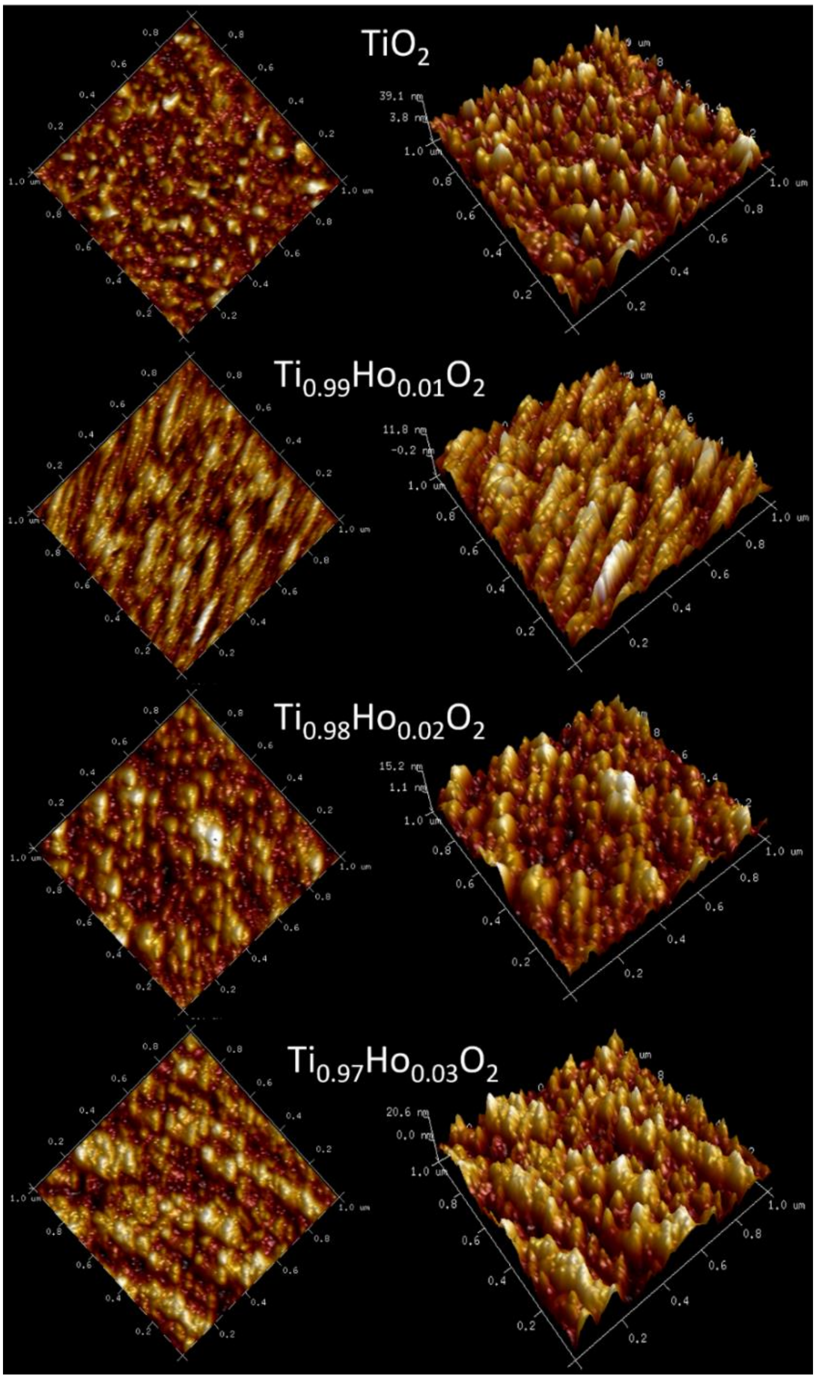

Figure 6. Top (left) and perspective (right) AFM views of $Ti_{1-x}Ho_xO_2$ (x= 0.00, 0.01, 0.02, 0.03)

For a further investigation of the films' surface profile, roughness analyzes were carried out. The roughness parameters of all the samples, including average roughness (R_a), root mean square roughness (R_q), maximum roughness (R_{max}), skewness (R_{sk}), and kurtosis (R_{ku}) are presented in Table 3. The (R_a) is 3.20 nm for undoped TiO_2, which increases to 3.61 nm in $Ti_{0.99}Ho_{0.01}O_2$. When the Ho concentration reaches 2%, the R_a value is obtained as 4.54 nm. Finally, at a concentration of 3% Ho, it reaches its maximum, with a value of 5.02 nm. The formation of larger particles due to Ho substitution could be responsible for this slight increase in the roughness values due to the variation in height differences on the film surfaces. The R_q value is a measure of the standard deviation of the Z height and is also known as RMS. This parameter defines the roughness by statistical methods, unlike the arithmetic average height (R_a) and gives more precise results than R_a in terms of significant deviation from the reference line [33]. Although R_a is used more frequently in surface roughness definitions, R_q values should also be considered when examining roughness properties. R_q values are obtained as 4.16 nm, 4.58 nm, 6.00 nm, and 6.27 nm for TiO_2, $Ti_{0.99}Ho_{0.01}O_2$, $Ti_{0.98}Ho_{0.02}O_2$, and $Ti_{0.97}Ho_{0.03}O_2$, respectively, showing a gradual increment with Ho substitution. As expected, the R_q values are higher than those of R_a and have the same increasing tendency with Ho concentration rate. Morphological changes previously observed in SEM, such as increasing film thickness, change in grain sizes, formation of clusters on the surface, and formation of secondary oxide phases with Ho substitution, can be attributed to the increase in both R_q and R_a values. The R_{sk} values, which show the degree of asymmetry of the profile about the reference line, are obtained as 0.97, 0.44, 0.88, and 0.24 for TiO_2, $Ti_{0.99}Ho_{0.01}O_2$, $Ti_{0.98}Ho_{0.02}O_2$, and $Ti_{0.97}Ho_{0.03}O_2$, respectively. These positive skewness values mean the peaks are predominantly distributed on all the film surfaces. The R_{ku} values of the samples are obtained as 4.91, 3.67, 4.78, and 3.13 for TiO_2, $Ti_{0.99}Ho_{0.01}O_2$, $Ti_{0.98}Ho_{0.02}O_2$, and $Ti_{0.97}Ho_{0.03}O_2$, respectively. R_{ku} values higher than 3 mean the film surfaces is defined as leptokurtic [33].

Table 3. Roughness parameters of $Ti_{1-x}Ho_xO_2$ (x= 0.00, 0.01, 0.02, 0.03)

Parameters	$\boldsymbol{R_a\ (nm)}$	$\boldsymbol{R_q\ (nm)}$	$\boldsymbol{R_{max}(nm)}$	$\boldsymbol{R_{sk}}$	$\boldsymbol{R_{ku}}$
Samples					
TiO_2	3.20	4.16	41.9	0.97	4.91
$Ti_{0.99}Ho_{0.01}O_2$	3.61	5.58	42.6	0.44	3.67
$Ti_{0.98}Ho_{0.02}O_2$	4.54	6.00	51.4	0.88	4.78
$Ti_{0.97}Ho_{0.03}O_2$	5.02	6.27	48.2	0.24	3.13

Figure 7 illustrates the optical transmittance graphs, while Table 4 presents the corresponding average transmittance values of $Ti_{1-x}Ho_xO_2$ (x= 0.0, 0.01, 0.02, 0.03) thin films. The average optical transmittance of the undoped sample in the visible region is 62%. With the Ho substitution, the average optical transmittance is obtained as 65% in $Ti_{0.99}Ho_{0.01}O_2$, while it is 77% in $Ti_{0.98}Ho_{0.02}O_2$, showing a considerable increment. Finally, $Ti_{0.97}Ho_{0.03}O_2$ shows the highest optical transmittance value of 80%. It is clear that Ho substitution improves the optical transmittance of TiO_2 thin films produced by the current method. The increment in the optical transmittance values of TiO_2 thin films by various doping processes has been observed in previous studies [11,16,34]. Many factors, such as film thickness, surface properties, roughness, crystal defects, annealing temperature and conditions, affect film transparency [35,36]. For the current study, the reduction in crystallite size with Ho substitution might hinder the light scattering, causing an increased optical transmittance in the visible region [35,37]. Furthermore, previous studies have emphasized that the transmittance properties are associated with crystal lattice defects [6,36,38]. In particular, the boost observed in the optical transmittance of $Ti_{0.98}Ho_{0.02}O_2$ might be attributed to the sharp decrease in the dislocation density of this sample (Table 1). Moreover, the formation of Ho_2TiO_5 particles might be responsible for the increased light transmission, which also needs further research.

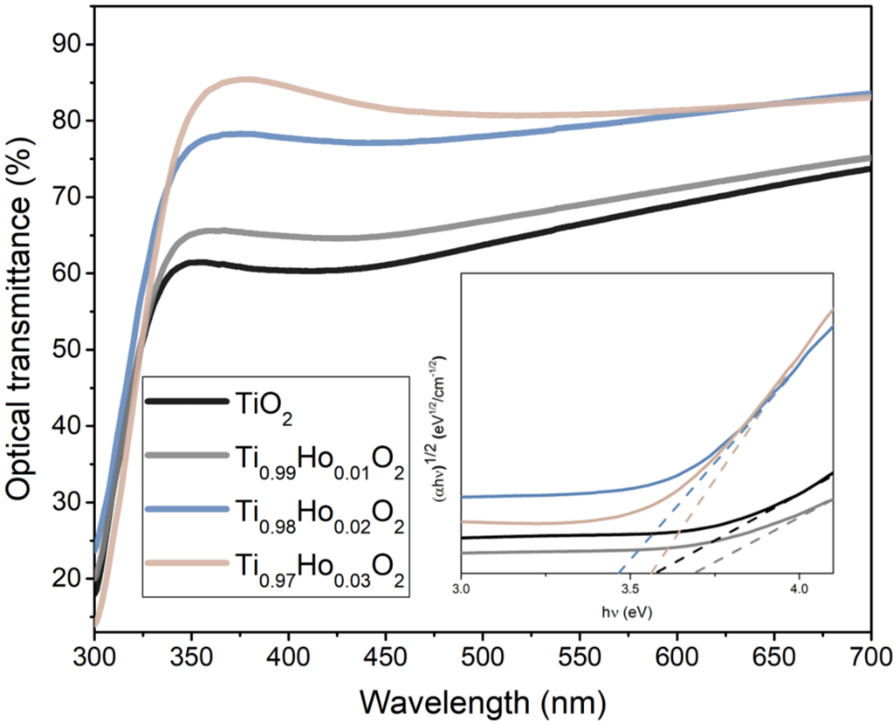

Figure 7. Optical transmittance graphs and Tauc's plots (shown in the inset) of $Ti_{1-x}Ho_xO_2$ (x= 0.0, 0.01, 0.02, 0.03)

Table 4. Average optical transmittance, band gap energy, and refractive index values of $Ti_{1-x}Ho_xO_2$ (x= 0.00, 0.01, 0.02, 0.03)

Sample	Average optical transmittance (%)	Band gap energy (eV)	Refractive index
TiO_2	62	3.58	2.17
$Ti_{0.99}Ho_{0.01}O_2$	65	3.69	2.14
$Ti_{0.98}Ho_{0.02}O_2$	77	3.46	2.20
$Ti_{0.97}Ho_{0.03}O_2$	80	3.56	2.17

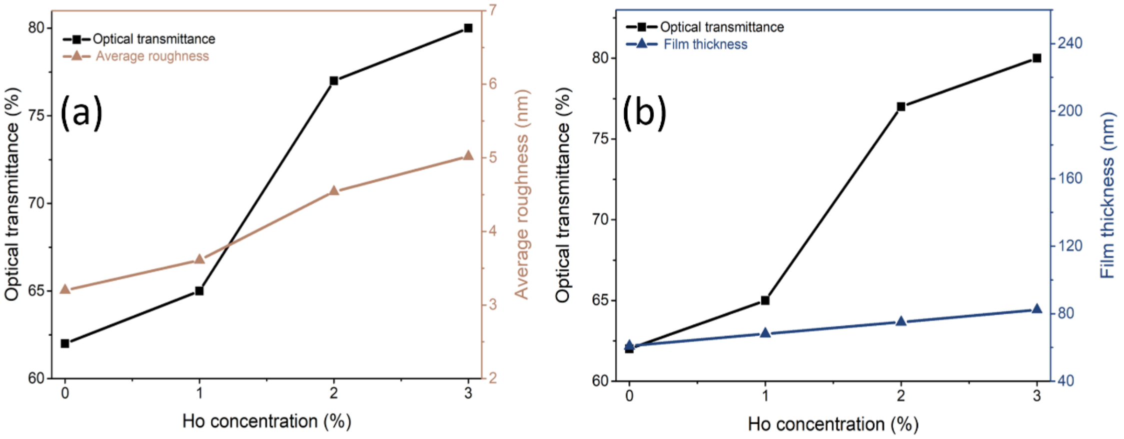

Figure 8. (a) The relationship between the average roughness and the average optical transmittance versus different Ho concentrations, (b) The relationship between the optical transmittance and the film thickness of the films versus different Ho concentrations

Figure 8(a) shows the relationship between the average roughness and the average optical transmittance values of all the samples. According to the graph, films' optical transmittance and roughness values increases with Ho substitution. Accordingly, it can be concluded that roughness-induced light scattering do not suppress an increase in the optical transmittance of the films with Ho substitution [34]. Figure 8(b) shows the relationship between the optical transmittance values and the film thickness of the samples versus different Ho concentrations. It is clear from the graph that the optical transmittance of the samples increases with the Ho concentration despite an increase in film thickness.

From the transmittance spectrum, the absorption coefficient (α) can be calculated by the equation given below [39]:

$$\alpha = \frac{1}{d}(ln\frac{1}{T}) \tag{5}$$

where T is the transmittance, and d is the thickness of the film. The band gap energy is determined using the equation given as [40]:

$$\alpha = \frac{A(hv - E_g)^n}{hv} \tag{6}$$

where hv is the photon energy, and A is the photon energy independent constant. The exponent n has a value of 1/2 for direct transitions and a value of 2 for indirect transitions. For indirect transitions, the equation can be written as [12]:

$$(\alpha hv)^{1/2} = A\left(hv - E_g\right) \tag{7}$$

The indirect band gap energies (E_g) of the samples were calculated from Tauc's plots, which are given in the inset of Figure 7, showing extrapolation of the linear portion of the plot $(\alpha hv)^{1/2}$ as a function of hv. The E_g values of all the samples are given in Table 4. The values obtained are in agreement with previous reports [6,37]. The E_g values of the samples are calculated as 3.58 eV, 3.69 eV, 3.46 eV, and 3.56 eV for TiO_2, $Ti_{0.99}Ho_{0.01}O_2$, $Ti_{0.98}Ho_{0.02}O_2$, and $Ti_{0.97}Ho_{0.03}O_2$, respectively. The band gap values of TiO_2 thin films are highly dependent on the production methods, electronic structure, chemical compositions and ratios, heat treatment procedures, surface morphology, and crystal properties. A widening in the E_g of $Ti_{0.99}Ho_{0.01}O_2$ can be attributed to the sharp decrease in the crystallite size of this sample (Table 1). On the other hand, a narrowing of E_g in $Ti_{0.98}Ho_{0.02}O_2$ is attributed to the introduction of new impurity levels through substitution [34]. As the Ho concentration increases, factors such as the increase in the crystallite size and the creation of lattice defects might be responsible for the further increase in the E_g of $Ti_{0.97}Ho_{0.03}O_2$ [6].

The refractive indices of the samples were estimated by a general relation between the refractive index and energy gap in semiconductors proposed by Hervé and Vandamme [41]:

$$n^2 = 1 + (\frac{A}{E_g + B})^2 \tag{8}$$

where, A is the hydrogen ionization energy, which equals 13.6 eV, while B is the constant assumed to be the difference between the UV resonance energy and band gap energy, and equals 3.47 eV [29,42]. Refractive index (n) values are given in Table 4. The n value is obtained as 2.17 for the undoped sample, while it is 2.14 for $Ti_{0.99}Ho_{0.01}O_2$. After showing the maximum value of 2.20 for $Ti_{0.98}Ho_{0.02}O_2$, interestingly, it decreases again to 2.17 in $Ti_{0.97}Ho_{0.03}O_2$. In previous studies, an increment [16,43], a decrement [44], and fluctuations [45] of the refractive index of TiO_2 with doping have been observed. The change in the refractive index has been associated with different factors such as crystal phase, crystallite size, annealing temperature, packing density, porosity, and film density

[46]. In addition, condensation and evaporation processes during the preparation of sol-gel based materials as well as the heat treatment and withdrawal speed of the substrate during the dip coating processes may also be responsible for the changes in the reactive index by affecting the surface characteristics [47].

The photoluminescence (PL) emission spectra of $Ti_{1-x}Ho_xO_2$ (x= 0.0, 0.01, 0.02, 0.03) thin films are given in Figure 9. All the samples exhibit a broad visible emission band ranging from 460 to 600 nm. The undoped sample's emission band is centered at 526 nm, while a slight blueshift is observed at 1% and 2% Ho. The peak center of the emission band is measured as 524 and 523 nm for $Ti_{0.99}Ho_{0.01}O_2$ and $Ti_{0.98}Ho_{0.02}O_2$, respectively. At 3% Ho, the peak center is 524 nm for $Ti_{0.97}Ho_{0.03}O_2$. The emission intensity of the samples increases as the Ho concentration is raised to 2%. The maximum emission is observed in $Ti_{0.98}Ho_{0.02}O_2$, and then it shows a sharp reduction in $Ti_{0.97}Ho_{0.03}O_2$. In the case of doped TiO_2 thin films, it has been previously observed that PL emissions are quenched or even disappear at higher doping ratios [48,49]. The variation in PL intensity is attributed to the change in defect states on the shallow level of the thin film surfaces [50]. Thus, it can be inferred that the recombination rate of photogenerated electrons and holes on the shallow level of the film sharply decreases in $Ti_{0.97}Ho_{0.03}O_2$ [50,51]. In addition to these results, it is noteworthy that the intense formation of the Ho_2TiO_5 as a secondary phase could be also responsible for the PL quenching in $Ti_{0.97}Ho_{0.03}O_2$.

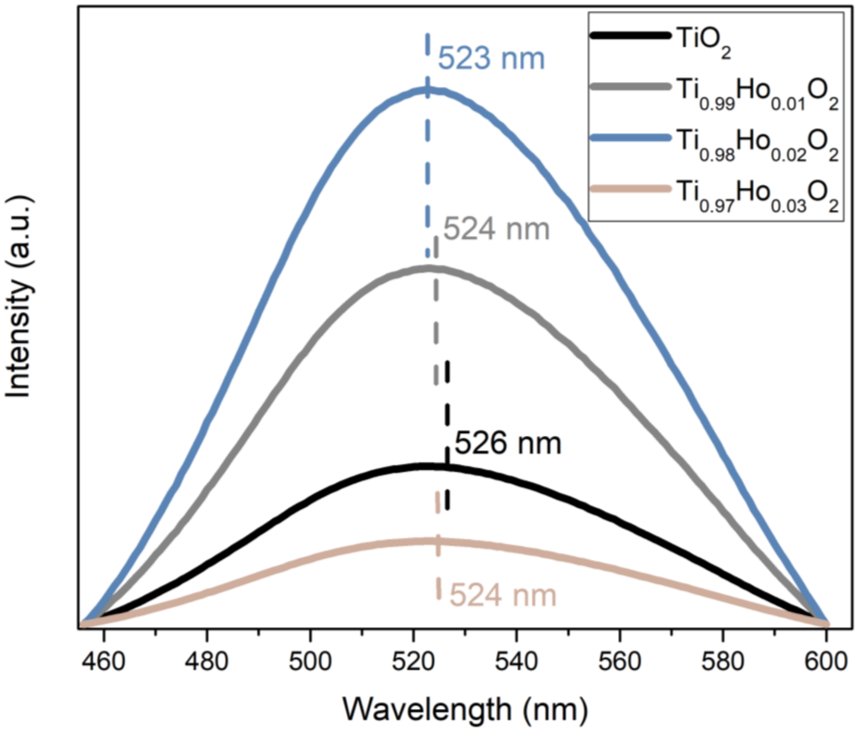

Figure 9. PL emissions of $Ti_{1-x}Ho_xO_2$ (x= 0.0, 0.01, 0.02, 0.03)

4. Conclusion

$Ti_{1-x}Ho_xO_2$ (x= 0.0, 0.01, 0.02, 0.03) thin films were prepared by a sol-gel method and a dip-coating technique. The influence of Ho substitution on the crystallographic, morphologic, and optical properties of TiO_2 thin films was investigated. According to the X-ray diffraction analyzes, all the films belong to the anatase phase of TiO_2. Nevertheless, with increasing Ho concentration, a secondary phase of Ho_2TiO_5 is observed. SEM images show that Ho substitution has significant effects on the morphological properties of TiO_2 thin films. The AFM measurements reveal that the Ho substitution increases the average roughness of the TiO_2 thin films. The increase in both the thickness and roughness values of the films with the increase in Ho concentration does not hinder the enhancement of the optical transmittance of the samples. Furthermore, the visible region PL emission increases as the Ho concentration is increased up to 2%, and then decreases sharply at 3% Ho, indicating that a quenching occurs in substituted samples beyond a certain level (2% for the current study). Overall, it can be concluded that Ho substitution at relatively lower rates ($x < 3\%$) is an efficient way to improve the optical properties of TiO_2 thin films, which are good candidates for next-generation optoelectronic applications.

Authorship contribution statement

Ş. Kaya: Conceptualization, Methodology, Investigation, Original Draft Writing, Review and Editing.

Declaration of competing interest

The authors declare that they have no known competing financial interests or personal relationships that could have appeared to influence the work reported in this paper.

Acknowledgment

This study was funded by the Kastamonu University Scientific Research Projects Coordination Department under Grant No. [KU-BAP01/2021-05].

Ethics Committee Approval and/or Informed Consent Information

As the authors of this study, we declare that we do not have any ethics committee approval and/or informed consent statement.

References

[1] A. M. E. Raj, V. Agnes, V. Bena Jothy, C. Ravidhas, J. Wollschläger, M. Suendorf, M. Neumann, M. Jayachandran and C. Sanjeeviraja, "Spray deposition and property analysis of anatase phase titania (TiO 2) nanostructures", *Thin Solid Films*, 519, 129-135,2010.

[2] T. C. Paul, M. H. Babu, J. Podder, B. C. Dev, S. K. Sen and S. Islam, "Influence of Fe3+ ions doping on TiO2 thin films: Defect generation, d-d transition and band gap tuning for optoelectronic device applications", *Physica B: Condensed Matter*, 604, 412618,2021.

[3] T. S. Rajaraman, S. P. Parikh and V. G. Gandhi, "Black TiO2: A review of its properties and conflicting trends", *Chemical Engineering Journal*, 389, 123918,2020.

[4] A. Farzaneh, M. Javidani, M.D. Esrafili and O. Mermer, "Optical and photocatalytic characteristics of Al and Cu doped TiO2: Experimental assessments and DFT calculations", *Journal of Physics and Chemistry of Solids*, 161, 110404, 2022.

[5] A. Möllmann, D. Gedamu, P. Vivo, R. Frohnhoven, D. Stadler, T. Fischer, I. Ka, M. Steinhorst, R. Nechache, F. Rosei, S.G. Cloutier, T. Kirchartz and S. Mathur, "Highly Compact TiO 2 Films by Spray Pyrolysis and Application in Perovskite Solar Cells", *Advance Engineering Materials*, 4,1801196, 2019.

[6] C. Yang, H. Fan, Y. Xi, J. Chen and Z. Li, "Effects of depositing temperatures on structure and optical properties of TiO 2 film deposited by ion beam assisted electron beam evaporation", *Applied Surface Science*, 44 (15), 2996-3000, 2008.

[7] D. Mardare, M. Tasca, M. Delibas and G. I. Rusu, "On the structural properties and optical transmittance of TiO2 r.f. sputtered thin films", *Applied Surface Science*, 156 (1-4), 200-206, 2000.

[8] D.S. Bhachu, R.G. Egdell, G. Sankar, C.J. Carmalt and I.P. Parkin, "Electronic properties of antimony-doped anatase TiO2 thin films prepared by aerosol assisted chemical vapour deposition", *Journal of Materials Chemistry C*, 5 (37), 9694-9701, 2017.

[9] J .C. Orlianges, A. Crunteanu, A. Pothier, T. Merle-Mejean, P. Blondy and C. Champeaux, "Titanium dioxide thin films deposited by pulsed laser deposition and integration in radio frequency devices: Study of structure, optical and dielectric properties", *Applied Surface Science*, 263, 111-114,2012.

[10] S. Obregón and V. Rodríguez-González, "Photocatalytic TiO2 thin films and coatings prepared by

sol–gel processing: a brief review", *Journal of Sol-Gel Science and Technology*, 102,125-141, 2021.

[11] Z. Lu, X. Jiang, B. Zhou, X. Wu and L. Lu, "Study of effect annealing temperature on the structure, morphology and photocatalytic activity of Si doped TiO 2 thin films deposited by electron beam evaporation", *Applied Surface Science*, 257 (24), 10715-10720, 2011.

[12] S. K. Gupta, J. Singh, K. Anbalagan, P. Kothari, R. R. Bhatia, P. K. Mishra, V. Manjuladevi, R. K. Gupta and J. Akhtar, "Synthesis, phase to phase deposition and characterization of rutile nanocrystalline titanium dioxide (TiO 2) thin films", *Applied Surface Science*, 264, 737-742, 2013.

[13] Y. Lv, H. Tong, W. Cai, Z. Zhang, H. Chen, X. Zhou, "Boosting the efficiency of commercial available carbon-based perovskite solar cells using Zinc-doped TiO2 nanorod arrays as electron transport layer", *Journal of Alloys and Compounds*, 851, 156785, 2021.

[14] H. N. T. Phung, N. D. Truong, L. T. Nguyen, K. L. P. Thi, P. A. Duong and V.T.H. Le, "Enhancement of the visible light photocatalytic activity of vanadium and nitrogen co-doped TiO2 thin film", *Journal of Nonlinear Optical Physics & Materials*, 24 (4), 1550052, 2015.

[15] M. H. Chan, W. Y. Ho, D. Y. Wang and F. H. Lu, "Characterization of Cr-doped TiO2 thin films prepared by cathodic arc plasma deposition", *Surface Coatings Technology*, 202 (4-7), 962–966, 2007.

[16] D. Komaraiah, E. Radha, J. Sivakumar, M. V. Ramana Reddy and R. Sayanna, "Photoluminescence and photocatalytic activity of spin coated Ag+ doped anatase TiO2 thin films", *Optical Materials*, 108, 110401, 2020.

[17] B. Singaram, J. Jeyaram, R. Rajendran, P. Arumugam and K. Varadharajan, "Visible light photocatalytic activity of tungsten and fluorine codoped TiO2 nanoparticle for an efficient dye degradation", *Ionics*, 25 (2), 773–784, 2019.

[18] K. Kukli, M. Kemell, M. C. Dimri, E. Puukilainen, A. Tamm, R. Stern, M. Ritala and M. Leskelä, "Holmium titanium oxide thin films grown by atomic layer deposition", *Thin Solid Films*, 565, 261–266, 2014.

[19] J. wen Shi, J. tang Zheng and P. Wu, "Preparation, characterization and photocatalytic activities of holmium-doped titanium dioxide nanoparticles", *Journal of Hazardous Materials*, 161(1), 416–422, 2009.

[20] J. Shi, J. Zheng, Y. Hu and Y. Zhao, "Photocatalytic degradation of organic compounds in aqueous systems by Fe and Ho codoped TiO2", *Kinetics and Catalysis*, 49, 279–284, 2008.

[21] F. Peng and D. Zhu, "Effect of sintering temperature and Ho2O3 on the properties of TiO2-based varistors", *Ceramics International*, 44, 21034–21039, 2018.

[22] T. M. Pan, M. De Huang, C. W. Lin and M. H. Wu, "Development of high-κ HoTiO3 sensing membrane for pH detection and glucose biosensing", *Sensors & Actuators, B: Chemical*, 144, 139–145, 2010.

[23] L. Macalik, M. Maczka, P. Solarz, A. F. Fuentes, K. Matsuhira and Z. Hiroi, "Optical spectroscopy of the geometrically frustrated pyrochlore Ho2Ti2O7", *Optical Materials*, 31, 6, 790–794, 2009.

[24] G. Li, K. Fang, Y. Ou, W. Yuan, H. Yang, Z. Zhang and Y. Wang, "Surface study of the reconstructed anatase TiO2 (001) surface", *Progress in Natural Science*, 31,1, 2021.

[25] D. Komaraiah, E. Radha, N. Kalarikkal, J. Sivakumar, M. V. Ramana Reddy and R. Sayanna, "Structural, optical and photoluminescence studies of sol-gel synthesized pure and iron doped TiO2 photocatalysts", *Ceramics International*, 45, 25060–25068, 2019.

[26] Y. Doubi, B. Hartiti, L. Hicham, S. Fadili, A. Batan, M. Tahri, A. Belfhaili and P. Thevnin, "Effect of annealing time on structural and optical proprieties of TiO2 thin films elaborated by spray pyrolysis technique for future gas sensor application", *Materials Today: Proceeding*s, 3 (4), 823–827, 2020.

[27] A. M. Bolbol, O. H. Abd-Elkader, H. Elshimy, Z. I. Zaki, S. A. Shata, M. Kamel, A. S. Radwan and N.Y. Mostafa, "The effect of Zr (IV) doping on TiO2 thin film structure and optical characteristics", *Results in Physics*, 42, 2022.

[28] D. Nath, F. Singh and R. Das, "X-ray diffraction analysis by Williamson-Hall, Halder-Wagner and size-strain plot methods of CdSe nanoparticles- a comparative study", *Materials Chemistry and Physics*, 239 (1), 2020.

[29] G. Demircan, E. F. Gurses, B. Aktas, S. Yalcin, A. Acikgoz, G. Ceyhan and M. V. Balak, "Sol–gel synthesis of Si-ZnO, Ti-ZnO and Si-Ti-ZnO thin films: Impact of Si and Ti content on structural and optical properties", *Materials Today Communications*, 34, 105234, 2023.

[30] A. K. Deb and P. Chatterjee, "Microstrain and lattice disorder in nanocrystalline titanium dioxide prepared by chemical route and its relation with phase transformation", *Journal of Theoretical and Applied Physics*,14, 285–293, 2020.

[31] D. Sudha, S. Dhanapandian, C. Manoharan, A. Arunachalam, "Structural, morphological and electrical properties of pulsed electrodeposited CdIn2Se4 thin films", *Results in Physics*, 6, 599–605, 2016.

[32] S. M. AL-Shomar, "Synthesis and characterization of Eu3+ doped TiO2 thin films deposited by

spray pyrolysis technique for photocatalytic application", *Materials Research Express*, 8(2), 2021.

[33] E. S. Gadelmawla, M. M. Koura, T. M. A. Maksoud, I. M. Elewa, and H. H. Soliman, "Roughness parameters", *Journal of Materials Processing Technology*, 123 (1), 133-145, 2002.

[34] Z. Sun, V. F. Pichugin, K. E. Evdokimov, M. E. Konishchev, M. S. Syrtanov, V. N. Kudiiarov, K. Li and S. I. Tverdokhlebov, "Effect of nitrogen-doping and post annealing on wettability and band gap energy of TiO2 thin film", *Applied Surface Science*, 500, 144048, 2020.

[35] M. Sreemany and S. Sen, "Influence of calcination ambient and film thickness on the optical and structural properties of sol-gel TiO2 thin films", *Materials Research Bulletin*, 42(1), 177-189, 2007.

[36] D.Y . Lee, J.T. Kim, J. H. Park, Y. H. Kim, I. K. Lee, M. H. Lee, and B. Y. Kim, "Effect of Er doping on optical band gap energy of TiO2 thin films prepared by spin coating", *Current Applied Physics*, 13(7),1301-1305, 2013.

[37] T.S. Senthil and M. Kang, "Transparent thin film dye sensitized solar cells prepared by sol-gel method", *Bulletin of the Korean Chemical Society*, 34(4), 1188-1194, 2013.

[38] A. Nakaruk, C. Y. Lin, D. S. Perera and C. C. Sorrell, "Effect of annealing temperature on titania thin films prepared by spin coating", *Journal of Sol-Gel Science and Technology*, 55, 328–334, 2010.

[39] T. M. Wang, S. K. Zheng, W. C. Hao and C. Wang, "Studies on photocatalytic activity and transmittance spectra of TiO2 thin films prepared by r.f. magnetron sputtering method", *Surface and Coatings Technology*, 155, (2-3),141–145, 2002.

[40] M. Sreemany and S. Sen, "A simple spectrophotometric method for determination of the optical constants and band gap energy of multiple layer TiO2 thin films", *Materials Chemistry and Physics*, 83,169-177, 2004.

[41] P. Hervé, L. K. J. Vandamme, "General relation between refractive index and energy gap in semiconductors", I*nfrared Physics & Technology,* 35 (4), 609–615, 1994.

[42] S. K. Tripathy, "Refractive indices of semiconductors from energy gaps", *Optical Materials*, 46, 240–246, 2015.

[43] A. Chanda, S. R. Joshi, V. R. Akshay, S. Varma, J. Singh, M. Vasundhara and P. Shukla, "Structural and optical properties of multilayered un-doped and cobalt doped TiO2 thin films", *Applied Surface Science*, 536, 147830 2021.

[44] S. M. Al-Shomar, "Investigation the effect of doping concentration in Ruthenium-doped TiO2 thin films for solar cells and sensors applications", *Materials Research Express*, 7, 036409, 2020.

[45] B. Houng, C. C. Liu and M. T. Hung, "Structural, electrical and optical properties of molybdenum-doped TiO2 thin films", *Ceramics International*, 39 (4), 3669–367639, 2013.

[46] M. Subramanian, S. Vijayalakshmi, S. Venkataraj and R. Jayavel, "Effect of cobalt doping on the structural and optical properties of TiO2 films prepared by sol-gel process", *Thin Solid Films*, 516, 3776–3782, 2008.

[47] C. J. Brinker, G. C. Frye, A. J. Hurd and C. S. Ashley, "Fundamentals of sol-gel dip coating", *Thin Solid Films*". 201, 97–108, 1991.

[48] P.B. Nair, V. B. Justinvictor, G. P. Daniel, K. Joy, V. Ramakrishnan, D. D. Kumar, and P. V. Thomas, "Structural, optical, photoluminescence and photocatalytic investigations on Fe doped Tio2 thin films", *Thin Solid Films*, 2014.

[49] M. M. Rahman, K. M. Krishna, T. Soga, T. Jimbo, and M. Umeno, "Optical properties and X-ray photoelectron spectroscopic study of pure and Pb-doped TiO2 thin films", *Journal of Physics and Chemistry of Solids*, 60 (2), 201-210, 1999.

[50] J. Yu, H. Yu, C. H. Ao, S. C. Lee, J. C. Yu and W. Ho, "Preparation, characterization and photocatalytic activity of in situ Fe-doped TiO2 thin films", *Thin Solid Films*, 496 (2), 273-280, 2006.

[51] F. B. Li and X. Z. Li, "Photocatalytic properties of gold/gold ion-modified titanium dioxide for wastewater treatment", *Applied Catalysis A: General*, 228 (1-2), 15-27, 2002.

Süleyman Demirel Üniversitesi Fen Edebiyat Fakültesi Fen Dergisi https://dergipark.org.tr/sdufeffd
Süleyman Demirel University Faculty of Arts and Sciences Journal of Science e-ISSN: 1306-7575
Research Article, 2023, 18(3): 238-247, DOI: 10.29233/sdufeffd.1355393

Experimental Study on The Gamma Ray Absorption Properties of Lanthanum and Cerium Borides

Hasan Gulbicim[1,*], Aynur Ozcan[2], Nureddin Turkan[3], Mecit Aksu[4], Esra Kurt[5]

[1]Department of Nuclear Medicine, Medicine Faculty, Ondokuz Mayıs University, 55139, Samsun, TURKEY
https://orcid.org/0000-0003-4518-2509
*corresponding author: hasanglbcm@gmail.com
[2,5]Department of Physics, Faculty of Science, Gazi University, 06560, Ankara, TURKEY
https://orcid.org/0000-0003-2514-5460
https://orcid.org/0000-0001-8147-8791
[3]Department of Engineering Physics, Faculty of Engineering and Natural Sciences, Istanbul Medeniyet University, 34700, Istanbul, TURKEY
https://orcid.org/0000-0002-0452-9484
[4]Department of Chemistry, Faculty of Science and Literature, Duzce University, 81620, Duzce, TURKEY
https://orcid.org/0000-0002-9405-1217

(Received: 05.09.2023, Accepted: 03.10.2023, Published: 23.11.2023)

Abstract: The objective of this study is to investigate the mass attenuation coefficients (μ_m) of lanthanumhexaborides and ceriumhexaborides over a wide photon energy range emitted from the main radioactive sources used in medicine and industry. ^{125}I, ^{99m}Tc, ^{131}I, ^{137}Cs, ^{60}Co and ^{152}Eu gamma ray sources were used in the experiments. The materials synthesized in powder form were first pelletized and then irradiated by photon beams. At the end, it was seen that there is successful consistency between the obtained experimental data and the previous theoretical results. It was also observed that the investigated samples are comparable enough to the known standard gamma shielding materials, especially to lead which is one of the most common one. In conclusion, it is understood that the presently investigated samples have a promising aspect in terms of developing new shielding materials against gamma rays.

Key words: Gamma rays, Hexaborides, Mass attenuation coefficient, Shielding

1. Introduction

Nowadays, with the fast improvements in technology, the use of radiation sources have been significantly highlighted [1-7]. Gamma and x-rays are the types of radiation included in the title of ‘ionizing radiation’, which is increasingly [8-10] used in the area of nuclear power plants, agriculture, medicine and industry. The ionizing radiation sources have also expanded applications in many areas like nanoscience, biotechnology, semiconductor technology, biology, photochemistry, and geology [11,12].

The main idea of protection from radiation is protecting the employees and the public by ensuring that they get the lowest level of radiation dose as much as possible. The materials having higher densities and atomic numbers are especially accepted as good candidates of the materials which also having higher probability of radiation protection [13]. The protective shielding materials enable workers to expose the radiation not exceeding the juristical dose limits that can be received during the environmental applications.

Developing new protective materials for radiation has also been significant subject of research due to the requirements of getting rid of the harmful effects of ionizing radiation [14,16]. In the radiation shielding studies, the mass attenuation coefficients are the main coefficients to examine and get an idea of measuring the photon interactions with the substance [17,18]. The experimental investigation of μ_m for radiation shielding materials is significantly important besides obtaining theoretical simulation results for them. Thus, there are various theoretical [19,20] and experimental [21,22] studies that have investigated new generation materials for radiation shielding. The materials containing lead are traditional radiation protection materials used for shielding due to their capability of radiation absorption [23].

Some of other radiation shielding materials can be stated as glasses, alloys, thin films and polymer composites [24-29]. In one of the recent study, gamma ray shielding performance and characterization of the graphitic carbon nitride were investigated [30]. There are also some other studies stating that the materials containing Bi_2O_3 nanoparticles have better radiation shielding performance than bulk Bi_2O_3 [31,32]. Several rock samples from different regions of Najran, Kingdom of Saudi Arabia were collected and then evaluated for their shielding performance for γ-rays [33]. R. Arya and his collaborators studied on the next generation gamma ray shielding blocks developed using alumina industry waste [34]. In literature, there are also some theoretical and experimental studies investigating the ionizing radiation absorption properties of materials containing boron compounds [35-37].

Our purpose of this study is to investigate the gamma ray absorption properties of lanthanum and cerium borides experimentally and compare the feature results with the data that have been obtained by Monte Carlo method. So, the μ_m values of experimental results for the radiation absorption are compared with the calculated one obtained by using the developed code. At the end, it was seen that the presented results are very similar and consistent with the calculated ones done by MC along with also those of the previously investigated results for borosilicate, granite, vermiculite, concrete and lead. Thus, it was seen from also experiments that the lanthanum and the cerium borides have high absorption capability of gamma rays when compared to lead which is the standard shielding material.

2. Experimental and Theoretical Details

2.1. Synthesis of lanthanumhexaboride (LaB_6)

For the synthesis of lanthanumhexaboride, the reduction reaction of La_2O_3 with B_2O_3 was used under special conditions. 1 mmol La_2O_3, 6 mmol B_2O_3 and 25 mmol Mg powder were mixed in the porcelain crucible until homogeneous distribution was achieved. The contents of the crucible were heated in the muffle furnace up to 900°C and kept at this temperature for 4 hours and cooled to room temperature. After the cooled sample was transferred into a beaker, it was mixed in 1 M HCl for 24 hours and then kept in concentrated acid for the same time period. After the obtained black precipitate was washed twice with distilled water by filtering, it was dried in an oven at 120 °C, and then annealed at 450 °C for 2 hours.

2.2. Synthesis of ceriumhexaboride (CeB_6)

For the synthesis of ceriumhexaboride; 1 mmol CeO_2, 3 mmol B_2O_3 and 13 mmol Mg powder were thoroughly mixed in a porcelain crucible, and then such contents of the crucible were heated in a muffle furnace up to 800°C. It was kept at this temperature for 2 hours and cooled. The cooled sample was transferred into a beaker and mixed in 1 M

HCl for one day, and then it was kept in concentrated acid for one day too. After the obtained gray precipitate was filtered and washed twice with distilled water, it was dried in an oven at 120 °C and then annealed at 450 °C for 2 hours.

2.3. Preparation of pellet samples

In this part of the study, pelletizing the samples was carried out for the irradiation of LaB_6 and CeB_6 compounds, which were synthesized and obtained in powder form, as seen in Figure 1.

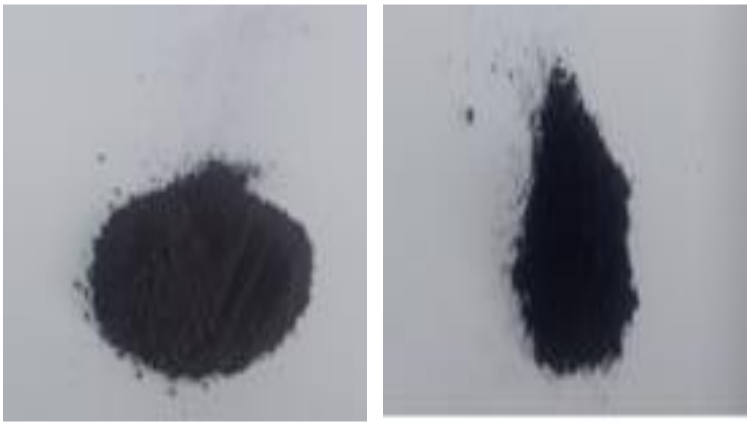

Figure 1. Appearance of LaB_6 and CeB_6 powder samples.

It is necessary to have certain physical properties in order to investigate the radiation absorption properties of materials. For this reason, the 30-ton press machine as seen in Figure 2 was used to make pellets from the synthesized samples. At this stage, cylindrical pellets with a diameter of 3 cm and a thickness of 3-6 mm were produced in a non-dispersible structure under high pressure.

Figure 2. Press machine with 30 tons capacity.

Pellets in desired physical dimensions were prepared, as seen in Figure 3, to be used in gamma spectroscopy system by pressing method under suitable conditions. Thus, the samples were prepared for the irradiation study to determine their radiation shielding properties.

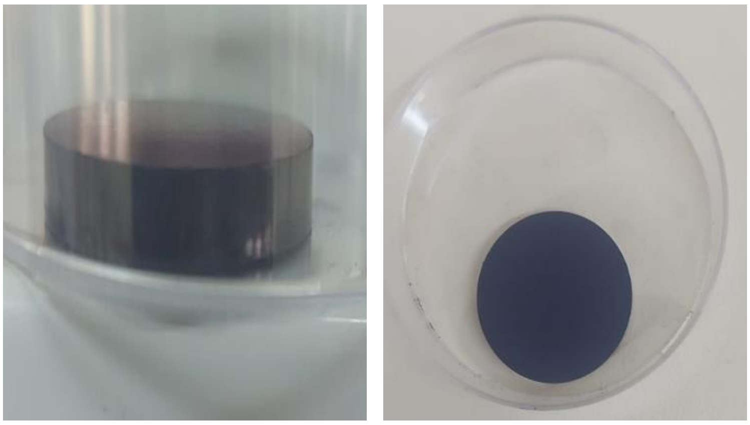

Figure 3. Top and side views of pelletized samples.

2.4. Gamma ray absorption spectroscopy

Gamma ray absorption properties of pellet samples having an appropriate physical size and composing of Lanthanumhexaboride and Ceriumhexaboride compounds were carried out by using two different scintillation detector systems. One of them is an ORTEC/905 Series mark/model gamma spectrometer system which has one block of thallium doped scintillation detector (NaI(Tl)). The experiments using this system were carried out in Nuclear Physics Laboratory located at the Faculty of Science of Ondokuz Mayıs University. The experimental analysis were practised using Scintivision-32 software, which is fully integrated into the calibrated system. The gamma energies of the radioisotopes used in this system are separated in the form of gaussian peaks by multi-channel analyzer. The other detector system is a GE/Discovery NM-630 mark/model gamma camera with multi-block NaI(Tl) detectors. This camera used in the experiments is located in the Nuclear Medicine Laboratory of Ondokuz Mayıs University-Faculty of Medicine. Narrow beam geometry was preferred in both systems used to examine the gamma ray absorption properties of pellet samples. Narrow beam geometry was created by beam collimation using lead cylinder. This cylinder has a diameter of 5 cm and a length of 20 cm, and its hole diameter is 3 mm. In both systems, after narrow beam collimation was achieved, the gamma rays were first dropped in the scintillation crystal. The crystal produces lots of scintillations, and the scintillations create electron avalanches in the photomultiplier tube. These electron avalanches are amplified by the applied voltage, producing an electrical signal proportional to the intensity of the radiation stored in the crystal. The experimental setup and schematic diagram of the both detector systems used are shown in Figure 4. The reason for using two different detector setups in this experimental study is that some radioisotopes and detector setups are located in different laboratories at the Ondokuz Mayıs University. While I-125, I-131 and Tc-99m radioisotopes and the gamma camera are located in the nuclear medicine laboratory, other radioisotopes and the ORTEC brand detector are located in the nuclear physics laboratory. Actually, both detector systems have a thallium-activated scintillation detector NaI(Tl). But the only difference between them is that the ORTEC detector has a single photomultiplyer tube (PMT) while the Gamma camera has multiple PMTs.

The attenuation of beam intensity in the same direction of the incidence due to absorption and scattering of beams is shown in Figure 5 at below. The radiation penetration and absorption properties of the materials as seen in the diagram of such figure are determined according to the Beer-Lambert law, also known as the exponential absorption law, which is also given in Equation 1 [5].

$$I=I_0 e^{-\mu \Delta x} \tag{1}$$

Here, Δx is the material thickness and μ is the linear attenuation coefficient. Here, I and I_0 are the radiation intensity in Becquerel (Bq) passing through the material and collected in the detector without the material, respectively. Since $I = I_0$ when there is no material between the source and the detector, I_0 is obtained for all radiation sources.

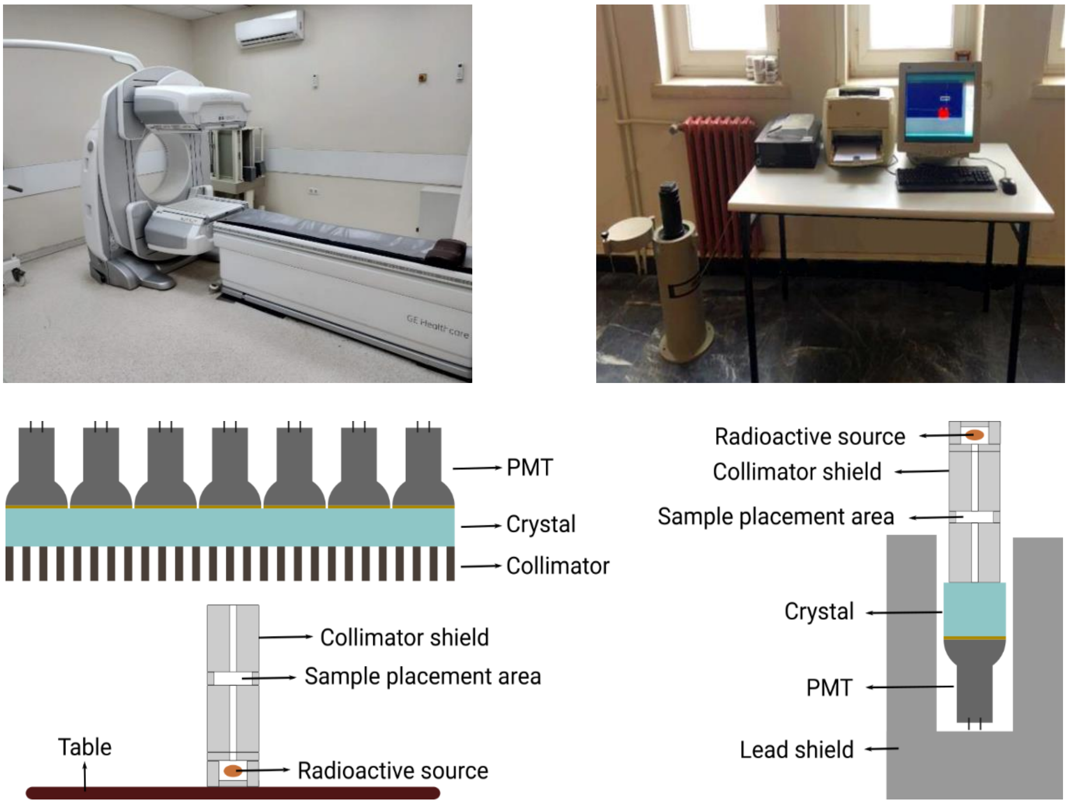

Figure 4. Gamma spectrometer measurement system with scintillation detector; a) GE/Discovery NM-630 Gamma camera and b) ORTEC/905 Series NaI(Tl) dedector.

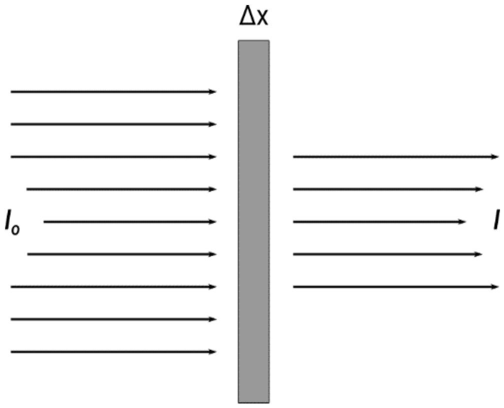

Figure 5. Schematic view of the attenuation in beam intensity.

When a material of Δx thickness is placed between the radiation source and detector, the linear attenuation coefficients (μ) are obtained. Since this coefficient varies with the different densities of the same materials, the μ_m value is much more used instead of μ [37]. This parameter is obtained by dividing the linear attenuation coefficient by the material density (Eq. 2).

$$\mu_m = {}^{\mu}/_{\rho} \tag{2}$$

In the measurements made using the ORTEC detector, the photon intensity was measured with and without the material, taking into account the channels falling within a certain width of the Gaussian peak corresponding to each energy value of the radioactive sources. Photon intensities in the measurements made with the gamma camera were counted by detector channels covering a circular area of 10 mm diameter in the center of the camera head. In this way, the photon absorption coefficients of the materials were obtained experimentally for each photon energy value by using the obtained I and I_0 values.

3. Results and Discussion

In order to calculate the mass attenuation coefficients, the density values of the cylindrical shaped pellet samples were determined experimentally by the classical method. Scales and digital steel calipers were utilized to achieve this precision. The theoretical density values of the synthesized samples and the obtained experimental results were given in Table 1. In order not to create a difference between the theoretical and the experimental data of the gamma ray absorption properties of the pellet samples, no additives were added to the samples during the pelletizing process since not to spoil the original content of the synthesized materials. So, just the cylindrical pellet samples having certain physical dimensions were prepared using a 30-tons press machine. For this reason, the obtained density values of the samples are lower than the theoretical values. It doesn't pose a problem in the comparison of the results since the density does not have an effect on the characteristic absorption parameter which also means the mass attenuation coefficient.

By the present study, the experimental and theoretical results of the mass attenuation coefficients at each energy value emitted from six different radioisotopes for LaB_6 and CeB_6 compound samples are given in Table 2.

Table 1. Theoretical and experimental density values of lanthanumhexaborides and ceriumhexaboride pellet samples.

Sample	**Density (g/cm^3)**	
	Experimental	**Theoretical [38]**
Ceriumhexaboride (CeB_6)	2.51	4.80
Lanthanumhexaboride (LaB_6)	1.92	4.72

Table 2. Theoretical and experimental mass attenuation coefficients of lanthanumhexaborides and ceriumhexaboride pellets for gamma energies emitted from six different radioisotopes.

Radioisotope	Gamma Energy (MeV)	Mass attenuation coefficients (μ/ρ)					
		CeB_6			LaB_6		
		EGSnrc [37]	XCom [37]	Experiment	EGSnrc [37]	XCom [37]	Experiment
^{125}I	0.021	19.7625	19.9400	7.3996	18.5308	18.7200	6.2341
^{99m}Tc	0.140	0.7450	0.7444	0.8082	0.7067	0.7060	0.5753
^{131}I	0.364	0.1334	0.1330	0.1778	0.1298	0.1294	0.1372
^{137}Cs	0.662	0.0776	0.0777	0.0824	0.0765	0.0766	0.0405
^{152}Eu	0.779	0.0693	0.0695	0.0541	0.0684	0.0686	0.0528
^{152}Eu	0.964	0.0606	0.0607	0.0518	0.0600	0.0601	0.0543
^{60}Co	1.173	0.0541	0.0540	0.0423	0.0536	0.0535	0.0801
^{60}Co	1.332	0.0504	0.0503	0.0689	0.0500	0.0499	0.0329
^{152}Eu	1.408	0.0488	0.0488	0.0334	0.0484	0.0484	0.0655

It is clearly understood from the data in Table 2 that there is a good agreement between the theoretical and experimental results. According to the data in the table, the biggest difference between the experimental and theoretical values was obtained for the ^{125}I source with 21 keV gamma energy. It can be said that the reason for this is that the beam energy is low for the 3 mm pellet thickness and the source activity for this radioisotope may also be insufficient. The obtained experimental results were compared to the XCom and the EGSnrc simulation results previously performed by Ozcan et al. [37] for these materials. It was understood that the calculated results in that study were comparable to lead, which is the standard shielding material, and it was strongly supported by the experimental data in this study. The comparisons of experimental data with the previous calculated results [37] for lanthanumhexaborides and ceriumhexaboride are shown in Figure 6.

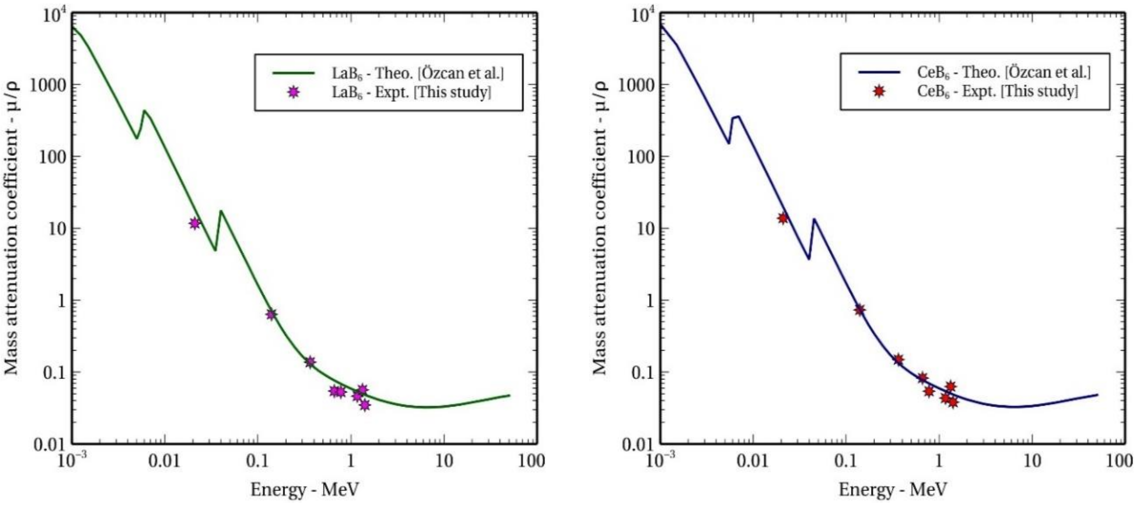

Figure 6. Comparison of the experimental data with the previous theoretical simulation results [37] for lanthanumhexaborides and ceriumhexaboride.

It is understood from the figure that the experimental values decrease exponentially with increasing energy values in consistency with the theoretical values. The small standard deviations appearing in this figure are thought to be the result of unnoticeable defects in the experimental setup like activity values of radioisotopes, or unavoidable statistical errors in the spectroscopy system. From such figure, it is generally seen that the experimental data and theoretical results are quite compatible with each other. The experimentally investigated materials of present study are quite well in terms of absorbing gamma radiation. In Figure 7, the radiation parameter of such materials are also compared to some other known shielding materials such as lead, vermiculite, borosilicate, granite and concrete.

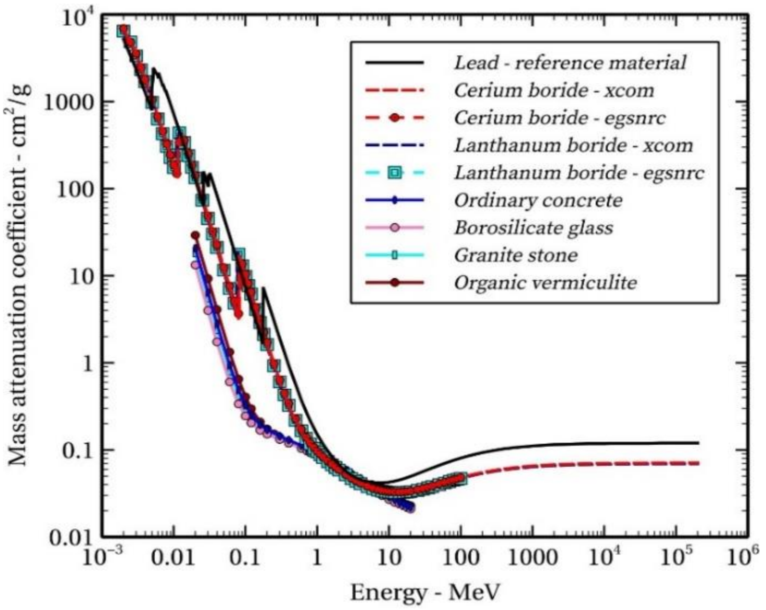

Figure 7. Comparison of the mass attenuation coefficients of lanthanumhexaboride and ceriumhexaboride with some other standard shielding materials (lead, granite, vermiculite, borosilicate and condrete) [36,39,40].

According to this figure, the boride compounds show graphical variations almost similar to lead, especially at gamma energies below 10 MeV. Below the energy of 2 MeV, it provides protectiveness of 92% radiation for 1.5 MeV, 85% radiation for 1 MeV, 63% radiation for 0.5 MeV and 34% radiation for 0.2 MeV, relative to the lead. In addition, according to the mass attenuation coefficients, it is observed that it has exactly the same absorptive property as lead at values corresponding to the K, L and M shell edges at some photon energies below 0.5 MeV. Variations in the mass attenuation coefficients corresponding to these edges can be seen from the peak jumps in the same figure. It should be kept in mind that these boride compounds have a quite low density values (4.80 g/cm^3 and 4.72 g/cm^3) when compared to lead (11.34 g/cm^3).

4. Conclusion

In this study, the mass attenuation coefficients, which are the characteristic parameter for radiation shielding, were experimentally determined for lanthanumhexaboride and ceriumhexaboride using radioactive sources having different gamma energies. The purpose of doing this is to know and understand the gamma absorption properties of such materials. So, it was understood that very appropriate results were obtained when the experimental data were compared to the previous theoretical findings. It is thought that in order to decide a material is a good candidate of radiation shielding material or not, it is a definite requirement to support theoretical ideas by experimental data. Thus, in this study, the expected theoretical results which were calculated previously are also obtained experimentally and it was seen that the results are quite promising ones for future studies that will be held on developing new radiation shielding materials synthesized in powder form. It was also understood from the densities of the hexaborides that being lighter than lead provides a significant advantage in terms of transportation of radiation shielding materials since lead is very heavy. Based on the obtained data, it was concluded that these materials, which are synthesized and produced in powder form, will play an important role in the development of gamma radiation shielding.

Authorship contribution statement

H. Gulbicim: Conceptualization, Methodology, Data Curation, Visualization; **A. Ozcan**: Original Draft Writing, Supervision/Observation/Advice; **N. Turkan**: Methodology, Original Draft Writing, Supervision/Observation/Advice; **M. Aksu**: Data Curation, Original Draft Writing; **E. Kurt**: Data Curation, Visualization.

Declaration of competing interest

The authors declare that they have no known competing financial interests or personal relationships that could have appeared to influence the work reported in this paper.

References

[1] R. Kurtulus, C. Kurtulus and T. Kavas, “Nuclear radiation shielding characteristics and physical, optical, mechanical, and thermal properties of lithium-borotellurite glass doped with Rb2O”, *Progress in Nuclear Energy*, 141, 103961, 2021.

[2] K. G. Mahmoud, M. I. Sayyed, D. A. Aloraini, A. H. Almuqrin and A. S. Abouhaswa, “. Impacts of praseodymium (III, IV) oxide on physical, optical, and gamma-ray shielding properties of boro-silicate glasses”, *Radiation Physics and Chemistry*, 207, 110836, 2023.

[3] A. Şengül, I. Akkurt, K. Gunoglu, K. Akgüngör and R. B. Ermis, “Experimental evaluation of gamma-rays shielding properties of ceramic materials used in dentistry”, *Radiation Physics and Chemistry*, 204, 110701, 2023.

[4] S. Dezhampanah, I. M. Nikbin, S. Mehdipour, R. Mohebbi and H. H. Moghadam, “Fiber- reinforced concrete containing nano - TiO2 as a new gamma-ray radiation shielding materials”, *Journal of Building Engineering*, 44, 102542, 2021.

[5] S. Kumar, K. S. Mann, T. Singh and S. Singh, “Investigations on the gamma-ray shielding performance of green concrete using theoretical, experimental and simulation techniques”, *Progress in Nuclear Energy*, 134, 103654, 2021.

[6] F. H. Sallam, M. Tharwat, A. H. Almuqrin, M. I. Sayyed and K. A. Mahmoud, “Ni0.5Zn0.5Fe2O4 nanoparticles reinforced polyester composite for advanced radiation shielding applications: A detailed discussion for synthesis, characterization, and gamma-ray attenuation properties”, *Radiation Physics and Chemistry*, 208, 110907, 2023.

[7] M. Elsafi, H. Al-Ghamdi, M. I. Sayyed, A. Antar, A. H. Almuqrin, K. A. Mahmoud, K. Cornish, T. I. Shalaby and A. M. El-Khatib, “Optimizing the gamma-ray shielding behaviors for polypropylene using lead oxide: a detailed examination”, *Journal of Materials Research and Technology,* 19, 1862-1872, 2022.

[8] J. H. Hubbell, “Photon Mass Attenuation and Energy-Absorption Coefficients”, *The International Journal Of Applied Radiation And Isotopes*, 33(11),1269–90, 1982.

[9] I. Akkurt, H. Akyıldırım, B. Mavi, S. Kilincarslan and C. Basyigit. “Photon Attenuation Coefficients of Concrete Includes Barite in Different Rate”, *Annals of Nuclear Energy,* 37(7), 910–14, 2010.

[10] C. Eke, O. Agar, C. Segebade and I. Boztosun, “Attenuation Properties of Radiation ShieldingMaterials Such as Granite and Marble against γ-Ray Energies between 80 and 1350 KeV”, *Radiochimica Acta*, 105(10), 851–63, 2017.

[11] J. Majid and A. Mohammadi, “Gamma Ray Attenuation Coefficient Measurement for Neutron-Absorbent Materials”, *Radiation Physics and Chemistry*, 77(5), 523–27, 2008.

[12] R. McCuen, “Book Reviews”, *JAWRA Journal of the American Water Resources Association*, 48(2), 407–10, 2012.

[13] J. M. Sharaf and M. S. Hamideen, “Photon Attenuation Coefficients and Shielding Effects of Jordanian Building Materials”, *Annals of Nuclear Energy*, 62, 50–56, 2013.

[14] G. C. Jagetia, “Radioprotective Potential of Plants and Herbs against the Effects of Ionizing Radiation”, *Journal of Clinical Biochemistry and Nutrition*, 40(2), 74–81, 2007.

[15] Y. Karabul, L. A. Susam, O. Içelli and Ö. Eyecioğlu, “Computation of EABF and EBF for Basalt Rock Samples”, *Nuclear Instruments and Methods in Physics Research, Section A: Accelerators, Spectrometers, Detectors and Associated Equipment*, 797, 29–36, 2015.

[16] M. Çağlar, H. Kayacık, Y. Karabul, M. Kılıç, Z. G. Özdemir and O. İçelli, “Na2Si3O7/BaO Composites for the Gamma-Ray Shielding in Medical Applications: Experimental, MCNP5, and WinXCom Studies”, *Progress in Nuclear Energy,* 117, 103-119, 2019.

[17] K. Ashok, “Gamma Ray Shielding Properties of PbO-Li2O-B2O3 Glasses”, *Radiation Physics and Chemistry,* 136, 50–53, 2017.

[18] A. Nigar, Z. Yüksel, E. Abbasov, H. Gülbiçim and M. Ç. Tufan, “Investigation of Gamma-Ray Attenuation Parameters of Some Materials Used in Dental Applications”, *Results in Physics*, 12, 2202–2205, 2019.

[19] A. Hakan, “Olivine Mineral Used inConcrete for Gamma-Ray Shielding”, *Arabian Journal of Geosciences*, 12(8), 1–8, 2019.

[20] M. Asghar and H. Ghiasi, “Shielding Properties of the Ordinary Concrete Loaded with Micro-and Nano-Particles against Neutron and Gamma Radiations”, *Applied Radiation and Isotopes*, 136, 27–31, 2018.

[21] H. O. Tekin, M. I. Sayyed, E. E. Altunsoy and T. Manici, “Shielding Properties and Effects of WO3 and PbO on Mass Attenuation Coefficients by Using MCNPX Code”, *Digest Journal of Nanomaterials and Biostructures*, 12(3), 861–67, 2017.

[22] M. G. Dong, M. I. Sayyed, G. Lakshminarayana, M. Çelikbilek, A. E. Ersundu, P. Nayar and M. A. Mahdi, “Investigation of Gamma Radiation Shielding Properties of Lithium Zinc Bismuth Borate Glasses Using XCOM Program and MCNP5 Code”, *Journal of Non-Crystalline Solids*, 468, 12–16, 2017.

[23] Z. Li, W. Zhou, X. Zhang, Y. Gao and S. Guo, S., “High-efficiency, flexibility and lead-free X-ray shielding multilayered polymer composites: layered structure design and shielding mechanism”, *Scientific Reports*, 11, 4384, 2021.

[24] Y. Kavun, S. Kerli, H. Eskalen and M. Kavgacı, “Characterization and nuclear shielding performance of Sm doped In_2O thin films”, *Radiation Physics and Chemistry*, 194, 110014, 2022.

[25] M. Alqahtani, F. Ercan, N. A. Saleh, M. H. A. Mhareb, N. Dwaikat, M. I. Sayyed, F. Abokhamis, A. Abdulrazzaq, B. Ozcelik and I. Ercan, “Structural, magnetic and gamma-ray shielding features of Zn doped Mg2FeTiO6 double perovskite”, *Physica B Condensed Matter*, 640, 414024, 2022.

[26] H. Yaykaslı, H. Eskalen, Y. Kavun and M. Gögebakan “Microstructural, thermal, and radiation shielding properties of Al50B25Mg25 alloy prepared by mechanical alloying”, Journal of Materials Science: Materials in Electronics, 33, 2350–2359, 2022.

[27] H. Eskalen, Y. Kavun, S. Kerli and S. Eken, “An investigation of radiation shielding properties of boron doped ZnO thin films”, *Optical Materials*, 105, 109871, 2020.
[28] Y. Kavun, H. Eskalen, S. Kerli and M. Kavgaci, “Fabrication and characterization of GdxFe2O3 (100-x)/PVA (x= 0, 5, 10, 20) composite films for radiation shielding”, *Applied Radiation and Isotopes*, 177, 109918, 2021.
[29] M. I. Sayyed, O. Agar, A. Kumar, H. O. Tekin, D. K. Gaikwad and S. S. Obaid, “Shielding behaviour of (20+ x) Bi2O3–20BaO–10Na2O–10MgO–(40–x) B2O3: An experimental and Monte Carlo study”, *Chemical Physics*, 529, 110571, 2020.
[30] Y. Kavun, H. Eskalen and M. Kavgacı, “A study on gamma radiation shielding performance and characterization of graphitic carbon nitride”, *Chemical Physics Letters*, 811, 140246, 2023.
[31] M. Elsafi, M. A. El-Nahal, M. I. Sayyed, I. H. Saleh and M. I. Abbas, “Effect of bulk and nanoparticle Bi2O3 on attenuation capability of radiation shielding glass”, *Ceramics International*, 47, 19651–19658, 2021.
[32] M. A. El-Nahal, M. Elsafi, M. I. Sayyed, M.U. Khandaker, H. Osman, B. H. Elesawy, I. H. Saleh and M. I. Abbas, “Understanding the effect of introducing micro-and nanoparticle bismuth oxide (Bi_2O_3) on the gamma ray shielding performance of novel concrete”, *Materials*, 14(21), 6487, 2021.
[33] A. Khan, A. Al-Alhareth, S. Mobark, W. Al-Mahri, N. Al-Sharyah, S. Al-Zmanan, H. B. Albargi and A. M. Abdalla, A.M., “Experimental and theoretical investigations of the γ-rays shielding performance of rock samples from Najran region”, *Annals of Nuclear Energy*, 183, 109676, 2023.
[34] R. Arya, R. Paulose, V. Agrawal, A. Pandey, D. Mishra, S. K. Sanghi and S. T. Salammal, “Next generation gamma ray shielding blocks developed using alumina industry waste”, *Construction and Building Materials*, 373, 130895, 2023.
[35] N. Ekinci, F. I. El-Agawany, A Gurol, Y. S. Rammah, E. M. Ahmed, D. Yılmaz, B. Aygün and M. Somer, “Physical properties, experimental and theoretical gamma-ray shielding”, *Radiation Physics and Chemistry*, 194, 110012, 2022.
[36] H. Gulbicim, M. N. Turkan, M. Aksu and S. Durmuş, “A study on the investigation of gamma shielding properties of some metal borides”, *Progress in Nuclear Energy*, 115, 107–114, 2019.
[37] A. Özcan, M. N. Türkan, M. Aksu, H. Gülbiçim and E. Kurt, “Magnezyotermik indirgeme ile sentezlenen Lantanyum hekzaborür (LaB6) ve Seryum hekzaborür (CeB6) malzemelerinin gama zırhlama özelliklerinin Monte Carlo simülasyonu”, *Gazi Üniversitesi Mühendislik Mimarlık Fakültesi Dergisi*, 38(2), 927-936, 2023.
[38] Y. Wang, K. C. Chou and G. H. Zhang, “Preparations of lanthanum hexaboride (LaB6) and cerium hexaboride (CeB6)”, *Journal of the American Ceramic Society*, 105(3), 1954-1966, 2022.
[39] H. Gülbiçim, M. Ç. Tufan and M. N. Türkan, “The investigation of vermiculite as an alternating shielding material for gamma rays”, *Radiation Physics and Chemistry*, 130, 112-117, 2017.
[40] D. Ickecan, M. N. Turkan and H. Gulbicim, “Investigation of shielding properties of impregnated activated carbon for gamma-rays”, *Applied Radiation and Isotopes*, 172, 109687, 2021.

Süleyman Demirel Üniversitesi Fen Edebiyat Fakültesi Fen Dergisi https://dergipark.org.tr/sdufeffd
Süleyman Demirel University Faculty of Arts and Sciences Journal of Science e-ISSN: 1306-7575
Research Article, 2023, 18(3): 248-258, DOI: 10.29233/sdufeffd.1265417

Adsorption of Uranium (VI) on organic cation-moded kula volcanite and optimization with surface response method (RSM)

Ümit H. Kaynar*[1], Sermin Çam Kaynar[2,]

[1] Department of Fundamental Sciences, Faculty of Engineering and Architecture, Izmir Bakırcay University, Menemen, 35030, Izmir, Turkey
https://orcid.org/0000-0002-3321-0341
*corresponding author: umit.kaynar@bakircay.edu.tr
[2] Department of Physics, Faculty of Arts and Sciences, Manisa Celal Bayar University, Muradiye, 45010, Manisa, Turkey

(Received: 15.03.2023, Accepted: 18.10.2023, Published: 23.11.2023)

Abstract: First of all, the structural characteristics of the prepared HDTMA-volcanite. such as XRF, SEM and BET surface area were examined, then uranium U(VI) adsorption from aqueous solutions was optimized by surface response method (RSM), which is widely used in industrial research. . Effective experimental conditions on adsorption efficiency: pH (3-8), time (30-150 minutes), uranium concentration (20-80 mg/L) and temperature (20-60 °C) were selected. The best possible combinations of these parameters were obtained by the surface response method (RSM). The central composite design (CCD) was chosen for the design of the experimental conditions. According to the RSM results, it was determined that the experimental design fit the quadratic model, and the R^2 and R^2_{adj} values, which are the parameters showing the model fit, were 0.98 and 0.95, respectively. HDTMA-Volk at optimum conditions. Adsorption capacity was obtained as 4.41 mg/g for the HDTMA-Volcanics at optimum conditions. The compatibility of the obtained data with adsorption isotherms was investigated, and thermodynamic parameters were calculated.

Key words: Adsorption, Uranium (VI), Volcanit, Response Surface Methodology (RSM)

---

1. Introduction

One of the most significant issues with nuclear technology is the removal, recovery, and storage of waste, which results in high expenditures. The elimination of pollution, especially caused by the expansion of the nuclear sector, is an important situation and is seen as a necessity for development today. Moreover, radioactive wastes that are generated in a variety of industries and sectors, including research, industry, and medicine, can be found in a variety of physical and chemical states. Chemical precipitation, coagulation, adsorption, ion exchange, biosorption [16], and other processes are the most efficient ways to remove radioactive materials and heavy metals. Due to the abundance of clays in our nation and the fact that they may be used to purify metals using the adsorption method, clays are often used as inorganic adsorbent materials. Modifying clays with long-chain quaternary amine cationic salts from organic cations increases their hydrophobicity, leading to improved adsorption of metal ions. This modification alters the structure from a hydrophilic silica surface to an organophilic surface, and the organic cation can easily bond to the adsorbent surface through electrostatic forces between the positive charges of the long-chain organic cations and the negative charges on the adsorbent surface [1]. Several adsorbents that are modified with organic cations are used as adsorbents in the literature [2-4].

In the environment, uranium (U) is typically found in its hexavalent form and is considered a toxic heavy metal due to its radioactive properties. It can be found in rocks, soils, and water, and can enter the environment through various sources, such as scientific research, industry, nuclear power plants, medicine, and weapons The US EPA has classified uranium as a confirmed human carcinogen (group A) [3], and the tolerable limit for its carcinogenic risk is 0.5 μg/kg body weight (or 35 μg for a 70 kg adult) [4]. While soluble uranium salts are toxic, their toxicity is generally less severe compared to other heavy metals such as mercury or lead. The kidneys are the organ most affected by uranium toxicity [4-9]. In a research conducted by Kutahyalı et al. [10], they determined that the sorption of strontium ions on untreated and HCl-treated Kula volcanic samples yielded calculations of 2.04 and 1.72 mg/g, respectively. In a study examined by Xi et al. (2009) [11], the adsorption capacity of 3.54 mg/g was shown under optimum conditions by using U(IV) solution in the adsorption of uranium on Hematite. In a different study, uranium adsorption was carried out on nano-MgO particles obtained by Kaynar et al. (2018b) ignition method. In the study, it was observed that the adhesion had multilayer adsorption and a sorption capacity of 128.4 mg/g [12].

The production of dangerous rays like alpha, beta, and gamma from the breakdown of atomic nuclei in radioactive materials like thorium and uranium can seriously affect both living things and the environment. Radioactive contamination has the potential to harm genetic material, impair immunological function, hasten the progression of cancer, and possibly result in fatalities [13].

The RSM (Response Surface Methodology) is a technique that utilizes statistical and mathematical modeling to evaluate the correlation between diverse observations obtained from different factors. Through the optimization of independent and dependent variables, RSM analyzes the theoretical and experimental data to investigate this correlation [14]. This methodology is extensively employed across various fields for enhancing and optimizing the process and obtaining a better understanding of how different variables impact the system under study [15,16].

This study focused on enhancing the adsorption capacity of the abundant and cost-effective alkali basaltic Kula volcanite by modifying it with an organic cation, HDTMA, for the removal of U(VI) from aqueous solutions. The effectiveness of the HDTMA-modified volcanite was evaluated and RSM for the adsorption of U(VI) from aqueous solutions. The goal was to investigate the feasibility of using organic-loaded volcanites in the removal and separation of U(VI) from aqueous solutions. Overall, this research aimed to develop a practical and cost-effective method for U(VI) removal and separation from aqueous solutions using modified volcanites.

2. Material and Method

The alkali basalt structure of the Kula volcanite used as an adsorbent in this study was derived from the volcanic zone surrounding Demirköprü Dam (Manisa). The study's chemical reagents were all analytical quality. The structure-modified quaternary ammonium (alkyl aryl ammonium) compound containing cationic surfactants utilized was straight chain hexadecyltrimethylammo-nium (HDTMA)-bromide ($C_{19}H_{42}NBr$, MA: 364.46 g, Sigma-Aldrich, purity: 99%). A thermostatic water bath shaker with the model number GFL-1083 was used to conduct the batch method adsorption investigations.

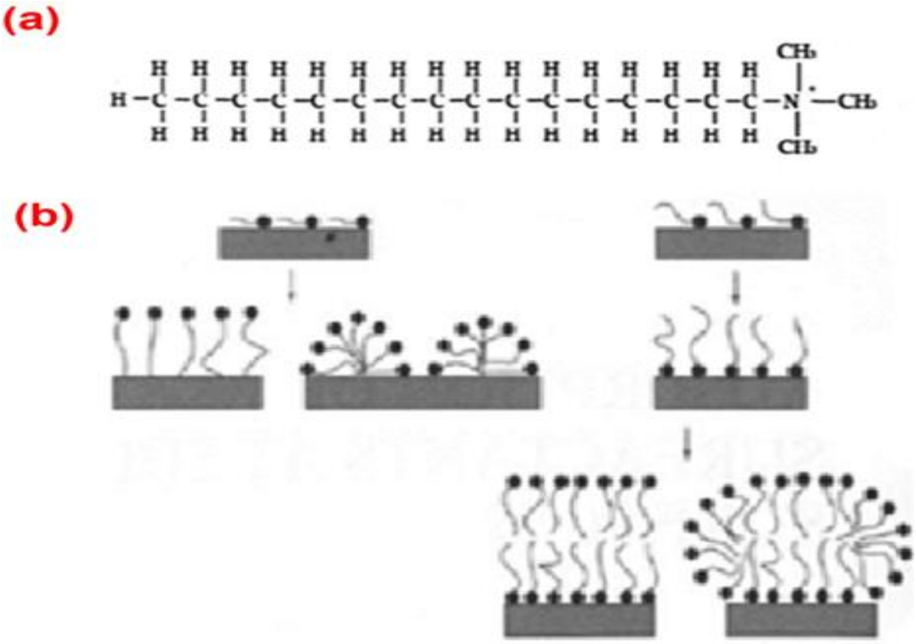

Figure 1. HDTMA molecule (a) and surface binding types (b)

2.1. Preparation of organo-volcanics

The volcanics were collected from three different locations around the Demirköprü dam extinct volcano region and washed thoroughly with pure water before undergoing organic cation modification. Subsequently, they were dried at 110 °C for 24 hours and crushed using jaw crushers. The volcanics were then treated with HDTMA salt solutions of 5, 10, 15, and 20 mM concentrations as organic matter and dried to prepare the modified organo-volcanites. The optimal concentration of 5 mM was chosen. The molecular structure and surface binding types of the organic cation HDTMA are depicted in Figure 1. The modified organo-volcanites were characterized using XRF, SEM, and BET surface area analysis.

2.2. Adsorption studies of uranium(VI)

For the uranium uptake studies from aqueous solutions, dilutions were made from a stock solution of 1000 ppm $UO_2(CH3COO)_2.2H_2O$. The modified Kula volcanic materials with HDTMA (5 mM) were used for the batch experiments. In each experiment, 0.375 g of modified volcanic material was mixed with 20 mL of uranium solution in a 50 mL tube. After centrifugation at 4500 rpm for 10 minutes, the supernatant was analyzed using ICP-OES (Perkin-Elmer Optima 2000 DV model Inductively Coupled Plasma-Optic Emission Spectrometry) to determine the remaining uranium concentration in the solution after adsorption.

2.3. Mathematical modeling of the experimental system

Response Surface Methodology

RSM is an analytical technique that employs statistical and mathematical models to investigate the relationship between multiple observations obtained under varying conditions [14]. By optimizing the values of independent and dependent variables, RSM allows for the comparison of theoretical and experimental data. Its application is widespread, as it enables the optimization and enhancement of processes, as well as the examination of the interrelationships between different variables that impact the system being studied [16].

Experimental design

The impact of each factor can be represented by a mathematical model derived from the scanning design and optimization. In addition to the experimental results, predicted outcomes can also be obtained. The statistical experimental design data is analyzed using multiple linear regression analysis, and response variables are described by polynomial functions. Subsequently, it is verified if the expected outcomes can be achieved experimentally.

$$y = b_o + \sum_{1}^{k} b_i x_i + \sum_{1}^{k} b_{ii} x_i^2 \sum_{i<j}^{k} b_{ij}\, x_i\, x_j + \varepsilon \quad (1)$$

In this study, the relationship between the response variable (y) and the independent variables (x1, x2, ..., xk) was expressed using a polynomial function that includes coefficients (b1, b2, ..., bk) determined by regression analysis. The interaction between factors was taken into account by including terms (bijxixj), and the curvature of the model was defined by including quadratic terms (biixi2). The error term (ε) was also included in the model. The optimal values of the independent variables were determined using the Minitab program.

Table 1. Independence Factors and their Coded Levels Used for Optimization.

Parameters	**Code**	-2	-1	0	1	2
pH	X1	3	4	5	6	8
Concentration	X2	20	40	50	60	80
Temperature (C)	X3	20	30	40	50	60
Time (t)	X4	30	60	90	120	150

3. Results

3.1. Characterization of adsorbents

The original basaltic volcanic sample analyzed in this study was found to have a chemical composition consisting of various elements, including SiO_2, Al_2O_3, Fe_2O_3, MnO, MgO, CaO, Na_2O, K_2O, TiO_2, P_2O_5, and other trace elements. The percentages of each element were measured, with SiO_2 being the most abundant at 48.4%, followed by Al_2O_3 at 17.66%, and Fe_2O_3 at 8.648%. Other elements found in smaller quantities included MnO at 0.085%, MgO at 8.538%, CaO at 6.234%, Na_2O at 3.989%, K_2O at 2.881%, TiO_2 at

1.85%, P_2O_5 at 0.625%, and other trace elements at 1.09% [17]. The analysis of the chemical composition provided important information about the properties of the original basaltic volcanic sample and informed the subsequent modification and use of the material in the study.

The SEM images of the volcanic adsorbent modified with organic cation were obtained using the QUANTA 400 F Field Emission-SEM and are presented in Figure 2. The EDS was also utilized to examine the elements in the pore structure and their percent distributions. The images are magnified x3000 times, and the crystalline dimensions appear to be in the micro-meter scale. The images indicate that the organic cation-modified surface completely covers the volcanic surface. Compared to normal volcanite, an increase in carbon percentage of 6.32% was observed in HDTMA-volcanite. The surface area changes of the raw and HDTMA modified volcanic samples were determined, and the results are presented in Table 2. The HDTMA modification increased the surface area of Kula volcanite to 3,689 (m^2/g).

Table 2. Surface area changes of unmodified and HDTMA modified -volcanite samples.

	Unmodified volcanite	HDTMA-volcanite
Surface area (m^2/g)	1,265	3,152

3.2. Experimental design results

The study aimed to optimize the amount of uranium (VI) adsorbed (mg/g) by using RSM and optimizing certain parameters including pH, temperature, initial U(VI) concentration (mg/L), and time. The optimal conditions were determined through RSM, and subsequent experiments were conducted to assess the effect of these parameters using the central composite design (CCD) method, a type of RSM method. A total of 31 experiments were conducted, with seven at the center point. The results obtained from the designed experimental conditions are presented in Table 3.

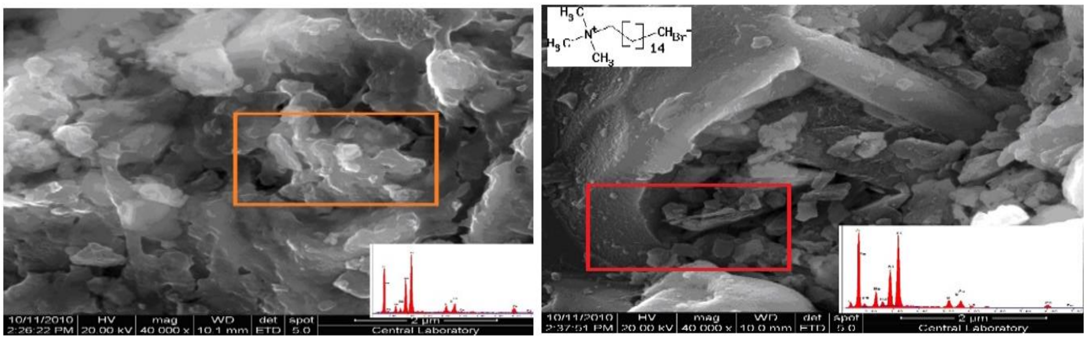

Figure 2. SEM image (x40000) and EDS distribution of raw and HDTMA-volcanics

Table 3. Central composite design model for U(VI) adsorption by HDTMA-Volcanics

Run Order	x_1	x_2	x_3	x_4	pH	Const	Temp	Time	Response (mg/g)	
									Predicted value (mg/g)	Observed value (mg/g)
1	1	1	1	1	6	60	50	120	3,20	3,15
2	1	1	1	-1	6	60	50	60	3,25	3,15
3	1	1	-1	1	6	60	30	120	3,04	3,04
4	1	1	-1	-1	6	60	30	60	3,07	3,02
5	1	-1	1	1	6	40	50	120	1,99	2,07
6	1	-1	1	-1	6	40	50	60	2,01	2,11
7	1	-1	-1	1	6	40	30	120	1,92	2,07
8	1	-1	-1	-1	6	40	30	60	1,92	2,06
9	-1	1	1	1	4	60	50	120	3,22	3,11
10	-1	1	1	-1	4	60	50	60	3,20	3,15
11	-1	1	-1	1	4	60	30	120	3,15	3,15
12	-1	1	-1	-1	4	60	30	60	3,12	3,08
13	-1	-1	1	1	4	40	50	120	1,97	2,12
14	-1	-1	1	-1	4	40	50	60	1,92	1,97
15	-1	-1	-1	1	4	40	30	120	1,99	2,13
16	-1	-1	-1	-1	4	40	30	60	1,93	2,07
17	2	0	0	0	8	50	40	90	2,53	2,47
18	-2	0	0	0	3	50	40	90	2,56	2,49
19	0	2	0	0	5	80	40	90	3,84	4,11
20	0	-2	0	0	5	20	40	90	1,44	1,04
21	0	0	2	0	5	50	60	90	2,60	2,64
22	0	0	-2	0	5	50	20	90	2,45	2,28
23	0	0	0	2	5	50	40	150	2,52	2,42
24	0	0	0	-2	5	50	40	30	2,51	2,49
25	0	0	0	0	5	50	40	90	2,63	2,68
26	0	0	0	0	5	50	40	90	2,63	2,53
27	0	0	0	0	5	50	40	90	2,63	2,66
28	0	0	0	0	5	50	40	90	2,63	2,68
29	0	0	0	0	5	50	40	90	2,63	2,52
30	0	0	0	0	5	50	40	90	2,63	2,61
31	0	0	0	0	5	50	40	90	2,63	2,41

The quadratic equation that predicts the amount of uranium adsorbed (mg/g) was derived from the evaluation of the obtained results.

$$Q\ (\text{mg/g}) = 2{,}629 - 0{,}007X_1 + 0{,}6X_2 + 0{,}039X_3 + 0{,}003X_4 - 0{,}021X_1X_1 + 0{,}003X_2X_2 - 0{,}026X_3X_3 - 0{,}028X_4X_4 - 0{,}01\,X_1X_2 + 0{,}024\,X_1X_3 - 0{,}016\,X_1X_4 + 0{,}022\,X_2X_3 - 0{,}009\,X_2X_4 - 0{,}005\,X_3X_4$$

Table 5 shows the second-order analysis of variance (ANOVA) of the response surface, which is used to test the statistical significance of the equation using the F-test. The obtained F-value of 23.04 indicates that the experimental results obtained by varying the factor levels are highly significant at a 95% confidence level. The model is considered compatible since the probability (P) value is less than 0.0001. The close proximity of R^2 and R^2_{Adj} (0.98-0.95) values for the quadratic model obtained for adsorbed uranium amount (mg/g) indicates that the predicted values by the model and the experimental values are in excellent agreement. The significance of the coefficients in front of the model variables was assessed using p-values in Table 4, where p-values less than 0.05 indicate that the first-order effect of increasing uranium initial concentration is significant in predicting the amount of adsorbed uranium (mg/g) using the model.

Table 4. Estimated regression coefficient and corresponding tand P values.

Regression	Coefficients	Standart error	T	P
Intercept	2,629	0,062	42,217	7,74E-18
x1	-0,007	0,034	-0,200	0,8438
x2	0,600	0,034	17,851	5,48E-12
x3	0,039	0,034	1,150	0,2670
x4	0,003	0,034	0,102	0,9197
x1^2	-0,021	0,031	-0,677	0,5079
X2^2	0,003	0,031	0,104	0,9185
X3^2	-0,026	0,031	-0,837	0,4149
X4^2	-0,028	0,031	-0,899	0,3818
X1X2	-0,010	0,041	-0,231	0,8202
X1X3	0,024	0,041	0,572	0,5751
X1X4	-0,016	0,041	-0,392	0,7005
x2x3	0,022	0,041	0,522	0,6086
x2x4	-0,009	0,041	-0,213	0,8341
x3x4	-0,005	0,041	-0,117	0,9085

Table 5. Analysis of variance (ANOVA) for the regression model for U(VI) adsorption efficiency.

ANOVA	Df	SS	MS	F	Probability F
Regression	14	8,76	0,63	23,04	5,77E-08
Residuals	16	0,43	0,03		
Total	30	9,19			
R^2 : 0.98, R^2_{adj} : 0.95					

Three-dimensional surface graphs of the parameters affecting the U(VI) adsorption are given in Figure 3. In the adsorption of U(VI) on HDTMA-volcanic, according to the three-dimensional surface graphics; In Figure 4a, changes depending on the time and concentration, which are the adsorption parameters at constant pH (5.5) and temperature (40 °C), are seen. When the effect of concentration was examined as a parameter, it was observed that the best adsorption occurred at 80 mg/L and the amount of adsorbed U(VI) increased proportionally as the concentration increased. According to the graph, the maximum amount adsorbed reached 3.9 mg/g. When pH and initial U(VI) concentration (mg/L) were evaluated together, an increase in the amount of adsorption was observed for both parameters. At a concentration of 80 mg/L U(VI) at pH 5.5, it reached 4.13 mg/g adsorption values (time 90 min.; temperature 40 °C). When the changes in pH and time at constant temperature (40 °C) and concentration (50 mg/L) were examined, it was determined that the adsorption amount reached 2.55 mg/g in pH

5.5 and 120 minutes. In adsorption, temperature and pH were found to have positive effects on adsorption and it is shown in Figure 3 (d). When the time and temperature were evaluated together, the amount of adsorption increased with the increase in time and a decrease was observed after a certain value (Figure 3 e). With the increase of the adsorption time, it reached the maximum adsorption values of 2.52 mg/g at 120 min and pH 5.5. When the concentration and temperature are evaluated together in a constant time (90 min) and pH environment, both have a positive effect on the increase, and the maximum U(VI) adsorption was observed as 4.16 mg/g at 58^{o}C (Figure.3-f).

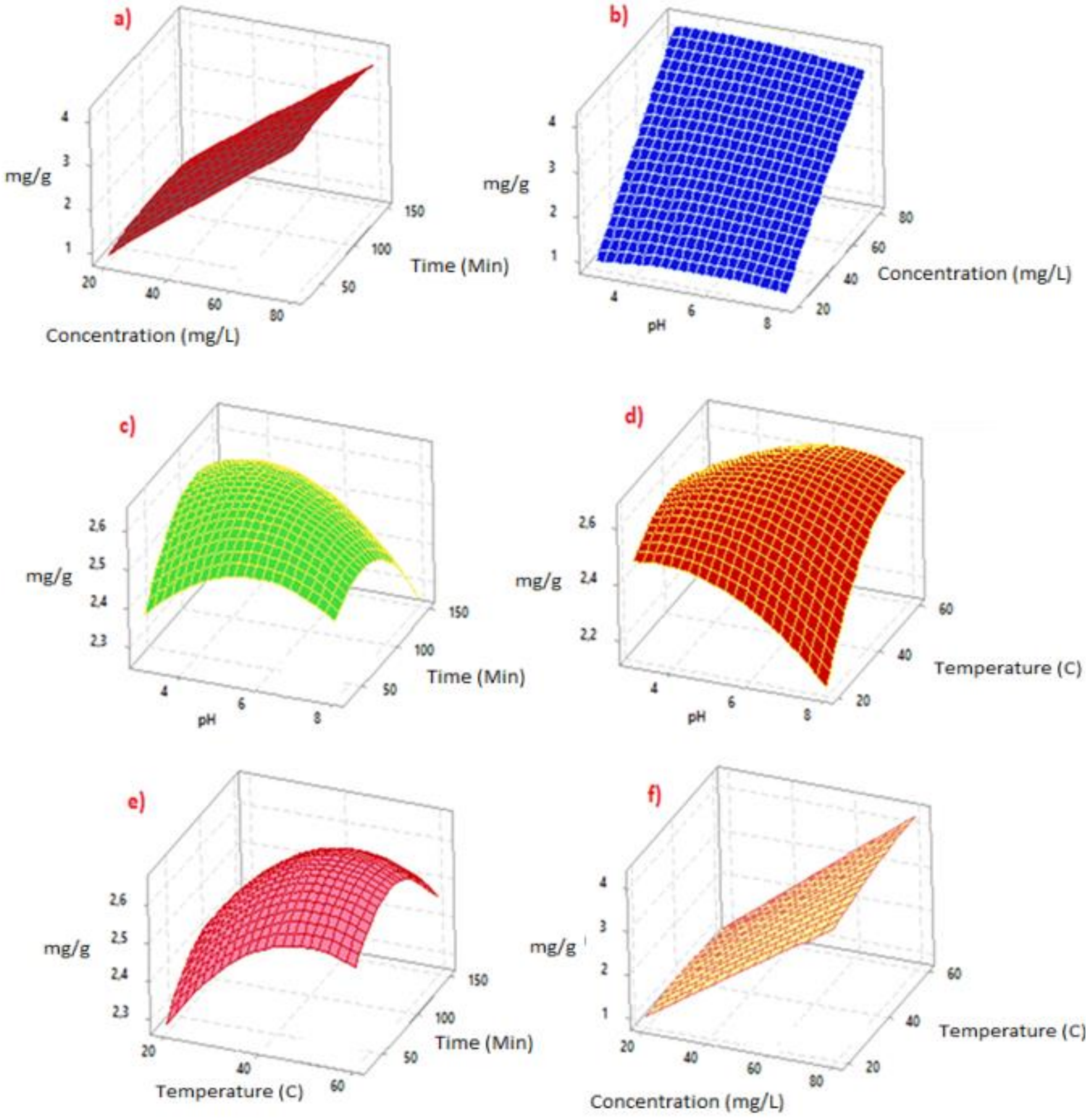

Figure 3. (a-f) Response surface graphs for interactions of investigated parameters of U(VI) adsorption onto HDTMA- volcanics

Optimum conditions for maximum adsorption were determined by conducting comparison experiments with the model. The optimal values were found to be pH 5.75, initial uranium concentration of 80 mg/L, temperature of 59.8 °C, and a duration of 40 minutes. The model predicted that the amount of adsorbed uranium at these optimum points would be 3,918 mg/g. In the experiments performed under these optimum conditions, the adsorption of U(VI) on HDTMA-volcanite was found to be 4.41 mg/g.

When the literature is examined, it is seen that HDTMA-Volcanite is a good adsorbent for U(VI) (Table 6).

Table 6. U(VI) uptake capacities of different adsorbents

Adsorbents	**q(mg/g)**	**pH**	**References**
Hematite	1.63	7	[18]
Talc	2.19	5	[19]
DEEA organo-volcanics	2.2	5	[20]
HDTMA-modified volcanite	4,41	5,75	This study

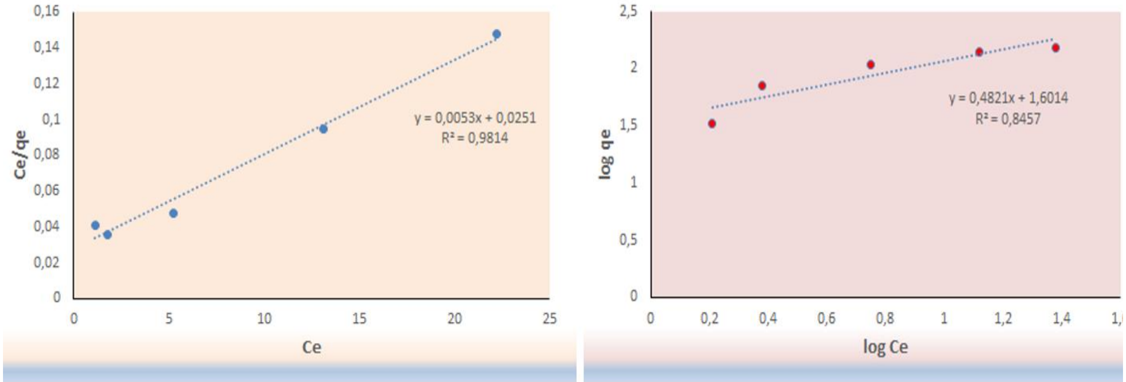

Figure 4. Langmuir and Freundlich adsorption isotherm for U(VI)

Based on the experimental data obtained from uranium adsorbed from aqueous solutions using organic cationic volcanic adsorbent, it was found that the adsorption isotherms followed Langmuir type adsorption (R^2 = 0.9814) (Figure. 4). Furthermore, when the thermodynamic parameters were analyzed, it was determined that the adsorption enthalpy (ΔH) was 3.5 kJ/mol, the free energy change (ΔG) was -18.07 kJ/mol, and the entropy change (ΔS) was 0.07 kJ/Kmol for the adsorption of uranium on HDTMA-volcanite. The positive value of ΔH indicates that the adsorption is endothermic. The observation that the free energy exchange ΔG has smaller values with increasing temperature under optimal conditions suggests that the adsorption process is spontaneous at high temperatures. Based on this information, it can be concluded that the uranium adsorption onto HDTMA-volcanite is a physical adsorption process. These findings have important implications for the use of HDTMA-volcanite in the removal and separation of U(VI) from aqueous solutions.

4. Results and discussion

The elimination of radionuclide pollution resulting from the nuclear industry is not only vital but also challenging and expensive. Advanced facilities and technologically applicable, economical methods are required for the removal, purification, and separation of radioactive elements from the environment, especially from uranium and thorium mining. In this study, it was found that a natural adsorbent called Kula volcanite, modified with an organic cation, can be a useful U(VI) remover. This adsorbent is locally sourced, readily available in large quantities, and can be modified with ecologically harmless organic cations to increase its adsorption capacity. Thus, it offers many advantages as a viable method for the removal of radionuclides that are costly to eliminate as waste. The development of Kula volcanite's features for the removal of hazardous metal ion wastes from the environment is significant for both the country's economy and the elimination of potential dangers and problems resulting from such wastes in the environment.

References

[1] Upson, R. T., Burns, S. E. 2006. Sorption of nitroaromatic compounds to synthesized organoclays. J. Colloid Interface Sci. 297, 70–76.

[2] Ryu, C. H., Yeo, S. D. 2010. Vapor phase adsorption of trichloroethane using organically modified montmorillonite. j. Ind. Eng. Chem. 377, 441-449.

[3] Majdan, M., Pikus, S., Gajowiak, A., Gladysz-Plaska, A., Krzyzanowska, H., Zuk, J., Bujacka, M. 2010. Characterization of uranium(VI) sorption by organobentonite. Appl. Surf. Sci. 256-17, 5416-5421.

[4] Shen, Y. H. 2004. Phenol sorption by organoclays having different charge characteristics. Colloids and Surfaces A: Physicochem. Eng. Aspects 232, 143–149.

[5] Benedict B, Pigford TH, Levi HW (1981) Nuclear chemical engineering. Mc Graw-Hill, New York

[6] Xie SB, Yang J, Chen C, Zhang XJ, Wang QL, Zhang C (2008) J Environ Radiact 99:126

[7] U.H. Kaynar, M. Ayvacıklı, S.C. Kaynar et al., Removal of uranium(VI) from aqueous solutions on nanoporous ZnO by manufactured microwave-assisted combustion synthesis. J. Radioanal. Nucl. Chem. 299, 1469–1477 (2014).

[8] US Environmental Protection Agency (1992) Integrated Risk Assessment System. Retrieval for metals, 9/14/92. Micromedeex Inc, Denver

[9] Shuibo X, Chun Z, Xinghuo Z, Jing Y, Xiaojlan Z, Jingsong W (2009) J Environ Radioact 100:162

[10] C. Kutahyalı, C. Cetinkaya, B. Acar M.B. Investigation of strontium sorption ont Kula volcanic using central composite design. J. Hazard. Mater. 201–202, 115–124 (2012).

[11] Xi, S., Zhang, C., Xinghuo, Z., Jing, Y., Xiaojian, Z., Jingsong, W. 2009. "Removal of uranium (VI) from aqueous solution by adsorption of hematite", J. Environ. Radioact, 100: 162-166

[12] Kaynar, U.H. 2018b. "A Modeling and Optimization Study by Response Surface Methodology (RSM) on UO_2^{2+} İons Adsorption Using Nano-MgO Particles" Inorganic and Nano-Metal Chemistry, 48-3: 187-195

[13] Hollriegl, V., Greiter, M., Giussani, A., Gerstmann, U., Michalke, B., Roth, P., Oeh, U. 2007. Observation of changes in urinary excretion of thorium in humans following ingestion of a therapeutic soil. J.Environ. Radioact. 95, 149–160.

[14] S., Malik, A., Satya, S. 2009. Application of response surface methodology (RSM) for optimization of nutrient supplementation for Cr(VI) removal by aspergillus lentulusAML05. J.Hazard.Mater. 164, 1198–1204.

[15] Cao, J., Wu, Y., Jin, Y., Yilihan, P., Huang, W. 2014. Response surface methodology approach for optimization of the removal of chromium (VI) by NH2-MCM -41. J. Taiwan Inst. Chem. Eng. 45, 860–868.

[16] Bezerra, M. A., Santelli, R. E., Oliveira, E. P., Villar, L. S., Escaleira, L. A. 2008. Response surface methodology (RSM) as a tool for optimization in analytical chemistry. Talanta, 76, 965–977.

[17] Helvacı, C. and Erkül F. 2001. Volcaniclastic rocks. Formation, general characteristics and classification. DEÜ, Engineering Faculty Publications, No: 285, Izmir (in Turkey),s: 93.

[18] Sprynskyy, M., Kovalchuk, I., Buszewski, B., 2010. The separation of uranium ions by natural and modified diatomite from aqueous solution. J. Hazard. Mat.181, 700–707.

[19] Liu, Y., Liu, Y., Cao, X., Hua, R., Wang, Y., Pang, C., Hua, M., Li, X. 2011. Biosorption studies of uranium (VI) on cross-linked chitosan: isotherm, kinetic and thermodynamic aspects. J. Radioanal. Nucl. Chem. 290(2), 231-239.

[20] Zhao, D., Wang, X., Yang S. et al., 2012. Impact of water quality parameters on the sorption of U(VI) onto hematite. J. Environ. Radioact. 103, 20–29.

[21] Sprynskyy, M., Kowalkowski, T., Tutu, H. et al., 2011. Adsorption performance of talc for uranium removal from aqueous solution. Chem. Eng. J. 171, 1185–1193.

[22] KAYNAR, U.H., HIÇSÖNMEZ, U., ÇAM -KAYNAR, S., KOÇAK, S. 2018. Sorption of uranium (VI) from aqueous solutions by DEEA- organovolcanic: Isotherms and thermodynamic studies, Nucl. Sci. Techn. 29:30,

[23] Zhang, Z., Zhou, Y., Liu, Y. H., Cao, X. H., Zhou, Z. W., Han, B., Liang, P., Xiong, G. 2014. Removal of thorium from aqueous solution by ordered mesoporous carbon CMK-3. J. Radioanal. Nucl. Chem., 302(1), 9–16.

[24] Ilaiyaraja, P., Deb, A.K.S., Sivasubramanian, K., Ponraju, D., Venkatraman, B. 2013. Removal of thorium from aqueous solution by adsorption using PAMAM dendron- functionalized styrene divinyl benzene, J. Radioanal. Nucl. Chem. 297, 59–69.

Süleyman Demirel Üniversitesi Fen Edebiyat Fakültesi Fen Dergisi https://dergipark.org.tr/sdufeffd
Süleyman Demirel University Faculty of Arts and Sciences Journal of Science e-ISSN: 1306-7575
Research Article, 2023, 18(3): 259-267, DOI: 10.29233/sdufeffd.1318890

Solutions to Differential-Differential Difference Equations with Variable Coefficients by Using Fourier Transform Method

Murat Düz [1], Sunnet Avezov [2], Ahmad Issa[3,*]

[1]Department of Mathematics, Faculty of Science, Karabük University, Karabük, TÜRKİYE
https://orcid.org/0000-0003-2387-4045
[2] Department of Mathematics, Faculty of Science, Yıldız Technical University, Istanbul, TÜRKİYE
https://orcid.org/0009-0007-6798-4189
[3] Department of Mathematics, Faculty of Science, karabük University, Karabük, TÜRKİYE
https://orcid.org/0000-0001-7495-3443
*corresponding author: ahmad93.issa18@gmail.com

(Received: 23.06.2023, Accepted: 26.10.2023, Published: 23.11.2023)

Abstract: In this paper, differential-differential difference equations with variable coefficients have been solved using the Fourier Transform Method (FTM). In addition, new definitions and theorems are introduced. Besides, the efficiency of the proposed method is verified by solving five important examples. Furthermore, we have noted that the Fourier transform method is a powerful technique for solving ordinary differential difference equations (ODDEs) with variable coefficients. It involves transforming the ODDEs into the frequency domain using the Fourier transform, solving the transformed equation, and then applying the inverse Fourier transform to obtain the solution in the time domain.

Key words: Linear differential equation, Variable coefficients, Fourier transform, Dirac delta function

---

1. Introduction

Differential equations are a fundamental concept in mathematics that describes how a function changes over time or in relation to other variables. They are widely used in various scientific fields, such as physics, engineering, economics, and biology, to model and understand natural phenomena, processes, and many other phenomena [7,9]. By studying the behavior and solutions of differential equations, we can gain insights into the underlying dynamics of these systems and make predictions about their future behavior. Differential difference equations combine both differential equations and difference equations, and they involve both continuous and discrete time variables. Solving such equations can be challenging, and various methods have been developed to address them. Here are some commonly used approaches: Laplace Transform, Elzaki transform [1], Taylor polynomial method [6], Mahgoub transform [2], differential transform method [8], and Generalized differential transform method [10].

In this article, we will solve ordinary differential- differential difference equations with variable coefficients given by the following formula :

$$\sum_{i=0}^{n}\sum_{k=0}^{m} C_{ik}(x)y^{(i)}(x-\mu_{ik}) = q(x)\,,\mu_{ik} \geq 0$$

The organization of the article is as follows: In the second section, new concepts and theories related to the proposed method were given. In the third section, five examples of differential equations and differential difference equations were solved, and finally the conclusion in the fourth section

2. Definitions and Theorems of Fourier Transform

Definition 2.1. [3] The Fourier transform of $f(t)$ is given by

$$\mathcal{F}[f(t)] = F(w) = \int_{-\infty}^{\infty} f(t).\, e^{-iwt} dt \tag{1}$$

Definition 2.2. [3] The inverse Fourier transform of $F(w)$ is given by

$$f(t) = \mathcal{F}^{-1}[F(w)] = \frac{1}{2\pi}\int_{-\infty}^{\infty} F(w)\, e^{iwt} dw \tag{2}$$

Theorem2.1. If $a, b \in R$. Then

$$\mathcal{F}[af_1(t) + bf_2(t)] = a\mathcal{F}[f_1(t)] + b\mathcal{F}[f_2(t)]$$

That means: The Fourier Transform is a linear combination.

Theorem2.2. [4] Let $f(t)$ be continuous or partly continuous in $(-\infty, \infty)$ and $f(t), f'(t), f''(t), \dots, f^{(n-1)}(t) \to 0$ for $|t| \to \infty$.

Also, If $f(t), f'(t), f''(t), \dots, f^{(n-1)}(t)$ are absolutely integrable in $(-\infty, \infty)$, then

$$\mathcal{F}\left[f^{(n)}(t)\right] = (iw)^n \mathcal{F}[f(t)] \tag{3}$$

Definition 2.3. [5] The Dirac delta distribution is limit for $\varepsilon \to 0$ function defined by

$$\delta_\varepsilon(t) = \begin{cases} \frac{1}{\varepsilon}, & 0 < t < \varepsilon \\ 0, & t < 0 \\ 0, & t > \varepsilon \end{cases}$$

That is $\delta(t) = \lim_{\varepsilon \to 0} \delta_\varepsilon(t)$.

And it's properties are given by

i. $\int_{-\infty}^{\infty} \delta(t) dt = 1$
ii. $\int_{-\infty}^{\infty} f(t)\delta(t - t_0) dt = f(t_0)$
iii. $\int_{-\infty}^{\infty} f(t)\delta^{(n)}(t - t_0) dt = (-1)^n f^{(n)}(t_0)$
iv. $\delta^{(n)}(w - w_0) = n!\,(-1)^n \frac{\delta(w-w_0)}{(w-w_0)^n}$
v. $\int_{-\infty}^{\infty} \frac{\delta(w-w_0) f(w)}{(w-w_0)^n} dw = \frac{1}{n!}\frac{d^n f(w)}{dw^n}\Big|_{(w=w_0)}$,

where $\delta(w - w_0)$ is given by

$$\delta(w - w_0) = \begin{cases} 0, & w \neq w_0 \\ \infty, & w = w_0 \end{cases} \tag{4}$$

Definition 2.4. [4] The Heaviside function is defined by

$$H(t) = \begin{cases} 1, & t > 0 \\ 0, & t < 0 \end{cases} \tag{5}$$

Lemma 2.1. $H'(t) = \delta(t)$

Theorem 2.3. The Fourier transform of $\delta(t)$ is 1. That means $\mathcal{F}[\delta(t)] = 1$

Theorem 2.4.[3,4] The Fourier transforms for some functions are following

I. $\mathcal{F}[1] = 2\pi\delta(w)$
II. $\mathcal{F}[t^n] = 2\pi i^n \delta^{(n)}(w)$
III. $\mathcal{F}[t^n f(t)] = i^n \frac{d^n \mathcal{F}[f(t)]}{dw^n}$
IV. $\mathcal{F}\left[e^{iw_0 t}\right] = 2\pi\delta(w - w_0)$.
V. If $\mathcal{F}[f(t)] = F(w)$, then $\mathcal{F}\left[e^{iw_0 t} f(t)\right] = F(w - w_0)$
VI. $\mathcal{F}[e^{at}] = 2\pi\delta(w + ia)$
VII. If $\mathcal{F}[f(t)] = F(w)$, then $\mathcal{F}[e^{at} f(t)] = F(w + ia)$
VIII. If $\mathcal{F}[f(t)] = F(w)$, then $\mathcal{F}[f(t - t_0)] = e^{-iwt_0} F(w)$

Theorem 2.5. If Fourier transform of $f(t)$ is $F(w)$ then

a. $\int_{-\infty}^{t} f(u)du = -i\mathcal{F}^{-1}\left[\frac{F(w)}{w}\right]$

b. $\int_{-\infty}^{u} F(u)du = i\mathcal{F}\left[\frac{f(t)}{t}\right]$

To prove a. we use the definition of the inverse Fourier transform

$$f(t) = \frac{1}{2\pi}\int_{-\infty}^{\infty} F(w)e^{iwt}dw$$

By taking integral on both sides from $-\infty$ to t, we have

$$\int_{-\infty}^{t} f(u)\,du = \frac{1}{2\pi}\int_{-\infty}^{\infty} F(w)\frac{e^{iwt}}{iw}dw = -i\mathcal{F}^{-1}\left[\frac{F(w)}{w}\right]$$

To prove b. we use the definition of the Fourier transform

$$F(w) = \int_{-\infty}^{\infty} f(t)e^{-iwt}dt$$

By taking integral on both sides from $-\infty$ to w, we obtain

$$\int\limits_{-\infty}^{w} F(s)\,ds = \int_{-\infty}^{\infty} f(t)\left(\int\limits_{-\infty}^{w} e^{-iut}\,du\right)dt = i\int_{-\infty}^{\infty}\frac{f(t)}{t}.e^{-iwt}dt = i\mathcal{F}\left[\frac{f(t)}{t}\right]$$

Theorem2.6. Let $w > 0$, then

a. $\mathcal{F}\left[\frac{1}{t}\right] = -2\pi i H(w)$

b. $\mathcal{F}\left[\frac{1}{t^2}\right] = -2\pi w$

c. $\mathcal{F}\left[\frac{1}{t^3}\right] = \pi i w^2$

d. $\mathcal{F}\left[\frac{1}{t^4}\right] = \pi \frac{w^3}{3}$

e. $\mathcal{F}\left[\frac{1}{t^5}\right] = -\pi i \frac{w^4}{12}$

f. $\mathcal{F}[lnt] = -2\pi \frac{H(w)}{w}$

Proof a: $\mathcal{F}\left[\frac{1}{t}\right] = \frac{1}{i}\int_{-\infty}^{w} \mathcal{F}(1)du = -i\int_{-\infty}^{w} 2\pi\delta(u)du = -2\pi i H(w)$

Proof b: $\mathcal{F}\left[\frac{1}{t^2}\right] = -i\int_{-\infty}^{w} \mathcal{F}\left(\frac{1}{t}\right)du = -i\int_{-\infty}^{w} -2\pi i H(u)du \quad = -2\pi w$

Proof c: $\mathcal{F}\left[\frac{1}{t^3}\right] = -i\int_{-\infty}^{w} \mathcal{F}\left(\frac{1}{t^2}\right)du = -i\int_{-\infty}^{w} -2\pi u du = \pi i w^2$

Proof f: We know that $\mathcal{F}[f'(t)] = iw\mathcal{F}[f(t)]$, and $(lnt)' = \frac{1}{t}$

We have $\mathcal{F}\left[\frac{1}{t}\right] = iw\mathcal{F}[lnt]$

Then we have $\mathcal{F}[lnt] = \frac{1}{iw}\mathcal{F}\left[\frac{1}{t}\right] = \frac{-2\pi H(w)}{w}$

Moreover this theorem can be seen with other way.

By using Theorems 2.5. a, 2.6. a, we have

$$\mathcal{F}^{-1}[H(w)] = \frac{1}{-2\pi i t}$$

$$\mathcal{F}^{-1}\left[\frac{H(w)}{w}\right] = \frac{i}{-2\pi i}\int_{-\infty}^{t} \frac{1}{u}du = \frac{lnt}{-2\pi}$$

Thus

$$\mathcal{F}[lnt] = -2\pi\frac{H(w)}{w}$$

Theorem2.7. $\mathcal{F}^{-1}\left[\frac{H(w)}{w^2}\right] = \frac{1}{2\pi i}(tlnt - t)$

Proof: $\mathcal{F}^{-1}\left[\frac{H(w)}{w^2}\right] = \frac{1}{-i}\int_{-\infty}^{t} \mathcal{F}\left[\frac{H(w)}{w}\right]du = \frac{1}{-i}\int_{-\infty}^{t} \frac{lnu}{-2\pi}du = \frac{1}{2\pi i}(tlnt - t)$

3. Examples of Applying The Fourier Transform on Differential Equations:

In this section five examples are given and exact solution is found using FTM.

Example 3.1: Let's consider the following ordinary differential difference equation

$$y'(x) + y(x-1) = x^2 + 1. \tag{6}$$

Solution. By taking Fourier transform to Eq (6), we get

$$\mathcal{F}\big(y'(x)+y(x-1)\big)=\mathcal{F}(x^2+1)$$

$$\big(iw+e^{-iw}\big)Y=2\pi i^2\delta''(w)+2\pi\delta(w)$$

$$Y=\frac{-2\pi\delta''(w)+2\pi\delta(w)}{iw+e^{-iw}}.$$

By taking the inverse Fourier Transform of the above equation, we obtain the solution $y(x)$.

$$y=\mathcal{F}^{-1}\left(\frac{-2\pi\delta''(w)+2\pi\delta(w)}{iw+e^{-iw}}\right)$$

$$=\int_{-\infty}^{\infty}\frac{-\delta''(w)}{iw+e^{-iw}}e^{iwx}\,dw+\int_{-\infty}^{\infty}\frac{\delta(w)}{iw+e^{-iw}}e^{iwx}\,dw$$

$$=-2\int_{-\infty}^{\infty}\frac{\delta(w)}{w^2(iw+e^{-iw})}e^{iwx}\,dw+1$$

$$=-2\,\frac{1}{2!}\frac{d^2}{dw^2}\left(\frac{e^{iwx}}{iw+e^{-iw}}\right)|_{w=0}+1=x^2.$$

Example 3.2: Let find a special solution of the following ordinary differential equation with variable coefficients

$$xy''-(2x+1)y'+(x+1)y=x^2e^x. \qquad (7)$$

Solution. By taking Fourier transform to Eq (7), we get

$$\mathcal{F}(xy''-(2x+1)y'+(x+1)y)=\mathcal{F}(x^2e^x).$$

Therefore

$$\mathcal{F}(xy'')-2\mathcal{F}(xy')-\mathcal{F}(y')+\mathcal{F}(xy)+\mathcal{F}(y)=\mathcal{F}(x^2e^x).$$

$$i\frac{d}{dw}(-w^2Y)-2i\frac{d}{dw}(iwY)-iwY+i\frac{dY}{dw}+Y=-2\pi\delta''(w+i)$$

$$-2iwY-iw^2Y'+2Y+2wY'-iwY+iY'+Y=-2\pi\delta''(w+i)$$

$$(-iw^2+2w+i)Y'+(3-3iw)Y=-2\pi\delta''(w+i)$$

$$Y'+\frac{3(1-iw)}{-i(w+i)^2}Y=\frac{2\pi\delta''(w+i)}{i(w+i)^2}.$$

The previous equation is a linear differential equation of first order.

$$\lambda = e^{\int \frac{3(1-iw)}{-i(w+i)^2} dw} = e^{\int \frac{3}{w+i} dw} = (w+i)^3$$

$$((w+i)^3 Y)' = \frac{2\pi}{i}(w+i)\delta''(w+i)$$

$$((w+i)^3 Y)' = \frac{4\pi}{i}(w+i)\frac{\delta(w+i)}{(w+i)^2} = -4\pi i \frac{\delta(w+i)}{(w+i)} = 4\pi i \delta'(w+i).$$

Therefore

$$((w+i)^3 Y)' = 4\pi i \delta'(w+i).$$

By taking integral to the above equation, we have

$$(w+i)^3 Y = 4\pi i \delta(w+i)$$

$$Y = \frac{4\pi i \delta(w+i)}{(w+i)^3}.$$

By taking the inverse Fourier Transform of the above equation, we obtain the solution $y(x)$.

$$y = \mathcal{F}^{-1}(Y) = \mathcal{F}^{-1}\left(\frac{-4\pi i \delta(w+i)}{(w+i)^3}\right) = 2i\int_{-\infty}^{\infty} \frac{\delta(w+i)}{(w+i)^3} e^{iwx} dw = 2i\frac{(ix)^3}{6}e^x$$

$$= \frac{x^3}{3}e^x.$$

Example 3.3: Let's consider the following ordinary differential equation

$$y'' - 2y' + y = \frac{e^x}{x^5}. \tag{7}$$

Solution. By taking Fourier transform to Eq (7), we get

$$\mathcal{F}(y'' - 2y' + y) = \mathcal{F}\left(\frac{e^x}{x^5}\right).$$

Therefore

$$\mathcal{F}(y'') - 2\mathcal{F}(y') + \mathcal{F}(y) = \mathcal{F}\left(\frac{e^x}{x^5}\right)$$

$$(-w^2 - 2iw + 1)Y = -\pi i \frac{(w+i)^4}{12}$$

$$Y = \pi i \frac{(w+i)^2}{12}.$$

By taking the inverse Fourier Transform of the above equation, we obtain the solution $y(x)$.

$$y = \mathcal{F}^{-1}(Y) = \mathcal{F}^{-1}\left(\pi i \frac{(w+i)^2}{12}\right) = \frac{i}{2}\int_{-\infty}^{\infty} \frac{(w+i)^2}{12} e^{iwx} dw = \frac{2\pi i}{2}\frac{1}{\pi i}\frac{1}{12}\frac{e^x}{x^3} = \frac{e^x}{12x^3}.$$

Example 3.4: Let find a special solution of the following ordinary differential equation with variable coefficients

$$(1-x)y'' + xy' - y = 2(x-1)^2 e^{-x}. \tag{8}$$

Solution. By taking Fourier transform to Eq (8), we get

$$\mathcal{F}(y'' - xy'' + xy' - y) = 2\mathcal{F}((x-1)^2 e^{-x})$$

$$(iw)^2 Y - i(-w^2 Y)' + i(iwY)' - Y = -4\pi e^{-i(w-i)}\delta''(w-i)$$

$$-w^2 Y + iw^2 Y' + 2iwY - Y - wY' - Y = -4\pi e^{-i(w-i)}\delta''(w-i)$$

$$(iw^2 - w)Y' + (-w^2 + 2iw - 2)Y = -4\pi e^{-i(w-i)}\delta''(w-i)$$

$$Y' + \frac{-w^2 + 2iw - 2}{iw^2 - w}Y = \frac{-4\pi e^{-i(w-i)}\delta''(w-i)}{iw^2 - w}$$

$$\lambda = e^{\int \frac{-w^2+2iw-2}{iw^2-w}dw} = e^{\int\left(i+\frac{2}{w}+\frac{1}{w+i}\right)dw} = w^2(w+i)e^{iw}$$

$$\left(w^2(w+i)e^{iw}Y\right)' = \frac{-4\pi e^{-i(w-i)}\delta''(w-i)}{iw^2 - w}w^2(w+i)e^{iw} = 4\pi i e^{-1} w\delta''(w-i)$$

$$w^2(w+i)e^{iw}Y = 4\pi i e^{-1}\int w\delta''(w-i)dw = 4\pi i e^{-1}\big(w\delta'(w-i) - \delta(w-i)\big)$$

$$Y = \frac{4\pi i e^{-1}\big(w\delta'(w-i) - \delta(w-i)\big)}{w^2(w+i)e^{iw}}.$$

By taking the inverse Fourier Transform of the above equation, we obtain the solution $y(x)$.

$$y = 2ie^{-1}\int_{-\infty}^{\infty} \frac{\big(w\delta'(w-i) - \delta(w-i)\big)}{w^2(w+i)e^{iw}} e^{iwx} dw$$

$$= 2ie^{-1}\int_{-\infty}^{\infty} \frac{w\delta'(w-i)}{w^2(w+i)} e^{iw(x-1)} dw - 2ie^{-1}\int_{-\infty}^{\infty} \frac{\delta(w-i)}{w^2(w+i)} e^{iw(x-1)} dw$$

$$= -2ie^{-1}\frac{d}{dw}\left(\frac{e^{iw(x-1)}}{w(w+i)}\right)\Big|_{w=i} - 2ie^{-1}\frac{e^{1-x}}{i^2 2i}$$

$$y = -\left(x + \frac{1}{2}\right)e^{-x} + e^{-x} = \left(\frac{1}{2} - x\right)e^{-x}.$$

Example 3.5: Let's consider the following ordinary differential difference equation

$$(1-x)y'' + xy' - y = 2(x-1)^2 e^{-x}. \tag{9}$$

Solution. By taking Fourier transform to Eq (9), we get

$$\mathcal{F}\big(y''(x)+y(x-2)\big)=\mathcal{F}(-x^2+2\ )$$

$$\left(e^{-2iw}-w^2\right)Y=-2\pi i^2\delta''(w)+4\pi\delta(w)$$

$$Y=\frac{2\pi\delta''(w)+4\pi\delta(w)}{e^{-2iw}-w^2}.$$

By taking the inverse Fourier Transform of the above equation, we obtain the solution $y(x)$.

$$y=\mathcal{F}^{-1}\left(\frac{2\pi\delta''(w)+4\pi\delta(w)}{e^{-2iw}-w^2}\right)$$

$$=\int_{-\infty}^{\infty}\frac{\delta''(w)}{e^{-2iw}-w^2}e^{iwx}\,dw+2\int_{-\infty}^{\infty}\frac{\delta(w)}{e^{-2iw}-w^2}e^{iwx}\,dw$$

$$=2\int_{-\infty}^{\infty}\frac{\delta(w)}{w^2(e^{-2iw}-w^2)}e^{iwx}\,dw+2$$

$$=2\,\frac{1}{2!}\frac{d^2}{dw^2}\left(\frac{e^{iwx}}{e^{-2iw}-w^2}\right)|_{w=0}+2=-4x-x^2.$$

4. Conclusion

In conclusion, delving into the realm of solutions for differential-differential difference equations with variable coefficients through the application of the Fourier Transform Method unveils a powerful and versatile approach. The Fourier Transform's ability to seamlessly navigate between the time and frequency domains provides a unique lens through which these complex equations can be unraveled. By transforming the differential-differential difference equations into simpler algebraic expressions in the frequency domain, we gain valuable insights into the system's behavior and characteristics. This method not only simplifies the mathematical complexities but also opens doors to a wide array of analytical tools that facilitate the exploration of solutions. Moreover, the Fourier Transform method shines particularly bright when faced with problems featuring variable coefficients. Its adaptability to changes in coefficients allows for dynamic and nuanced analysis of systems that may exhibit variations over time. This adaptability is crucial in capturing the intricate dynamics of real-world phenomena where coefficients are seldom constant. Also in future studies, we can solve partial differential difference equations and integro differential difference equations using this method.

Authorship contribution statement

M. Düz: Methodology, Investigation, Review and Editing, Formal Analysis; **S. Avezov**: Validation, Formal Analysis, Original Draft Writing; **A. Issa**: Review and Editing, Formal Analysis, Methodology, Original Draft Writing, Validation.

Acknowledgment

As the authors of this study, we declare that we do not have any support and thank you statement.

Conflict of Interest

The authors declare that they have no known competing financial interests or personal relationships that could have appeared to influence the work reported in this paper.

Ethics Committee Approval and Informed Consent

As the authors of this study, we declare that we do not have any ethics committee approval and/or informed consent statement.

References

[1] T. M. Elzaki and S. M. Elzaki, “On the Elzaki transform and ordinary differential equation with variable coefficients”, *Advances in Theoretical and Applied Mathematics*, 6(1), 41-46, 2011.

[2] S. Aggarwal, N. Sharma, R. Chauhan, A. R. Gupta and A. Khandelwal, “A new application of Mahgoub transform for solving linear ordinary differential equations with variable coefficients”, *Journal of Computer and Mathematical Sciences,* 9(6), 520-525, 2018.

[3] M. Düz, A. Issa and S. Avezov, “A new computational technique for Fourier transforms by using the Differential transformation method”, *Bulletin of International Mathematical Virtual Institute,* 12(2), 287-295, 2022.

[4] Osgood, “The Fourier transform and its applications”, Lecture notes for EE, 261, 2009, pp. 20.

[5] N. Wheeler, Simplified Production of Dirac Delta Function Identities, Reed College, 1997.

[6] M. Sezer and A. Akyüz-Daşcıoğlu, “Taylor polynomial solutions of general linear differential–difference equations with variable coefficients”, *Applied Mathematics and Computation,* 174(2), 1526-1538, 2006.

[7] K.L. Cooke, “Differential Difference Equations”, New York, Academic Press, 1963.

[8] A. Arikoglu and I. Ozkol, “Solution of differential–difference equations by using differential transform method”, *Applied Mathematics and Computation,* 181(1), 153-162, 2006.

[9] J. K. Zhou, “Differential Transformation and Its Applications for Electrical Circuits”, Wuhan, Huazhong University Press, 1986.

[10] L. Zou, Z. Wang and Z. Zong, “Generalized differential transform method to differential-difference equation”, *Physics Letters A,* 373(45), 4142-4151, 2009.

Süleyman Demirel Üniversitesi Fen Edebiyat Fakültesi Fen Dergisi https://dergipark.org.tr/sdufeffd
Süleyman Demirel University Faculty of Arts and Sciences Journal of Science e-ISSN: 1306-7575
Research Article, 2023, 18(3): 268-275, DOI: 10.29233/sdufeffd.1251876

A Photo-transfer Thermoluminescence (PTTL) Study of TLD-100 over a Wide Dose Range

Engin Aşlar[1,*]

[1]Institute of Nuclear Sciences, Ankara University, 06100, Ankara, TURKEY
https://orcid.org/0000-0002-1414-0317
*corresponding author: easlar@ankara.edu.tr

(Received: 17.02.2023, Accepted: 13.11.2023, Published: 23.11.2023)

Abstract: Photo-transferred thermoluminescence (PTTL) is defined as the transfer of electrons from deep traps into shallow traps via optical stimulation. The importance of PTTL is that it allows for a second measurement of dose assessments for accuracy in cases such as an erroneous dose evaluation. In this study, the PTTL signal of TLD-100 was investigated in detail for a wide dose range from mGy to Gy. The investigation of PTTL signals in the order of Gy is the main innovation of this study. Based on the results of the low dose measurement (mGy), the PTTL dose-response curve has a significant sublinear characteristic in the order of mGy for the total area condition. Additionally, PTTL signals could not be distinguished from the background signal up to 5mGy. Therefore, the PTTL method can be used by taking into account the sublinear function obtained after 5mGy for the total area. On the other hand, it can be applied to TLD-100 between 0.5mGy and 50mGy using ROI. Based on the high dose measurement results (Gy), the PTTL method can be applied up to 10Gy regardless of the total area and ROI. Therefore, the dose reassessment can be performed with PTTL signal in high dose measurements (Gy) such as in the radiotherapy field. Furthermore, in future studies, heating the dosimeters during UV exposure, predose effect, or subjecting the dosimeters to fast cooling following the annealing process may provide important outputs to obtaining higher PTTL intensity, thus, it may allow measuring lower radiation doses.

Key words: Photo-transfer, PTTL, TLD-100, LiF:Mg,Ti

1. Introduction

The photo-transferred thermoluminescence (PTTL) phenomenon is described as the transfer of electrons by light from deep electron traps to shallower electron traps already depleted. The glow curve obtained by heating the material to a certain temperature, followed by exposure to light of a certain wavelength for a period of time, causes the regeneration of the TL glow curve [1-4]. Although the thermoluminescence (TL) phenomenon is known to be irreversible, it is possible to reassess doses thanks to the PTTL method, since not all traps in the material are emptied [5]. The TL peaks obtained depend on the power of the light source, wavelength, and illumination duration [6]. PTTL has been seen in both natural and artificial materials, this makes the PTTL a useful tool for dosimetry and dating applications [7]. Especially in personal dosimetry, it may be necessary to re-evaluate the dose and control the accuracy of the measurement. In this case, the use of the PTTL method is of critical importance [8,9].

TLD-100 (LiF:Mg,Ti) has important features in radiation dosimetry such as tissue equivalent, low energy response, and linear dose-response over a wide dose range [10].

The PTTL behavior of TLD-100 has been investigated by various researchers for a long time [5,8,9,11-20]. Initial studies performed with TLD-100 have shown that dose reassessment with PTTL is possible for doses higher than 10mGy [11]. Mukherjee and Duftschmid [12] showed that doses of up to 2mGy can be recalculated using a 30W UV lamp with TLD card dosimeters. Apart from these studies, Delgado et al. [5], by designing a simple and effective UV irradiator, it was determined that doses in the range of 0.2mGy could be determined by PTTL. It has been reported that the method can be routinely applied for re-assessment of the doses. According to the study carried out by Budzanowski et al. [9], the PTTL behavior of the TLD-100 was investigated throughout the dose range between 5 and 50mGy. The PTTL properties of TLD-100 were also investigated by Ben-Shachar [14]. According to this study, the doses can be re-evaluated with dosimeters between 5 and 100mGy for TLD-100. In addition, it has been reported that the PTTL signal intensity can be increased by heating the samples during UV exposure and by pre-dose sensitized dosimeters [5,15]. A similar study has been performed in recent years by Wrzesień et al. [16]. In this study, PTTL properties of TLD-100 were investigated between 100 and 1000mGy.

PTTL studies of TLD-100 have been performed mostly in the personnel dosimetry dose range (order of mGy) in the literature. It was seen that studies on the behavior of the PTTL signal at high dose values (Gy) were inadequate when the literature was examined. In the present study, PTTL signals were investigated both in the order of mGy and Gy. In this context, the investigation of PTTL signals in the order of Gy is the main innovation of this study. The results obtained in the order of Gy may provide important contributions and new perspectives to high-dose dosimetry area for dose evaluation with PTTL signal, especially in the field of radiotherapy. Secondly, when the literature is examined, the dose values used in the order of mGy are in a very limited range, but in the present study, the dose values are selected over a wide range.

The purpose of this study is to investigate the PTTL signal behavior of TLD-100 in a wide range of doses, starting from the lowest possible dose (0.1mGy) up to 100 Gy. PTTL behavior, especially at high doses, is one of the main aims of this study. Both TL and PTTL dose-response curves were established for TLD-100. In addition, the UV sensitivity of TLD-100 was studied at different UV exposure durations.

2. Material and Method

2.1. Material

The LiF:Mg,Ti (TLD-100) chip dosimeters with dimensions of 3.2×3.2×0.9 mm^3 were used in the study. The $^{90}Sr/^{90}Y$ beta source was used as irradiation source. The Harshaw TLD Model 2210 Chip Irradiator a dose rate of 0.92μGy/s was used for low dose (mGy) measurement. For high dose (Gy) measurement, the internal $^{90}Sr/^{90}Y$ beta source in the Risø TL/OSL reader with a dose rate of 0.11 Gy/s was used. TL measurements were performed with Harshaw TLD-3500 equipped with a normal glass filter. A programmable Thermo Theldo furnace was used for the preheat and annealing of the dosimeters. For UV exposure, a 15 Watt UVC TUV/G15 T8 model Philips brand UV lamp with a wavelength of 254nm and a power of 0.15 W×m^2 at 7 cm was used.

2.2. Method

The dosimeters were calibrated according to both dose values (mGy and Gy). For this purpose, the irradiations were performed at 10mGy in low-dose measurements and 1Gy in high-dose measurements. Element correction coefficients (ECC) were assigned to the dosimeters separately for each type of measurement in the order of mGy and Gy. Forty dosimeters were used throughout the study, having a standard deviation of around %5. The final TL intensity was obtained by multiplying the intensity values obtained from the TL reader by the predetermined ECC factors.

The measurement protocol for PTTL measurements was given in Table 1. RT refers to the room temperature in Table 1. This protocol was the same given in the study by Budzanowski et al. [9]. The dosimeters were placed in the center at a distance of 7 cm from the UV lamp. All measurements were performed using three dosimeters. The error bars in the figures describe the standard deviation over the three dosimeters.

The total area value was determined as the area under the glow curve, while the Region of Interest (ROI) was obtained over three peaks in the dosimetric peak region (Channels: between 110 and 160). The total area value was generally used in the order of Gy measurements. The parts where the ROI was used were indicated in the text.

Table 1. PTTL measurement protocol

Steps	Measurements	Process
1	Annealing of the dosimeters	1 hour at 400°C followed 2 hour at 100°C
2	Irradiation of the dosimeters	mGy to Gy
3	Preheat of the dosimeters	10 min at 100°C
4	TL measurement	RT to 300°C (Heating rate=5°C/s)
5	UV exposure	15 min at room temperature
6	Preheat of the dosimeters	10 min at 100°C
7	PTTL measurement	RT to 300°C (Heating rate=5°C/s)

Two different dose range was studied for dose-response: First, dosimeters were irradiated in the order of mGy at 0.1, 0.5, 1, 5, 10, 15, 20, 30, 40 and 50mGy. Secondly, irradiation doses were chosen as 0.10, 0.25, 0.50, 0.75, 1, 10 and 100Gy in the order of Gy. A pinhole was used in the first TL measurement (Step 4 in Table 1) for 100Gy in front of the glass filter in the TLD reader to prevent the possible saturation of the photomultiplier tube, decreasing the TL intensity by about 80%.

3. Results

3.1. Optimum UV exposure duration

Figure 1 shows the variation of PTTL signal intensity obtained according to different UV exposure durations. The figure was constructed using both total area and ROI. In both cases, the PTTL signal intensity showed the same behavior according to the UV exposure duration. The PTTL signal intensity increased from 5 to 15 min with UV exposure, then started to decrease, and finally, it showed an almost stable behavior after 120 min. The highest PTTL signal intensity was obtained after 15 min of UV exposure. Therefore, 15 min of UV exposure was adopted throughout the study to build the PTTL signal.

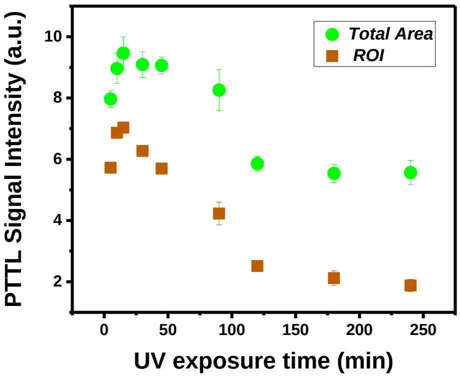

Figure 1. PTTL signal intensity obtained versus different UV exposure durations

The behavior of PTTL intensity with UV exposure time obtained in this study showed a similar pattern with the Alzahrani et al. [6] and Budzanowski et al. [9] although the optimum UV exposure time obtained in these studies differs due to reasons such as different power of the lamp and difference in distance of sample and lamp.

3.2. Glow curves (TL and PTTL)

Figures 2a and b show the TL and PTTL glow curves in the same figures obtained for 20mGy and 1Gy, respectively. According to Figure 2a, the TL intensity was almost eight times bigger than the PTTL intensity when taking into consideration peak maximum intensity (known as peak 5). The maximum temperature difference of the main peak in the TL and PTTL glow curves was ~6°C. Similar difference was also seen in Budzanowski et al. [9]. This temperature difference can be originated from factors such as the temperature changes in the heated dosimeter and the planchet material cannot be fully distinguished, and the differences in the temperature sensitivity in the thermocouple system. Therefore, it can be accepted that TL and PTTL peaks appear at the same temperatures. As for the 1Gy, again TL intensity was eight times bigger than the PTTL intensity according to peak maximum intensity (Figure 2b). The temperature difference of the main peak between TL and PTTL was the same as ~6°C.

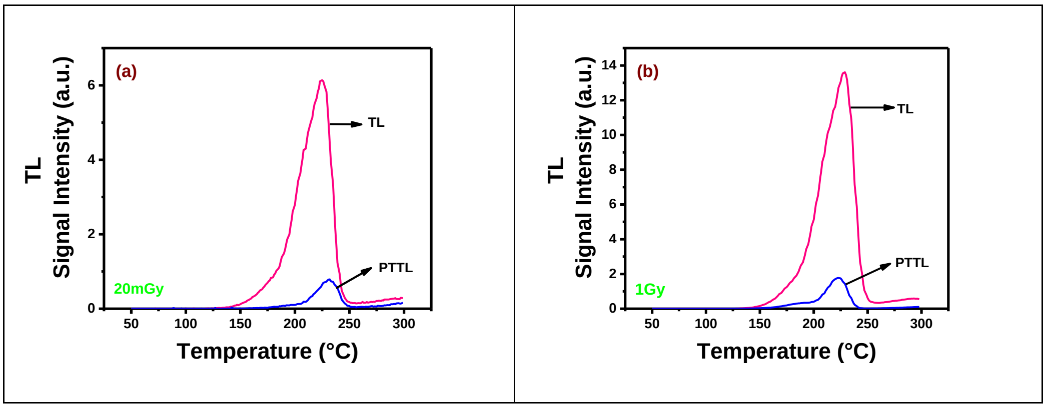

Figure 2. TL and PTTL glow curves obtained according to different radiation doses: a) 20mGy; b) 1Gy

The ratio of PTTL intensity to TL intensity varied between (10-12)% according to both ROI and total area for the doses between 10 and 50mGy. On the other hand, this ratio varied between (15-45)% for ROI and (20 – 85)% for the total area at doses between 0.5 and 5mGy. The PTTL intensity obtained at 0.1mGy was greater than the TL intensity contrary to expectations, both in terms of ROI and total area. Therefore, reassessment of doses with the PTTL method for 0.1mGy was not possible under these conditions. Furthermore, TL peaks were not evident in the PTTL glow curves at doses between 0.1

and 1mGy considering the total area. However, the PTTL peaks became distinguishable for these dose ranges in the case of ROI. The ratio of PTTL intensity to TL intensity in the order of Gy varied as (10-12)% for all doses between 0.1 and 100Gy. This ratio did not change according to ROI either. Budzanowski et al. [9] reported that the ratio of PTTL intensity to TL intensity reached 17% in their study. Similarly, Wrzesień et al. [16] obtained this ratio as 19%. These results are almost compatible with our study. The slightly higher value seen in both Budzanowski et al. [9] and Wrzesień et al. [16] is due to the increased PTTL efficiency as a result of heating the dosimeters at the same time during UV exposure.

3.3. UV sensitivity

Figure 3 shows the TL signal intensity obtained from UV exposed dosimeters ranging from 5 to 120 minutes for annealed dosimeters. Dashed lines show the mean value of all data. In order to understand the UV sensitivity of TLD-100, both the area values under the glow curve and the formation of the TL glow curve were investigated. The area values obtained after direct UV exposure for annealed dosimeters showed different behavior during the 5 to 15 min UV exposure according to ROI and the total area. In the case of ROI, the UV sensitivity obtained from the TLD-100 in general was quite low even though the intensity at low UV exposures showed an increasing trend. However, a significant peak structure could not be seen in the glow curve. The maximum deviation from the mean was around 13% in the case of total area, while it was around 33% for the ROI. The high deviation in the ROI situation was due to an increase seen in the first three UV durations. No regular increase or decrease in intensity was observed for the total area. Similar to ROI condition, no notable TL glow curve was observed in the total area condition. As a result, TLD-100 did not show UV sensitivity with respect to both ROI and total area.

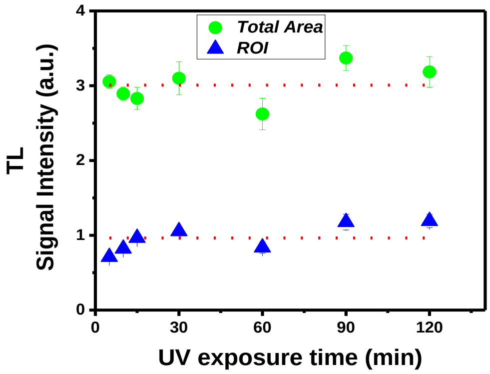

Figure 3. TL signal intensity obtained following different UV exposure durations

According to a study performed by Mason et al. [21], the UV sensitivity of TLD-100, TLD-200 and TLD-300 has been reported as low. The UV sensitivity of the dosimeters was compatible with those obtained by both Ben-Shachar et al. [14] and Mason et al. [21].

3.4. Dose-response curve (TL and PTTL)

Figures 4a and b show the TL and PTTL signal intensity obtained doses between 0.1mGy and 50mGy, respectively in the log-log scale. Figure 4a was constructed according to the total area, while Figure 4b was constructed according to both total area and ROI. Dose-response curves were fitted to the function of $y=a\times D^b$ where the D is applied dose, a is the constant and b is the linearity coefficient. In this equation, if b equals 1, a curve is linear, if $b<1$ or $b>1$, the curve shows sublinear and supralinear behavior, respectively [22,23]. According to Figure 4a, the TL signal intensity showed sublinear behavior with *b* equal to 0.92±0.02. However, this value can be considered linear as *b* is close to 1.00. On the other hand, Figure 4b shows different dose-response characteristics depending on the total area and ROI. PTTL signal intensity has prominently sublinear characteristics by *b* equal to 0.41±0.08 for the total area condition. As for the ROI, it showed a slightly sublinear behavior similar to Figure 4a by *b* equal to 0.84 ±0.02. It can be said that the use of ROI increases its linearity.

According to studies conducted by [11-14], PTTL dose-response curves in the mGy order have been reported to show linear behavior. However, the linearity of the dose-response curves was not investigated with any fit function, it was interpreted only visually. In the present study, the PTTL signal generally increases as the dose increases for both mGy and Gy order. In this sense, the data obtained are compatible with the literature [11-14]. When the linearity of the curves was examined comprehensively, a serious sublinearity appeared in the case of the total area case in the order of mGy. Therefore, attention should be paid to the sublinearity of the dose-response function when determining the dose with the PTTL signal in the mGy order according to the total area. As a result, the PTTL signal obtained at between 0.1 and 1mGy cannot be used since the peaks cannot be distinguished from the background signal for the total area. Therefore, dose evaluation with PTTL can be used after 5mGy. On the other hand, in the case of ROI, it is possible to re-evaluate doses with the PTTL signal at dose values between 0.5 and 50 mGy.

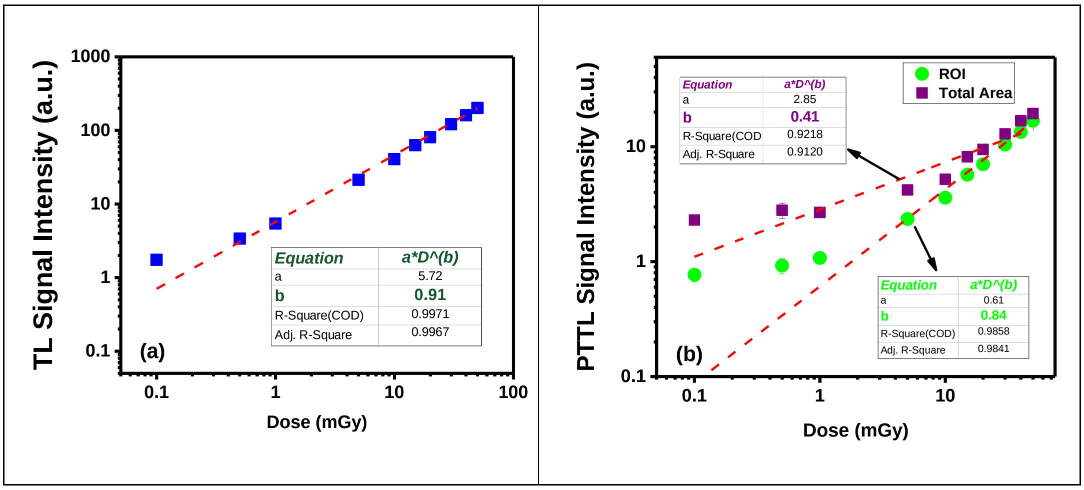

Figure 4. Dose-response curves obtained for the order of mGy: a) TL signal intensity, b) PTTL signal intensity

Figures 5a and b show the TL and PTTL intensity obtained between 0.1 and 100 Gy in the log-log scale. The correction was applied to the last data (100Gy) due to the pinhole reducing the intensity. Both TL and PTTL intensities increased with increasing dose values.

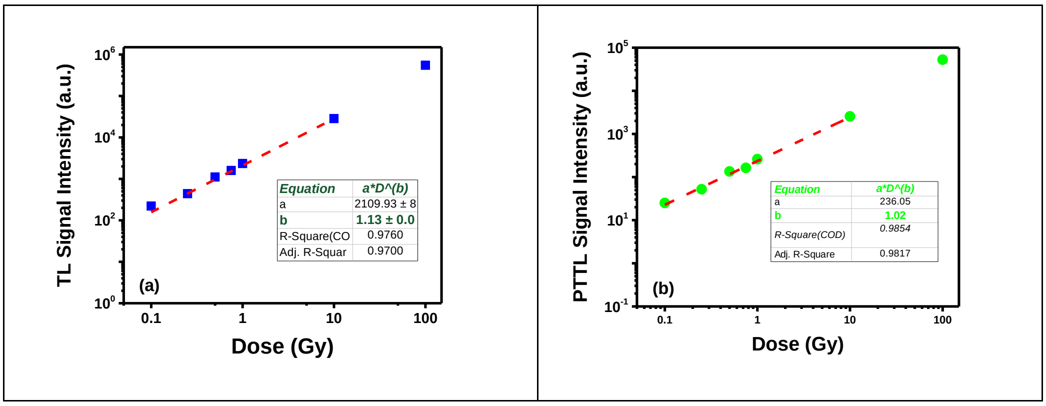

Figure 5. Dose-response curves obtained for order of Gy: a) TL signal intensity, b) PTTL signal intensity

According to Figure 5a, the TL signal intensity showed slight supralinear behaviour by *b* equal to 1.13 ±0.03 in the dose ranges between 0.1 and 10Gy. After 10Gy, the supralinearity increases further. In Figure 5b, the PTTL signal showed a linear response with *b* equal to 1.02 ±0.02 and started to deviate from linearity after 10 Gy. Based on the results for the order of Gy, the PTTL method allows re-assessment of doses up to 10Gy.

4. Conclusion

In this study, PTTL signals were investigated in detail both in the order of mGy and Gy. The investigation of PTTL signals in the order of Gy is the main innovation of this study. Based on the results of the low dose measurement (mGy), the PTTL dose-response curve has a significant sublinear characteristic in the order of mGy for the total area. Additionally, PTTL signals could not be distinguished from the background signal up to 5mGy. Therefore, the PTTL method can be used by taking into account the sublinear function after 5mGy for the total area. On the other hand, it can be applied to TLD-100 between 0.5 and 50mGy using ROI. Based on the high dose measurement results (Gy), the PTTL signal can be evaluated up to 10Gy regardless of the total area and ROI. Therefore, the dose reassessment can be performed with PTTL signal in high dose measurements (Gy) such as in the radiotherapy field. With this study, it has been shown that dose reassessment is possible with a PTTL signal in the order of Gy. Furthermore, in future studies, heating the dosimeters during UV exposure, predose effect, or subjecting the dosimeters to fast cooling following the annealing process may provide important outputs to obtaining higher PTTL intensity, thus, it may allow measuring lower radiation doses.

Authorship contribution statement

Engin Aşlar: Conceptualization, Methodology, Investigation, Review and Editing, Original Draft Writing, Visualization

Declaration of competing interest

The authors declare that they have no known competing financial interests or personal relationships that could have appeared to influence the work reported in this paper.

Ethics Committee Approval and/or Informed Consent Information

As the authors of this study, we declare that we do not have any ethics committee approval and/or informed consent statement.

References

[1] M. A. Periard and R. P. Bradley, "Dose re-estimation of personal dosimeters using the technique of phototransferred thermoluminscence", *Radiation Protection Dosimetry*, 6(1–4), 273–276, 1984.

[2] J. L. Muñiz, V. Correcher and A. Delgado, "PTTL dose re-estimation applied to quality control in tld-100 based personal dosimetry", *Radiation Protection Dosimetry*, 85, 63–66, 1990.

[3] C. S. Alexander and S. W. S. McKeever, "Phototransferred thermoluminescence", *Journal of Physics D: Applied Physics*, 31(20), 2908, 1998.

[4] M. L. Chithambo, P. Niyonzima and J. M. Kalita, "Phototransferred thermoluminescence of synthetic quartz: analysis of illumination-time response curves", *Journal of Luminescence*, 198, 146-154, 2018.

[5] A. Delgado, V. Unamuno, J. L. Muñiz, V. Correcher and J. M. Gómez Ros, “A simple UV irradiator for low dose reassessment with LiF TLD-100”, *Radiation Protection Dosimetry*, 67(4), 303-306, 1996.

[6] J. S. Alzahrani, C. Soliman and D. A. A. Alzahrany, “Phototransferred thermoluminescence from obsidian using ultraviolet radiation”, *Journal of Natural Sciences Research*, 6(16), 53-59, 2016.

[7] I. K. Bailiff, S. G. E. Bowman, S. F. Mobbs and M.J. Aitken, “The phototransfer technique and its use in thermoluminescence dating”, *Journal of Electrostatics*, 3(1-3), 269-280, 1977.

[8] S. Miljanić, J. Bibić, S. Blagus, B. Mihaljević and B. Vekić, “Dose reassessment of LiF: Mg, Ti detectors in the mixed fields”, *Radiation Measurements*, 46(12), 1586-1589, 2011.

[9] M. Budzanowski, A. Sas-Bieniarz, P. Bilski, A. Bubak and R. Kopeć, “Dose reassessment by using PTTL method in MTS-N (LiF: Mg, Ti) thermoluminescent detectors”, *Radiation Measurements*, 56, 389-392, 2013.

[10] A. J. J. Bos, “High sensitivity thermoluminescence dosimetry”, *Nuclear Instruments and Methods in Physics Research Section B: Beam Interactions with Materials and Atoms*, 184(1-2), 3-28, 2001.

[11] M. W. Charles, “An extended role for thermoluminescent phosphors in personnel environmental and accident dosimetry using sensitisation, re-estimation and fast fading”, *Nuclear Instruments and Methods in Physics Research*, 206(1-2), 239-242, 1983.

[12] B. Mukherjee and K.E. Duftschmid, “Re-estimation of low level gamma ray doses detected by lithium fluoride thermoluminescence dosemeters”, *Radiation Protection Dosimetry*, 14(1), 41-45, 1986.

[13] B. D. Bhasin, S. P. Kathuria and S. V. Moharil, “Some peculiarities of photo-transfer thermoluminescence in LiF-TLD 100”, *Physica Status Solidi (A)*, 106(1), 271-276, 1988.

[14] B. Ben-Shachar, “Ultraviolet sensitivity and photo-transferred thermoluminescence of the Harshaw and Panasonic used TLDs-a comparison”, *International Journal of Radiation Applications and Instrumentation. Part A. Applied Radiation and Isotopes*, 40(8), 687-690, 1989.

[15] T. M. Piters, E. M. Yoshimura, C. M. Sunta, E. Okuno, N. K. Umisedo and M. P. Diaz, “A comparative study of glow curves in photo-transferred and pre-dose sensitized thermoluminescence (PTTL and TL) in LiF: Mg, Ti”, *Radiation Effects and Defects in Solids*, 136(1-4), 301-306, 1995.

[16] M. Wrzesień, H. Al-Hameed, Ł. Albiniak, J. Maciocha-Stąporek and M. Biegała, “The photo-transferred thermoluminescence phenomenon in case of emergency dose assessment”, *Radiation and Environmental Biophysics*, 59, 331-336, 2020.

[17] A. Delgado, J. G. Roz, J. L. Muñiz and J. C. Portillo, “Application of glow curve analysis methods to improve TLD-100 dose reassessment performance”, *Health Physics*, 62(3), 228-234, 1992.

[18] S. Miljanić, K. Krpan and S. Blagus, “TL and PTTL of TLD-100 and TLD-700 after irradiation with 14.5 MeV neutrons”, *Nuclear Instruments and Methods in Physics Research Section A: Accelerators, Spectrometers, Detectors and Associated Equipment*, 574(3), 510-517, 2007.

[19] A. Abraham, M. Weinstein, U. German and Z. B. Alfassi, “On the reassessment of doses in TL-dosimetry by measuring the residual dose”, *Radiation Protection Dosimetry*, 125(1-4), 113-116, 2007.

[20] A. Sas-Bieniarz, M. Budzanowski, A. Bubak and R. Kopeć, “Application of phototransferred thermoluminescence (PTTL) for dose re-assessment in routine dosimetry using MTS-N (LiF: Mg, Ti) thermoluminescent detectors”, *Radiation Measurements*, 71, 447-450, 2014.

[21] E. W. Mason, “Thermoluminescence response of 7LiF to ultra-violet light”, *Physics in Medicine& Biology*, 16(2), 303, 1971.

[22] A. Halperin and R. Chen, “Thermoluminescence of semiconducting diamonds”, *Physical Review, 148,* 839-845, 1966.

[23] S. V. Nikiforov, V. Pagonis and A. S. Merezhnikov, “Sublinear dose dependence of thermoluminescence as a result of competition between electron and hole trapping centers”, *Radiation Measurements*, 105, 54–61, 2017.

Süleyman Demirel Üniversitesi Fen Edebiyat Fakültesi Fen Dergisi https://dergipark.org.tr/sdufeffd
Süleyman Demirel University Faculty of Arts and Sciences Journal of Science e-ISSN: 1306-7575
Research Article, 2023, 18(3): 276-283, DOI: 10.29233/sdufeffd.1381927

Investigation of the Incorporation of C_{60} into $PC_{61}BM$ to Enhance the Photovoltaic Performance of Inverted-type Perovskite Solar Cells Based on $MAPbI_3$

Mehmet Kazici[1,*]

[1]Department of Electrical & Electronics Engineering, Engineering Faculty, Siirt University, 56100, Siirt, TURKEY
https://orcid.org/0000-0001-9048-7788
*corresponding author: mehmetkazici@siirt.edu.tr

(Received: 27.10.2023, Accepted: 15.11.2023, Published: 23.11.2023)

Abstract: Perovskite Solar Cells (PSCs) have managed to significantly capture attention by achieving efficiency values of 25.6% in a remarkably short period of around ten years. Each layer within the device plays a crucial role in the overall device efficiency when it comes to PSC production. $PC_{61}BM$, a derivative of fullerene, is one of the most commonly used electron-transport layers (ETLs) in inverted-type PSCs. In this study, the improvement of the ETL was aimed by incorporating C_{60} into $PC_{61}BM$, and the effects of the doped ETL on $MAPbI_3$-based inverted-type PSCs were investigated. For inverted type PSCs which are fabricated under high humidity (40-60%) and room conditions (~25 °C), the power conversion efficiencies (PCEs) have boosted from 11.54% (for undoped $PC_{61}BM$) to 13.40% (for C_{60}-doped $PC_{61}BM$). To comprehend the sources of improvement in the fabricated devices, a series of characterizations were carried out, including Current Density-Voltage (J-V), Hysteresis Factor (HF), Scanning Electron Microscope (SEM), and Atomic Force Microscope (AFM) measurements.

Key words: Perovskite solar cells, Fullerene, Electron transport layer

1. Introduction

Perovskite solar cells (PSCs) have achieved a remarkable increase in efficiency, from 3.8% to 25.6%, in a relatively short period of about a decade [1, 2]. PSCs have garnered significant attention from researchers worldwide due to their easy production, high efficiency, and cost-effectiveness. Perovskite materials typically have a chemical structure represented as ABX_3. In the desired semiconductor structure of halide perovskites for photovoltaic applications, ABX_3 consists of: A = cation (such as $CH_3NH_3^+$ and $CH(NH_2)_2^+$), B = divalent metal cation (such as Pb^{2+}), and X = halogen anion (such as Cl^-, Br^- and I^-) [3]. In 2009, Miyasaka and their colleagues discovered that the organic metal halide perovskite materials, Methyl ammonium lead bromide ($MAPbBr_3$) and Methyl ammonium lead iodide ($MAPbI_3$), could absorb sunlight in dye-sensitized solar cells. They achieved an efficiency of 3.8% by using perovskite materials inside liquid electrolytes [1]. However, it was observed that perovskite materials degraded rapidly within liquid electrolytes, leading to research efforts to find more suitable production methods for perovskite. In 2012, using thin-film technology, the first all-solid-state PSCs were fabricated, and device stability was improved, reaching efficiency values of 9.7% [4]. In the same year, Snaith and their colleagues used compact titanium dioxide (TiO_2) as the electron transport layer (ETL) and aluminum oxide (Al_2O_3) as the scaffold material, achieving an efficiency of 10.9% for PSCs by using the perovskite material methyl ammonium lead iodide chloride ($CH_3NH_3PbI_2Cl$) [5]. Recently, all-solid-state single junction PSCs have reached efficiency values of 25.6% [2]. Thin-film layers involved in every stage of fabrication for PSCs are crucial in terms of production cost, stability, and efficiency. In traditional and inverted device architectures of PSCs, the main aim is to transport the charges generated in the absorber layer (perovskite) to the necessary electrodes through charge transport layers. Therefore, charge transport layers play a significant role in the device efficiency. The orientation of the electron-hole (exciton) pairs formed in the absorber layer is the most fundamental difference between traditional and inverted type PSCs. In the traditional architecture, electrons move towards the bottom electrode, whereas in the inverted architecture, they move towards the top electrode. Similarly, in the traditional device architecture, holes move towards the top electrode, while in the inverted structure, holes move towards the bottom electrode. In the PSCs fabricated using traditional device architecture, inorganic oxide materials such as titanium dioxide (TiO_2)[4, 5, 6] and tin (IV) oxide (SnO_2) [7, 8] are commonly used as ETLs. On the other hand, in the inverted device architecture, ETLs often involve fullerene and its derivatives, known for their ultrafast charge transfer properties [9, 10]. The inverted device architecture has gained attention for commercial applications due to its low-temperature production techniques and ease of manufacturability [11]. Phenyl-C_{61}-butyric acid methyl ester ($PC_{61}BM$), a derivative of fullerene, is one of the most commonly used electron transport materials in the inverted type PSCs due to its strong electron transport capabilities and relatively high electron affinity [12]. However, $PC_{61}BM$ can lead to efficiency reduces in the inverted type PSCs due to certain limitations, including low electron mobility, challenges in forming high-quality thin films, current leakage, and excessive nonradiative recombination [10, 13]. To overcome the disadvantages mentioned above, one of the most effective methods is to apply a doping process into $PC_{61}BM$. Kuang and their colleagues enhanced device performance in $CH_3NH_3PbI_{3-x}Cl_x$-based PSCs by introducing a new two-dimensional carbon material called graphdiyne as a dopant into $PC_{61}BM$. This approach enhanced film conductivity and improved the electron transport layer/perovskite interface [14]. Bae and their colleagues boosted the PCE of PSCs by employing n-type 1,3-Dimethyl-2-phenyl-2,3-dihydro-1H-benzoimidazole (DMBI) as a dopant into $PC_{61}BM$. This addition increased the electrical conductivity of the ETL while reducing the work function [15]. Xia and their colleagues enhanced device efficiency by incorporating Oleamide, an amphiphilic surfactant, into $PC_{61}BM$. This modification improved the coverage of ETL on the perovskite surface, increased the flow of the charge to the top electrode, and significantly reduced recombination [16]. Similar doping strategies with $PC_{61}BM$, such as reduced graphene oxide (RGO) [17] , carbon quantum dots [18] , bathocuproine (BCP) [19] and poly[(9,9-dioctyluorene)-2,7-diyl-alt-(4,7-bis(3-hexylthien-5-yl)-2,1,3 benzothiadiazole) -2′,2″-diyl] (F8TBT) [20], have been utilized to enhance the PCEs of PSCs. In 2021, Younes and their colleagues improved device performance and stability for inverted type PSCs by directly doping fullerene (C_{60}) into $PC_{61}BM$, serving as an ETL [21]. In this study, chlorobenzene was used as a solvent for both $PC_{61}BM$ and C_{60} materials, and the research investigated very low concentration ratios of C_{60} within $PC_{61}BM$. The device fabrication involved preparing perovskite ($MAPbI_3$) in dimethyl sulfoxide (DMSO) and gamma-butyrolactone (γ-butyrolactone) solvents, and perovskite and ETLs were deposited in a glove box with low oxygen and humidity conditions. However, it's important to note that commercializing PSCs with device fabrication inside a glove box can be both challenging and costly.

In this present study, PSCs based on $MAPbI_3$ were fabricated using gamma-butyrolactone as a solvent under high humidity conditions (40-60%) and room temperature (~25 °C) for the inverted architecture. The aim was to improve device efficiency by incorporating C_{60} into $PC_{61}BM$ as the electron transport layer. Unlike previous studies, 1,2-dichlorobenzene, which is a good solvent for C_{60}, was specifically used for the electron transport layer, and the amount of $PC_{61}BM$ was reduced, with C_{60} being added in its place. The efficiency of the fabricated PSCs increased from 11.54% (for undoped $PC_{61}BM$) to 13.40% (for C_{60}-doped $PC_{61}BM$), as compared to the reference device.

2. Material and Method

2.1. Device Fabrication

The inverted type PSCs were fabricated with the ITO/PEDOT:PSS/$MAPbI_3$/$PC_{61}BM$ or $PC_{61}BM:C_{60}$ /BCP/Ag device architecture. Indium tin oxide (ITO)-coated glass substrates (Japan, 10-12 ohm/square resistance) were first cleaned by sonication in acetone and isopropanol for 20 minutes each and then dried with nitrogen gas. Before the spin-coating process, the cleaned ITO-coated glass substrates were exposed to oxygen plasma for 10 minutes (Germany, Diener-Femto). As the hole transport layer, PEDOT:PSS (Heraeus, AL4083) was coated onto the ITO-coated glass using the spin-coating method. After the deposition of PEDOT:PSS thin films, a 10-minute annealing process was carried out at 140 °C. The perovskite solution was prepared by mixing PbI_2 (Sigma Aldrich, 1.3 M) and CH_3NH_3I (Lumtec, 1.54 M) materials in 2.5 mL of gamma-butyrolactone (GBL) and stirring on a magnetic stirrer at 50 °C for 24 hours. Prior to coating, the perovskite solution was filtered using a 0.45 µm PTFE filter. Subsequently, the perovskite solution was spin-coated onto the PEDOT:PSS layer at 5000 rpm for 40 seconds. During the last 10 seconds of the spin-coating process, a washing step with 80 µL of toluene was applied as an anti-solvent while coating the perovskite onto the PEDOT:PSS layer. The perovskite films were annealed at 100 °C for 20 minutes $PC_{61}BM$ (Lumtec) (20 mg) and $PC_{61}BM:C_{60}$ (18 mg:2 mg) were separately prepared in 1 mL of 1,2-dichlorobenzene solvent and mixed on a magnetic stirrer for 12 hours without temperature application. The $PC_{61}BM$ and $PC_{61}BM:C_{60}$ solutions were then spin-coated onto the perovskite surface at 2000 rpm for 35 seconds. The BCP (Lumtec) solution (0.5 mg/mL in ethanol) was spin-coated on ETL at 4000 rpm for 45 seconds. Finally, a 110 nm-thick silver (Ag) top metal electrode was deposited using thermal evaporation method. Throughout the device fabrication process, all steps except for the top metal electrode deposition were carried out under ambient conditions with high humidity levels (40-60%).

PCEs and hysteresis factor (HF) of fabricated devices were calculated by using the following equations:

$$PCE(\%) = \left(\frac{P_{out}}{P_{in}}\right) x100 = \frac{Jsc\ xVoc\ xFF}{Pin} x100 \tag{1}$$

$$HF(\%) = \frac{|PCE_{Forward} - PCE_{Reverse}|}{PCE_{Forward}} x100 \tag{2}$$

3. Results

Fullerene and its derivatives are among the most often utilized ETLs for inverted-type (IT) PSCs. The effects of using of fullerene (C_{60}) in its derivative ($PC_{61}BM$) as ETLs for PSCs have been investigated on device performance. IT-PSCs were fabricated with the device configuration of ITO/PEDOT:PSS/$MAPbI_3$/$PC_{61}BM$ or $PC_{61}BM:C_{60}$/BCP/Ag. The fabricated device architecture and molecular structures of C_{60} and $PC_{61}BM$ were illustrated in figure 1.

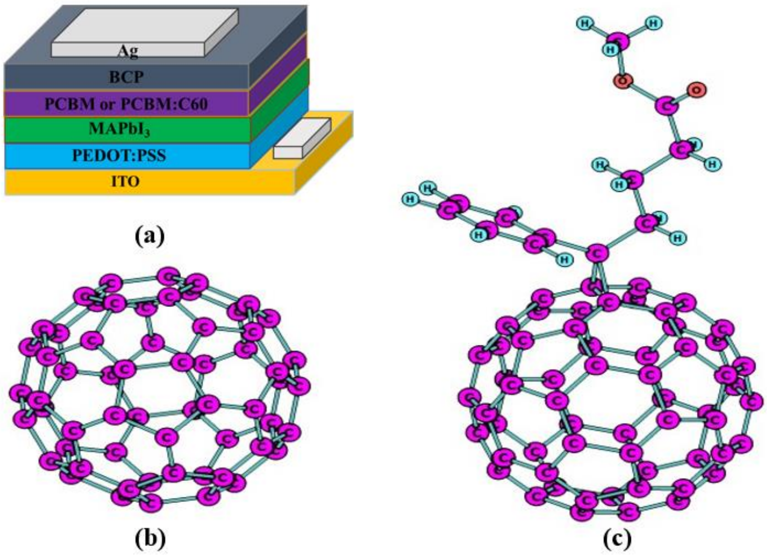

Figure 1. (a) Device structure of inverted-type PSC and molecular structures of (b) C_{60} and (c) $PC_{61}BM$

In order to determine the photovoltaic parameters of the fabricated IT-PSCs, current density-voltage (*J*-*V*) measurements were carried out. The photocurrent density-voltage (*J*-*V*) characteristics were measured under AM 1.5G irradiation at 100 mW/cm^2. Figure 2 displays *J*-*V* curves of control ($PC_{61}BM$ as ETL) and champion ($PC_{61}BM$:C_{60} as ETL) devices. In the absence of any small amounts of C_{60} additives, utilizing pristine $PC_{61}BM$ as the ETL (control device), the cell exhibited a short-circuit current density (J_{SC}) of 16.92 mA/cm^2, an open circuit voltage (V_{OC}) of 1015 mV and a fill factor (*FF*) of 67.2%. The photovoltaic parameters resulted in a power conversion efficiency (*PCE*) of 11.54% for the control device, with an average PCE of 10.37% across the fifteen fabricated devices. The addition of the C_{60} into $PC_{61}BM$ (champion device) boosted PCE to 13.40% with a J_{SC} of 18.36 mA/cm^2, a V_{OC} of 986 mV and a *FF* of 74.0% (average *PCE* of 12.91% for fifteen devices).

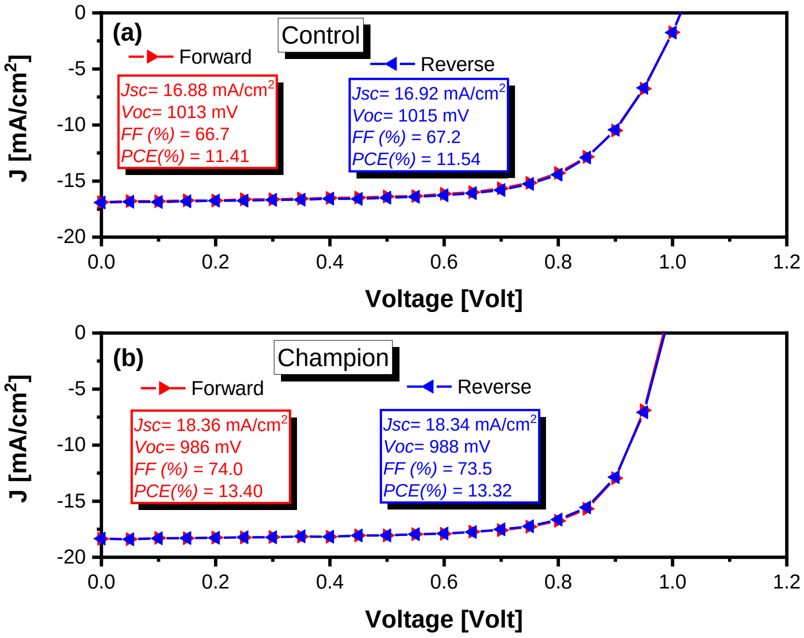

Figure 2. Current density (*J*) - Voltage (*V*) curves for (a) control and (b) champion devices

When the best efficiency values for the control and champion devices are compared, it is found that using C_{60} as the additive in ETL improves the *PCE* by approximately 16%. The primary factors contributing to this enhancement are clearly discernible in the form of increased J_{SC} and FF. It is evident that the addition of C_{60} into $PC_{61}BM$ has significantly boosted J_{SC}, increasing it from 16.92 mA/cm² (control) to 18.36 mA/cm² (champion), and FF has also improved from 67.2% to 74.0%. Another factor that affects the *PCEs* of PSCs is the current-voltage hysteresis. To comprehend the hysteresis effect of C_{60} as an additive in $PC_{61}BM$ on PSCs, both forward and reverse scans were carried out during *J-V* measurements. Photovoltaic parameters and *HF* values for control and modified devices are provided in Table 1. Table 1 reveals that the hysteresis factors for the control and champion devices were computed as 1.14% and 0.60%, respectively. It can be said that the negligible level of hysteresis factor obtained for the champion device might lead to improvements in the charge carrier extraction when C_{60} is added into $PC_{61}BM$. The average PCEs were determined based on a total of 30 distinct fabricated devices.

Table 1. Photovoltaic parameters of fabricated devices

ETL		J_{SC} (mA/cm^2)	V_{OC} (mV)	FF (%)	PCE (%)		HF(%)
					Best	Average	
$PC_{61}BM$ (Control)	Forward	16.88	1013	66.7	11.41	10.37	1.14
	Reverse	16.92	1015	67.2	11.54		
$PC_{61}BM:C_{60}$ (Champion)	Forward	18.36	986	74.0	13.40	12.91	0.60
	Reverse	18.34	988	73.5	13.32		

The surface morphology of the layers within PSCs has a substantial impact on their photovoltaic performance. Therefore, in order to gain a better understanding of the impact of C_{60} on the photovoltaic parameters, Scanning Electron Microscope (SEM) measurements were conducted. SEM images of $PC_{61}BM$ and $PC_{61}BM$: C_{60} layers on the perovskite were depicted in Figure 3.

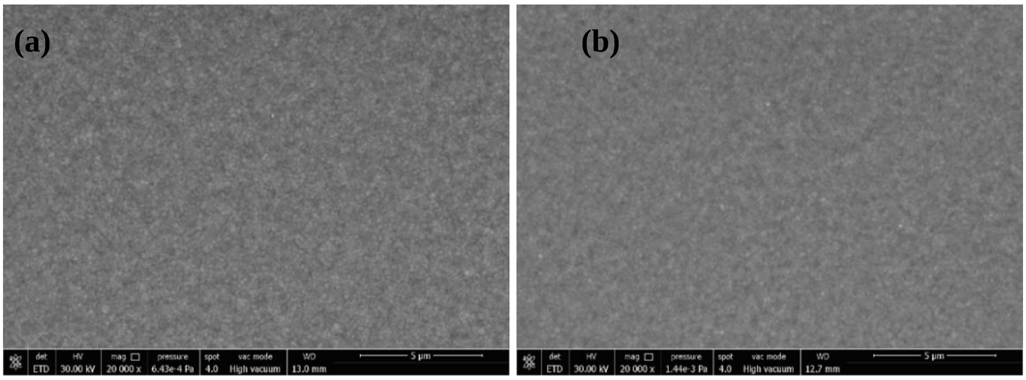

Figure 3. SEM images for (a) $PC_{61}BM$ and (b) $PC_{61}BM$: C_{60} layers on perovskite

It was realized that the ETLs deposited on perovskite appear to be quite uniform based on SEM measurements. There are almost no pinholes observed in films coated with both $PC_{61}BM$ and $PC_{61}BM:C_{60}$ on perovskite. To delve deeper into the effects of incorporating C_{60} into the ETL surface, atomic force microscopy (AFM) measurements were performed. In this way, it could be gained a more detailed understanding of the morphology of both the perovskite/$PC_{61}BM$ and the perovskite/$PC_{61}BM:C_{60}$ surfaces. 2D and 3D AFM images of $PC_{61}BM$ and $PC_{61}BM:C_{60}$ surfaces deposited on perovskite layers were illustrated in Figure 4. The Root mean square (RMS) roughness values for the interfaces of perovskite/$PC_{61}BM$, perovskite/$PC_{61}BM:C_{60}$ are 5.20 nm and 4.50 nm, respectively. It is evident that the $PC_{61}BM:C_{60}$ surface is smoother than the $PC_{61}BM$ surface from the AFM images. Thus, the incorporation of C_{60} into $PC_{61}BM$ enhanced the morphology of the ETL films, leading to smoother surfaces.

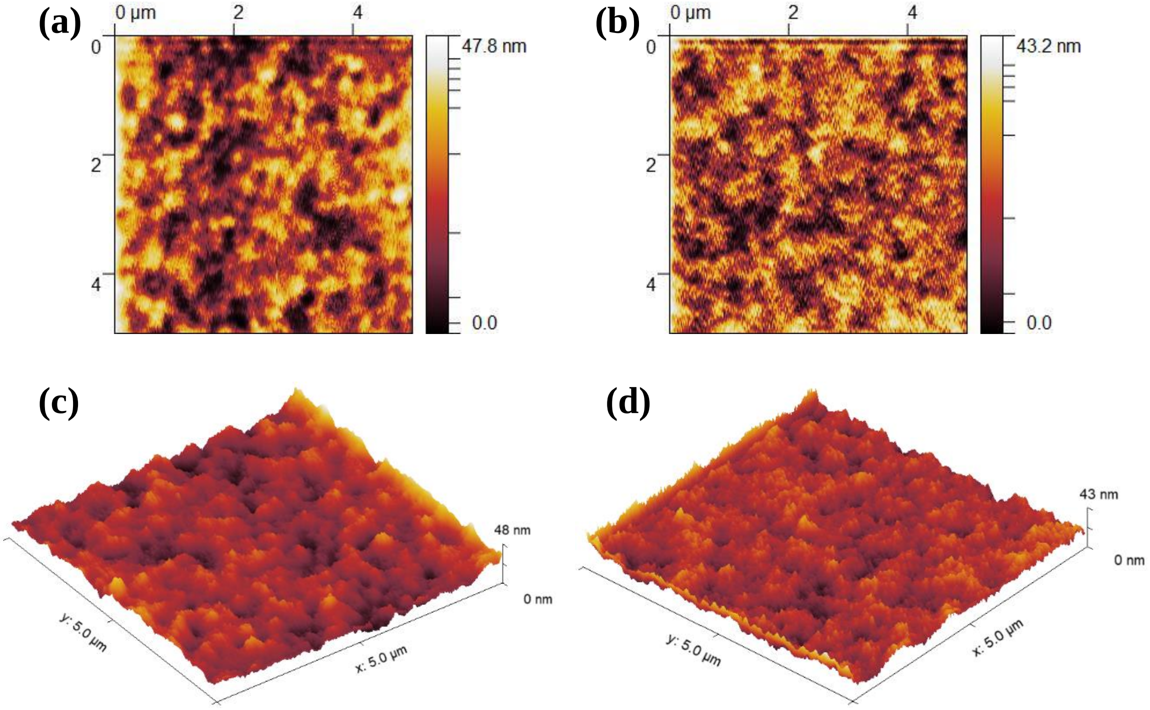

Figure 4. (a) 2D and (c) 3D AFM images of the $PC_{61}BM$ surface on perovskite, and (b) 2D and (d) 3D AFM images of the $PC_{61}BM:C_{60}$ surface on perovskite

The smoother coated of the ETL on perovskite can prevent direct contact between the perovskite and the metal layer applied on ETL. Consequently, this situation might allow for more efficient charge transport between the metal contact and the ETL, leading to reduced charge recombination [21]. It can be concluded that the photovoltaic results obtained for both control and champion devices clearly demonstrate the considerable influence of this enhancement at the perovskite/ETL interface. In this study, a total of 30 different devices were fabricated with 15 serving as controls ($PC_{61}BM$ used as ETL) and 15 incorporating C_{60}-doped ETLs, to investigate the impact of C_{60} on photovoltaic performance. The statistical distribution of photovoltaic parameters for the fabricated devices is illustrated in Figure 5.

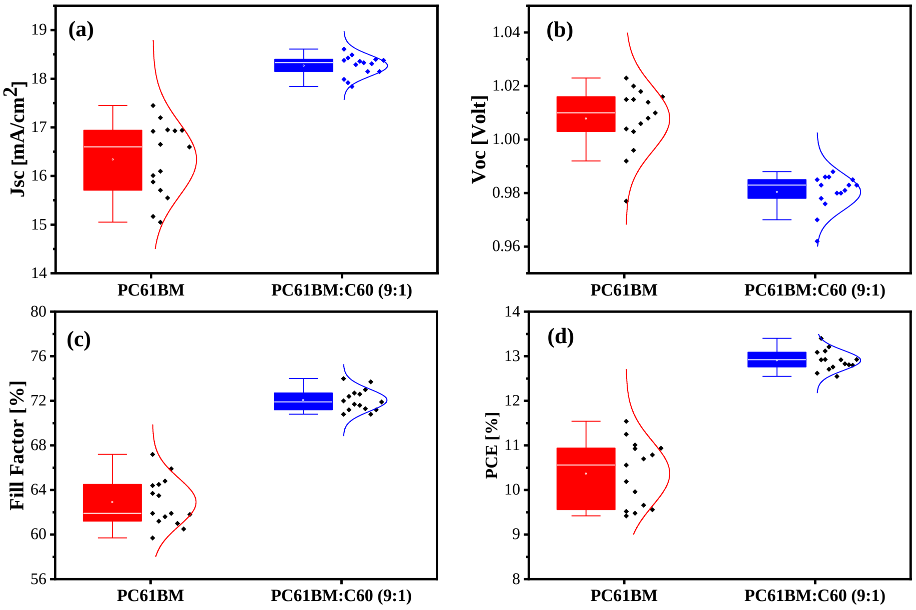

Figure 5. Statistic distribution of photovoltaic parameters for PSCs utilized $PC_{61}BM$ and $PC_{61}BM:C_{60}$ as ETLs: distribution of (a) J_{SC}, (b) V_{OC}, (c) FF and (d) PCE.

In devices where pristine $PC_{61}BM$ is used as the ETL, J_{SC} values are observed in the range of 15.05 to 17.45 mA/cm², while in devices where C_{60}-doped ETLs are employed, J_{SC} values have been observed in the range of 17.84 to 18.61 mA/cm². The minimum J_{SC} value (17.84) for C_{60}-doped devices surpasses the maximum J_{SC} value (17.45) for the reference device. V_{OC} values for devices with pristine ETLs range from 0.98 to 1.02 volt, whereas for doped ETLs, they range from 0.96 to 0.99 volt. There has been not a noticeable shift in V_{OC}. The *FF* values for control devices range from 59.7% to 67.2%, while for C_{60}-doped devices, they range from 70.8% to 74.0%. It is clear that there is a significant improvement in *FFs* as well. As a result, the enhancement of both J_{SC} and *FF* contributed to the increased *PCE* in devices incorporating C_{60} into the ETL.

4. Conclusion

In this study, IT-PSCs were fabricated using $MAPbI_3$ perovskite structure under high humidity (40-60%) and room temperature (~25 °C) and C_{60} was incorporated into $PC_{61}BM$ as the ETL to improve PCEs of PSCs. The photovoltaic results demonstrated that by incorporating C_{60} into the ETL, the *PCE* values for IT-PSCs were boosted from 11.54% to 13.40%. Additionally, it has been observed that the hysteresis factor decreased in devices with C_{60} doping. SEM and AFM measurements were conducted to assess the impact of C_{60} on the film morphology in PSCs. AFM images reveal that surface of C_{60}-doped ETL is smoother than the pristine ETL. The smoother surface of ETLs doped with C_{60} is thought to avoid direct interaction between the metal contact on the ETL and the perovskite structure. As a result, devices with doped ETLs show significant improvements in J_{SC} and *FF* parameters, attributed to enhanced charge transport and reduced charge recombination.

Authorship contribution statement

M. Kazici: Investigation, Conceptualization, Methodology, Formal Analysis, Original Draft Writing, Review and Editing

Declaration of competing interest

The author declare that he has no known competing financial interests or personal relationships that could have appeared to influence the work reported in this paper.

Acknowledgment

I would like to express my gratitude to Prof. Dr. Mahmut Kus from the Department of Chemical Engineering at Konya Technical University for his contributions in providing me with laboratory facilities.

Ethics Committee Approval and/or Informed Consent Information

As the author of this study, I declare that I do not have any ethics committee approval and/or informed consent statement.

References

[1] A. Kojima, K. Teshima, Y. Shirai and T. Miyasaka, “Organometal halide perovskites as visible-light sensitizers for photovoltaic cells”, *Journal of the American Chemical Society*, 131, 6050–6051, 2009.

[2] J. Jeong, M. Kim, J. Seo, H. Lu, P. Ahlawat, A. Mishra, Y. Yang, M. A. Hope, F. T. Eickemeyer, M. Kim, Y. J. Yoon, I. W. Choi, B. P. Darwich, S. J. Choi, Y. Jo, J. H. Lee, B. Walker, S. M. Zakeeruddin, L. Emsley, U. Rothlisberger, A. Hagfeldt, D. S. Kim, M. Grätzel and J. Y. Kim, “Pseudo-halide anion engineering for α-FAPbI3 perovskite solar cells”, *Nature*, 592, 381–385, 2021.

[3] A. K. Jena, A. Kulkarni and T. Miyasaka, “Halide perovskite photovoltaics: background, status, and future prospects”, *Chemical Reviews*, 119, 3036–3103, 2019.

[4] H. S. Kim, C. R. Lee, J. H. Im, K. B. Lee, T. Moehl, A. Marchioro, S. J. Moon, R. Humphry-Baker, J. H. Yum, J. E. Moser, M. Grätzel and N. G. Park, “Lead iodide perovskite sensitized all-solid-state submicron thin film mesoscopic solar cell with efficiency exceeding 9%”, *Scientific Reports*, 2, 591, 2012.

[5] M. M. Lee, J. Teuscher, T. Miyasaka, T. N. Murakami and H. J. Snaith, “Efficient hybrid solar cells based on meso-superstructured organometal halide perovskites”, *Science*, 338, 643–647, 2012.

[6] W. Hu, S. Yang and S. Yang, “Surface modification of TiO2 for perovskite solar cells”, *Trends in Chemistry*, 2, 148–162, 2020.

[7] W. Ke, G. Fang, Q. Liu, L. Xiong, P. Qin, H. Tao, J. Wang, H. Lei, B. Li, J. Wan, G. Yang and Y. Yan, “Lowerature solution-processed tin oxide as an alternative electron transporting layer for efficient perovskite solar cells”, *Journal of the American Chemical Society*, 137, 6730–6733, 2015.

[8] Q. Jiang, X. Zhang and J. You, “SnO2: a wonderful electron transport layer for perovskite solar cells”, *Small*, 14, 1–14, 2018.

[9] N. S. Sariciftci, L. Smilowitz, A. J. Heeger and F. Wudl, “Photoinduced electron transfer from a conducting polymer to buckminsterfullerene”, *Science*, 258, 1474–1476, 1992.

[10] R. Zahran and Z. Hawash, “Fullerene-based inverted perovskite solar cell: a key to achieve promising, stable, and efficient photovoltaics”, *Advanced Materials Interfaces*, 9, 1–18, 2022.

[11] X. Lin, D. Cui, X. Luo, C. Zhang, Q. Han, Y. Wang and L. Han, “Efficiency progress of inverted perovskite solar cells”, *Energy & Environmental Science*, 13, 3823–3847, 2020.

[12] M. A. Kumari, T. Swetha and S. P. Singh, “Fullerene derivatives: a review on perovskite solar cells”, *Materials Express*, 8, 389–406, 2018.

[13] D. Yang, X. Zhang, K. Wang, C. Wu, R. Yang, Y. Hou, Y. Jiang, S. Liu and S. Priya, “Stable efficiency exceeding 20.6% for inverted perovskite solar cells through polymer-optimized PCBM electron-transport layers”, *Nano Letters*, 19, 3313–3320, 2019.

[14] C. Kuang, G. Tang, T. Jiu, H. Yang, H. Liu, B. Li, W. Luo, X. Li, W. Zhang, F. Lu, J. Fang and Y. Li, “Highly efficient electron transport obtained by doping PCBM with graphdiyne in planar-heterojunction perovskite solar cells”, *Nano Letters*, 15, 2756–2762, 2015.

[15] J. H. Bae, Y. J. Noh, M. Kang, D. Y. Kim, H. B. Kim, S. H. Oh, J. M. Yun and S. I. Na, “Enhanced performance of perovskite solar cells with solution-processed n-doping of the PCBM interlayer”, *RSC Advances*, 6, 64962–64966, 2016.

[16] F. Xia, Q. Wu, P. Zhou, Y. Li, X. Chen, Q. Liu, J. Zhu, S. Dai, Y. Lu and S. Yang, “Efficiency enhancement of inverted structure perovskite solar cells via oleamide doping of PCBM electron transport layer”, *ACS Applied Materials & Interfaces*, 7, 13659–13665, 2015.

[17] J. S. Yeo, R. Kang, S. Lee, Y. J. Jeon, N. S. Myoung, C. L. Lee, D. Y. Kim, J. M. Yun, Y. H. Seo, S. S. Kim and S. I. Na, “Highly efficient and stable planar perovskite solar cells with reduced graphene oxide nanosheets as electrode interlayer”, *Nano Energy*, 12, 96–104, 2015.

[18] X. Zhu, J. Sun, S. Yuan, N. Li, Z. Qiu, J. Jia, Y. Liu, J. Dong, P. Lv and B. Cao, “Efficient and stable planar perovskite solar cells with carbon quantum dots-doped PCBM electron transport layer”, *New Journal of Chemistry*, 43, 7130–7135, 2019.

[19] Y. Wang, S. Dong, Y. Miao, D. Li, W. Qin, H. Cao, L. Yang, L. Li and S. Yin, “BCP as additive for solution-processed PCBM electron transport layer in efficient planar heterojunction perovskite solar cells”, *IEEE Journal of Photovoltaics*, 7, 550–557, 2017.

[20] Y. Bai, H. Yu, Z. Zhu, K. Jiang, T. Zhang, N. Zhao, S. Yang and H. Yan, “High performance inverted structure perovskite solar cells based on a PCBM:polystyrene blend electron transport layer”, *Journal of Materials Chemistry A*, 3, 9098–9102, 2015.

[21] E. M. Younes, A. Gurung, B. Bahrami, E.M. El-Maghraby and Q. Qiao, “Enhancing efficiency and stability of inverted structure perovskite solar cells with fullerene C60 doped PC61BM electron transport layer”, *Carbon*, 180, 226–236, 2021.